Ultrastable Atomic Force Microscopy for Biophysics

by

Allison B. Churnside

B.A., University of Colorado, 2002

M.S., University of Colorado, 2009

A thesis submitted to the

Faculty of the Graduate School of the

University of Colorado in partial fulfillment

of the requirements for the degree of

Doctor of Philosophy

Department of Physics

2013

This thesis entitled:
Ultrastable Atomic Force Microscopy for Biophysics
written by Allison B. Churnside
has been approved for the Department of Physics

Kyle McElroy

Thomas T. Perkins

Date

The final copy of this thesis has been examined by the signatories, and we find that both the content and the form meet acceptable presentation standards of scholarly work in the above mentioned discipline.

Churnside, Allison B. (Ph.D., Physics)

Ultrastable Atomic Force Microscopy for Biophysics

Thesis directed by Prof. Kyle McElroy

Atomic force microscopy (AFM) is a multifunctional workhorse of nanoscience and molecular biophysics, but instrumental drift remains a critical issue that limits the precision and duration of experiments. We have significantly reduced the two most important types of drift: in position and in force. The first, position drift, is defined as uncontrolled motion between the tip and the sample, which occurs in all three dimensions. By scattering a laser off the apex of a commercial AFM tip, we locally measured and thereby actively controlled its three-dimensional position above a sample surface to <0.4Å(Δf = 0.01–10 Hz) in air at room temperature. With this enhanced stability, we demonstrated atomic-scale ($\sim$1 Å) tip-sample stability and registration over tens of minutes with a series of AFM images. The second type of drift is force drift. We found that the primary source of force drift for a popular class of soft cantilevers is their gold coating, even though they are coated on both sides to minimize drift. When the gold coating was removed through a simple chemical etch, this drift in deflection was reduced by more than an order of magnitude over the first 2 hours after wetting the tip. Removing the gold also led to $\sim$10-fold reduction in reflected light, yet short-term (0.1–10 s) force precision improved. With both position and force drift greatly reduced, the utility of the AFM is enhanced. These improvements led to several new AFM abilities, including a five-fold increase in the image signal-to-noise ratio; tip-registered, label-free optical imaging; registered tip return to a particular point on the sample; and dual-detection force spectroscopy, which enables a new extension clamp mode. We have applied these abilities to folding of both membrane and soluble proteins. In principle, the techniques we describe can be fully incorporated into many types of scanning probe microscopy, making this work a general improvement to scanning probe techniques.

Dedication

To my husband, Brendan.

Acknowledgements

A large project such as this one is the result of efforts by many people.

First and foremost, I must thank my advisor, Tom Perkins, for overseeing this project and my PhD work. He has been a true mentor, teaching me not only laboratory skills, but also showing me how to navigate the many other aspects of research life. Tom's patient guidance, persistence, and understanding have been critical to my development as a scientist.

A number of Perkins group members have contributed to this project. Gavin King was one of the original creators of the Ultrastable AFM project, and its architect and champion. Working together with Gavin taught me innumerable laboratory tricks and techniques, and he has also been a mentor and advocate. Ashley Carter was another creator of the Ultrastable AFM, performing many of the early proof-of-principle experiments. Louisa Eberle was involved with the early stages of LabVIEW coding. Ruby Sullan contributed a tremendous amount of work to create robust protocols for attaching biomolecules to surfaces, and in the force drift project. Sara Case was a summer student who did the early work on the force drift project, convincing us that it was worth pursuing. Duc Nguyen has worked tirelessly to continue this project. Matt Bull has become an expert on the SEM and FIB, and is continuing to improve on the post fabrication protocols described here. George Emanuel contributed useful code for analysis of force curves. Matt Siewny will become the primary student on the Ultrastable AFM, and I am pleased to be able to leave it in his capable hands. I also wish to thank all of the Perkins lab members, past and present, who I did not work with directly. Their presence helped make the lab a pleasant and friendly place to be, and their scientific advice often helped me move forward: Amanda Carpenter, Wayne Halsey,

Martha Hosotani, Justin Kuczynski, Hern Paik, Rebecca Montange, Elisabeth Shanblatt, Violet Roskens, Rob Walder, and Peter Lawson.

It is well-known that JILA has an exceptional technical staff, and many of them have been involved with this project. Alan Patee did much of the original design of the AFM. Tracy Keep designed and fabricated many of the later parts, including the fluid cells and the stronger infrastructure described in Chapter 2. Hans Green helped develop the technique to add the windows to the fluid cells. Both Tracy and Hans helped trace and eliminate noise sources. David Alchenberger kept the cleanroom running and provided assistance on nanofabrication techniques. Carl Sauer built and helped improve and maintain the many custom electronics in the instrument. JR Raith, Jim McKown, and Mike Paige kept the computers running. Illustrators Greg Kubler and Brad Baxley are responsible for the artistic representations in the thesis. All of these people, plus Kim Hagen, Todd Asnicar, Kelsey Detra, Blaine Horner, Ariel Paul, Leslie Czaia, Terry Brown, James Fung-A-Fat, Paul Beckingham, and Alan Dunwell, provided technical assistance. In addition, everyone named here has brightened my days by sharing a geeky joke or encouraging word.

In addition, JILA has an exceptional administrative staff and supply office. Acknowledgements are due to Maryly Dole, Beth Kroger, Melanie McKinney, Dave Errickson, Brian Lynch, Jeff Sauter, Randall Holliness, and Jennifer Erickson for helping me at various times to keep the wheels turning smoothly.

The biophysics training grant program has been a major part of my graduate education, providing funding, helping me put my work in context, and introducing me to many fantastic biophysics colleagues. Many thanks are therefore due to Joe Falke for running this program, and to Lin Pharris.

A number of other professors at CU have provided valuable input to my PhD training. Dana Anderson supported the first year of my graduate work, and taught me a number of laboratory and project management skills in that time. Michael Stowell and Joe Falke met with me for training grant committee meetings, and provided feedback. My thesis committee— Ralph Jimenez, Kyle McElroy, Meredith Betterton, and Ivan Smalyukh— has also provided guidance and feedback,

especially during the final stages of the process.

Josh Shaevitz of Princeton provided software upon which my 3D calibration software is based.

Hongbin Li at the University of British Columbia spent several months of his sabbatical working with us on the NuG2 project, and is owed thanks for his contribution on that. In addition, working with such an expert on single-molecule force spectroscopy deepened my understanding of the technique immeasurably.

We use a number of commercial parts in our instrument, often at or beyond their intended limits, so the experts in these companies provide valuable assistance as well as engaging technical discussions. I would particularly like to thank Scott Jordan, Jaye Jillson, and David Steinberg at Physik Instrumente; Jason Cleveland, Deron Walters, Nick Geisse, Sophia Hohlbauch, and Mario Viani at Asylum Research; and Igor Alvarado and Patrick Webb at National Instruments.

I wish to acknowledge my family and friends. My husband, Brendan Billingsley, has organized many of the details of our home life so that I can focus on this work, and is a constant sounding board and source of support. My son, William, inspires me with his zest for life and learning. My dad, Jim Churnside, has shared the excitement of science with me as long as I can remember. My mom, Karen Churnside, and my mother-in-law, Elise Billingsley, have provided thousands of hours of child care. These and other family and friends, too numerous to name here, have provided much wisdom, encouragement, and support.

Finally, I would like to acknowledge the many funding sources that have contributed to the work described here. This work would not be possible without significant financial resources. They are: the Burroughs Wellcome Fund, a Beverly Sears Graduate Student Grant, the NIH Molecular Biophysics Training Program (T32GM-065103), the Butcher Fund, the National Science Foundation (Phy-0404286 and Phy-1551010), and NIST.

Contents

Chapter

Figures

Figure

Chapter 1

Introduction

Biophysics is a broad area of research that uses the tools and techniques of physics to understand the structure, dynamics, and energetics of biological systems. At all scales— molecules, cells, tissues, organisms, and environments— life can be considered as a set of complex systems. Application of physics to these systems includes the search for underlying mathematical principles, the reductionist approach, and development of novel instrumentation. First, physicists tend to understand the world quantitatively and look for underlying mathematical principles. This is often done by attempting to find the simplest models that explain the phenomena at hand. Second, physicists often take a reductionist approach to understanding a system, preferring to understand each part and then attempting to discern how the parts fit together into a whole. Single-molecule biophysics, the focus of much of this thesis, is one such reductionist strategy, and serves as a bridge between molecular physics and biophysics of larger systems. Single-molecule techniques, such as single-molecule fluorescence, optical trapping, and atomic force microscopy, are able to uncover heterogeneities that might be hidden by the use of a bulk method, often observing the energetics and dynamics of molecules in real time. Finally, physicists are well-suited to develop advanced instrumentation. Applying instrumentation principles to biology has a long history dating back to the invention of the microscope itself, and including now-well-established techniques such as NMR, electron microscopy, x-ray scattering, and laser spectroscopy.

Atomic force microscopy (AFM) is an extremely valuable tool in single-molecule biophysics and nanotechnology as a whole. It can produce detailed images of a wide variety of systems—

from the chemical bonds in a single small organic molecule [1, 2] to the architecture of membranes from eye lens cells [3, 4]. It was critical in determining the arrangement of the photosynthetic apparatus in its native membrane under varying light conditions [5], and mapping the surface properties of pathogens [6]. Biological AFM excels at the problem of understanding how smaller protein units are arranged to form larger assemblies. Unlike many characterization methods, AFM is a dynamic technique, able to capture events such as conformation changes in a photosynthetic protein [7] in real time. AFM is also an uncommonly direct method for manipulating matter at the nanoscale, with the ability to act as a nanoscale pen [8] and assemble individual DNA molecules [9]. Unlike many other biophysical characterization techniques, AFM can operate over a wide variety of conditions and with a wide variety of samples, including biologically relevant aqueous conditions.

At its core, an AFM consists of an atomically sharp tip interacting with a sample, producing a force. A wide range of AFM tips are commercially available. The only further requirements are a way to measure the force, and a way to move the tip and/or sample with the required resolution (Figure 1.1). To measure the force, the tip is situated on a cantilever, so that a force on the tip corresponds to bending of the cantilever. Originally AFM was conceived as a generalization of scanning tunneling microscopy, and the bending was measured by electron tunneling [10], a very sensitive but difficult configuration. While a number of deflection sensing techniques have emerged through the years, a relatively simple technique known as an "optical lever arm" [11] is by far the most popular. Optical lever arm sensing involves reflecting a focused laser beam off the backside (i.e., opposite the tip) of the cantilever and observing the distribution of optical power at a detector (usually a quadrant photodiode). It derives its name from the fact that small deflections of the tip yield relatively large translations of the beam on the detector. The technique is straightforward to implement and precise, yielding <5 pm detection sensitivity across a broad bandwidth (0.1 -1000 Hz), (Asylum Cypher Spec Sheet). Furthermore, optical lever arm sensing is relatively inexpensive and can be applied in fluid environments— a must for biological applications. For these reasons it is frequently implemented on commercial and custom AFM instruments. To move the tip and the sample at the nanoscale, AFM relies on piezoelectric technology. Although the current generation

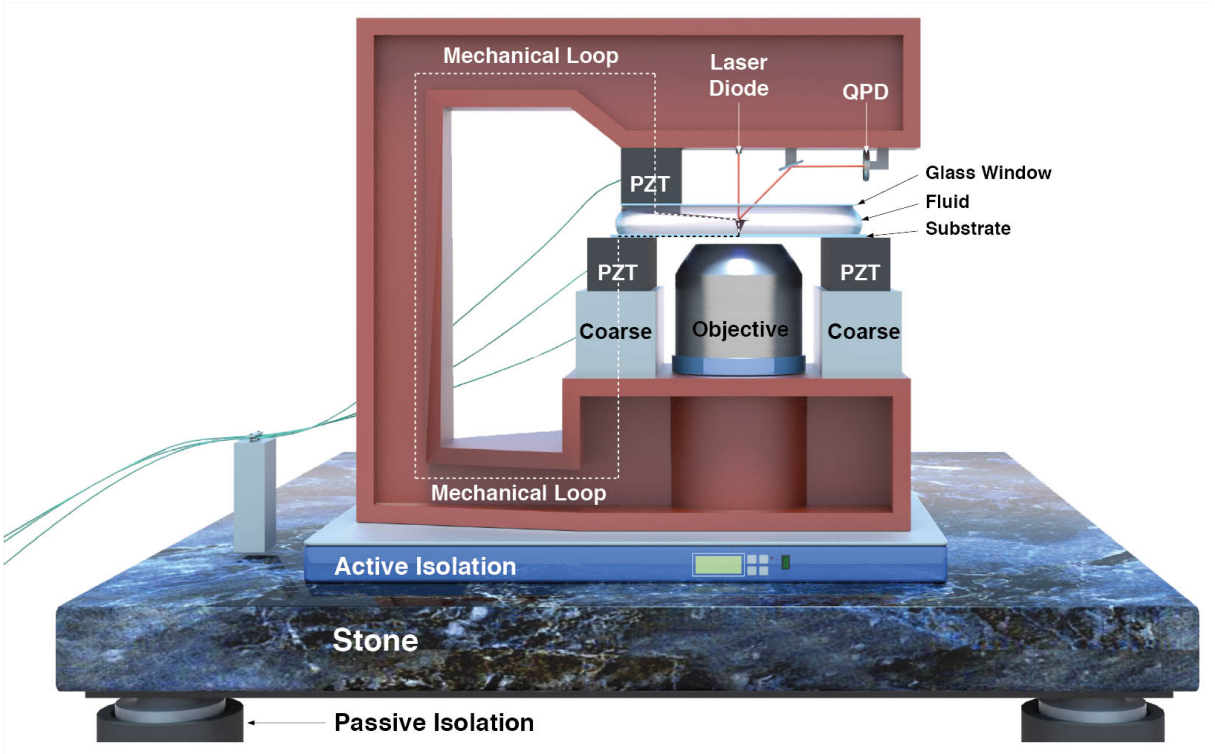

Figure 1.1: Artist's illustration of a biological AFM highlighting key components and considerations for passive stability. The optical lever arm system formed by the laser diode and the quadrant photodetector (QPD) measures the force by measuring the deflection of the cantilever. Piezoelectric stages (PZT) produce small (10 pm-10 μm) movements of the tip and the sample (Substrate), while a coarse stage (Coarse) provides the ability to align the tip to an interesting feature. For biologically-relevant applications, the experiment must be enclosed in fluid, with a glass window stabilizing the fluid-air interface. Often an objective is added to provide optical microscopy data. The mechanical loop is the path traced from the tip, through the microscope, back around to the sample. Any motion in this loop will present itself as noise or drift in the system. To reduce noise from the floor, an AFM is often mounted on top of an active isolation platform, and passive isolation techniques such as a heavy table (stone) and pneumatic table legs are employed. (Figure credit: Brad Baxley)

of these stages use sensors along with feedback loops to stabilize the position and compensate for PZT creep and hysteresis, as we will see in subsequent sections, drift remains a problem.

For biological applications, two primary modes of operation are most common: imaging (Figure 1.2, a) and single-molecule force spectroscopy (SMFS) (Figure 1.2, b). In imaging modes of operation, a molecule is adhered to the surface and the tip is raster scanned over it while force is measured by the optical lever arm laser. In the simplest "contact mode" imaging, the tip height is adjusted during this process to keep the tip deflection (proportional to force) constant. This type of imaging is favored by researchers who achieve high-resolution images of membrane proteins [4], where the changes in topography are small (Ångstroms). More complicated AC modes of imaging are more typical, where the tip is oscillated near its resonant frequency, and the amplitude, phase, or frequency of the oscillations are used to measure the interactions with the surface. This is then used in the feedback loop to keep the interaction constant. Operating in an AC mode generally allows smaller forces to be used, and reduces the lateral friction, and thus more gentle imaging can be performed. SMFS measurements consist of a molecule being held between the tip and the surface. Since this type of measurement is the one I primarily used in this thesis, it is discussed in detail in the next section.

1.1 Protein folding with single-molecule force measurements

It is still not fully understood how a protein folds. The protein folding problem is most often visualized as a rugged, funnel-shaped energy landscape of peaks and valleys. The native structure is the lowest energy state, the outer high-energy rim represents the numerous unfolded states, and troughs represent stable folding intermediates. A full description of the folding pathways describes the path that the protein traverses through this landscape, and the probabilities to go in any given direction. In general, it is understood that local and secondary structures fold first, then more global structures assemble from these parts. However, an overall mechanism for protein folding is still lacking [12]. As a consequence, the prediction of protein structure from sequence is still very difficult. Since about 1000x more sequences are known than structures [12], unlocking this

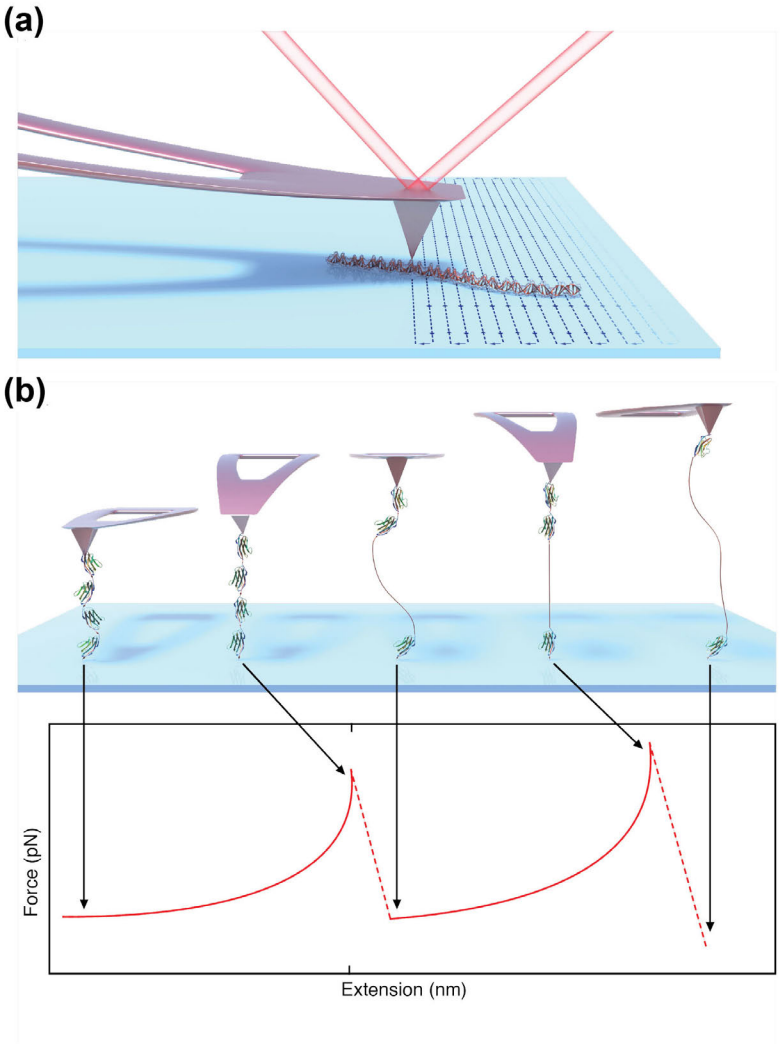

Figure 1.2: A cartoon illustrating the two most common types of AFM studies on biological molecules. (a) In imaging modes, the tip is typically raster-scanned across the surface while the force is monitored by the optical lever arm laser (*red*). There are many types of AFM imaging; the simplest involves moving the cantilever up and down so that the force remains constant. (b) In single-molecule force spectroscopy, a molecule is attached with one end on the surface and the other on the AFM tip. The tip is then retracted, which results in an increasing force on the cantilever, then a sudden drop when part of the molecule unfolds. (Figure credit: Brad Baxley)

predictive ability would result in great payoffs. We would also reap great benefits from the ability to solve the reverse problem: determining a protein sequence that would fold into a desired structure [13].

By pulling a biological macromolecule by its ends, an AFM can be used to study the energetics and dynamics of folding and assembly. This is known as single-molecule force spectroscopy (SMFS), although no optical spectrum is involved. The simplest form of SMFS is to attach the molecule to the AFM tip and move the piezoelectric translation stage at a constant rate away from the surface. Simply stretching a disordered polymer chain will result in an entropic stretching curve, following the wormlike chain (WLC) model. If there is an ordered region (*e.g.* a protein) in the chain, unfolding events cause sudden drops in the force, as the new segment is introduced into the stretched unfolded polymer. For tandem repeats of identical proteins, this results in a characteristic, evenly-spaced "sawtooth" unfolding pattern, with each curve in the sawtooth fitting to a WLC of the appropriate length [14]. This makes the resulting trace easier to identify and interpret, which is the reason that researchers often use identical repeats in constructs for force studies. For a more complicated protein, such as the seven-helix membrane protein bacteriorhodopsin (BR) discussed extensively later, the unfolding pattern has unevenly-spaced peaks, and may not be the same each time [15], evidence that the protein may follow one of a number of unfolding pathways. Analysis of these unfolding patterns can provide information about unfolding units, and, in the case of membrane proteins, topology and anchor points of the protein in the membrane. However, more information can be obtained by using more complex pulling protocols.

Several unfolding protocols have been used to measure biomolecular folding and unfolding. A double-pulse protocol can measure folding kinetics at the single-molecule level [16]. This experiment is performed on a polyprotein of identical repeats. The molecule is unfolded, then the tip is held near the surface for some amount of time, and then the molecule is unfolded again. By counting the number of protein units that folded for a given wait time, the kinetics of folding can be measured. Using a technique called Dynamic Force Spectroscopy [17], the unfolding barriers for a molecule can be located. In this technique, the peak unfolding force of a protein, or unbinding of an adhesion

bond, is determined as a function of pulling rate. The force clamp technique is a valuable way to study folding [18, 19]. The protein is held at a high force, and the unfolding is observed as a series of steps. Then the protein is relaxed back to a low force, and its folding trajectory is monitored. An extension clamp is the logical complement to a force clamp, but is hampered by the presence of drift, as will be seen in the example below. The work described in this thesis enables an extension clamp by introducing a new, direct measurement of extension.

1.2 Drift and stability in AFM

Several types of instrumental drift present significant problems for biological applications of AFM. Lateral position drift adversely affects the ability to keep an object in the field of view, or to return to the same feature after, for instance, an extended incubation period. It also limits the user's ability to take a slow image, which might be desirable in order to decrease noise by averaging down the Brownian motion of the tip. Vertical position drift limits the precision and duration of force spectroscopy experiments. Force drift, a related but distinct issue, has the same effect on force spectroscopy, and also on imaging. Molecules can change conformation depending on the force [20], and the imaging conditions can be degraded if the force drifts outside of an acceptable range. Although software-based techniques have been implemented [21], an AFM operator typically adjusts the force set point manually during imaging. Force drift is a more significant concern for contact mode imaging; AC modes of imaging are less susceptible to force drift. Drift in AFM can be minimized by operating in more isolated environments (Figure 1.3). The most stable AFMs operate in vacuum at cryogenic temperatures. However, this set of conditions forfeits biological relevance.

As an illustration of how the problem of drift affects measurements, consider two recent papers on the folding and unfolding landscapes of the protein calmodulin. In the first, the Rief group used an AFM to investigate the conformational fluctuations of this calcium-sensing protein at the single-molecule level [22] with high-precision ($\sim$2 pN) AFM. They were able to achieve this level of precision because they built a custom, low-drift AFM and were therefore able to pull

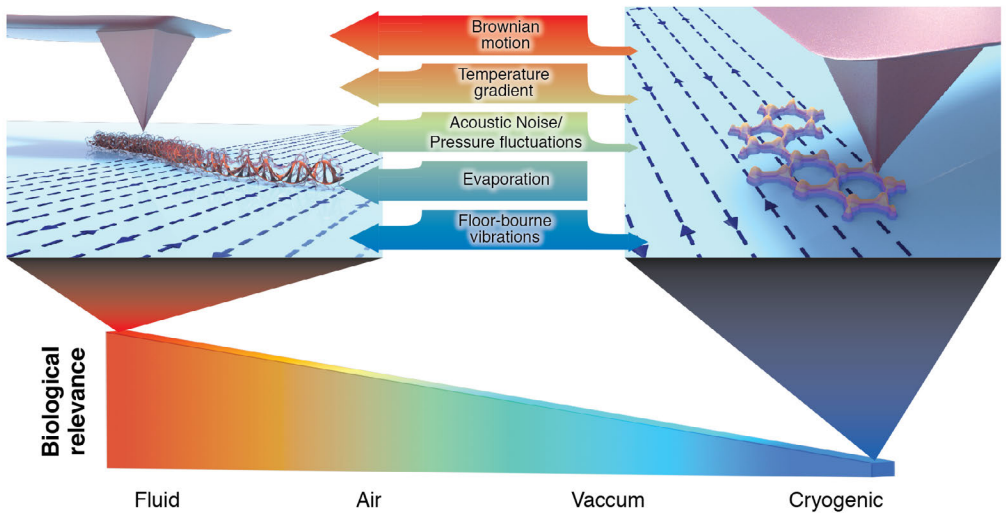

Figure 1.3: Illustration showing the trade-offs between biological relevance and isolation from noise sources. The most biologically relevant conditions— in fluid at room temperature— also make the instrument more susceptible to the many sources of noise listed. Although each noise source can be attenuated somewhat, the quietest conditions for AFM are ultimately achieved by moving away from biological relevance, toward a cryogenic system. Our goal is to bring cryogenic levels of stability to biologically relevant conditions. (Figure credit: Brad Baxley)

at an extraordinarily slow velocity (1 nm/s). At this stretching rate, they observed equilibrium hopping between two folding sub-states over 1-2 s. They went on to show how the kinetics of this hopping depended on the Ca^{2+} concentration. Two years later, the same group elucidated the full kinetic pathway for calmodulin folding and unfolding using an ultrastable dual-beam optical trap [23]. The motivation for changing measurement platform was better stability and precision. The researchers were now able to achieve 300-s long records of folding and unfolding at a fixed extension ($v = 0$). These records revealed a complex folding pathway containing six states, including transiently populated folding intermediates. More generally, this paper highlights the ability of optical traps to reveal and quantitatively measure the full energy landscape of a single protein.

Given the success of optical trapping in this experiment, it is reasonable to question whether AFM should continue to be a popular tool for SMFS. One critical advantage of AFM is that highly stable instruments are commercially available, broadening the range of users. Moreover, AFM is inherently a surface-based technique, allowing for a broader range of systems to be studied than in a dual-beam optical-trap assay. For example, the small surface area of an AFM tip facilitates extracting an individual membrane protein from a lipid bilayer for folding and unfolding studies [15]. Furthermore, AFMs combine force spectroscopy with sub-nanometer resolution imaging [15]. On a more technical level, dual-beam traps require relatively long handles (∼300-600 nm), while AFMs can use much shorter constructs (20-40 nm), dramatically decreasing compliance issues. A final advantage is AFM's ability to access higher forces without significant radiation damage. Hence, there is a bright future for AFM-based force spectroscopy if its strengths can be combined with the force precision and stability of state-of-the-art optical traps.

There exist a handful of drift-compensation methods that exhibit varying degrees of success and usability. Tracking techniques [24, 25, 26] can yield atomic precision in ultra-high vacuum, but they forfeit scanning or assume unvarying drift rates. Software-based techniques can reduce drift rates to ∼500 pm/min in ambient conditions [27], but require predictions of future drift or compensate for drift only once per image. The advent of high-speed AFM [28, 29] increases the viability of these image-based techniques for controlling drift in the lateral dimensions, since the

correction rate is higher, but the problem of vertical drift remains. External optical techniques, applied in one [30, 31] or more dimensions [32, 33], have not achieved atomic-scale tip-sample stability or image registration (<10-nm overlay precision [33]).

Sub-pN force precision in a limited bandwidth has been observed during AFM-based SMFS experiments using lock-in amplification [34]. In this study, a 5-nm oscillation was applied to the tip at 20 Hz. These improvements allowed the folding pathway on immunoglobulin to be more carefully examined. Overall, lock-in detection improves force precision in a specified bandwidth but can complicate interpretation. (This paragraph was adapted from References [35] and [36].)

The work described in this thesis was motivated by the need in the field for general techniques to reduce all types of drift. We addressed lateral and vertical position drift by using a new optical measurement, along the way discovering a useful tip-registered optical imaging technique. With this lowered position drift, the problem of force drift came to the forefront, and we found that it could be significantly reduced by simply removing the gold from AFM cantilevers. Finally, by applying this unique combination of ultrastable AFM and stable cantilevers, we observed equilibrium fluctuations of a membrane protein, which were previously inaccessible to AFM. We have also studied equilibrium fluctuations of a soluble protein and have begun to characterize its folding.

1.3 Thesis outline

To solve the problems associated with drift in AFM, we introduced an optically based frame of reference for the measurement. We directly measure the positions of the AFM tip and the sample substrate with backscattered light from two laser foci. These measurements are then used in feedback loops to PZT stages in order to keep the tip stable with respect to the sample. In Chapter 2, I first discuss the instrument hardware (2.1), with particular emphasis on the many new developments since the thesis of Ashley Carter [37]. I then detail the LabVIEW software that runs the instrument (2.2). Sections of that discussion are adapted from Reference [38].

Once the stability of the instrument was demonstrated, we were able to confirm the stability through the most relevant test, imaging. We showed that the images of a 5-nm gold bead stuck to a

surface were very stable over 80 minutes of imaging. We also showed that we could improve image quality by acquiring images more slowly and averaging away noise. Thus the work in Chapter 3, which is adapted from Reference [35], showed that we had achieved a functional ultrastable AFM.

Our ultrastable instrument was also uniquely suited to solving the "needle in the haystack" problem common in AFM. Since molecules are often sparsely adsorbed over a surface, finding a region of interest can be time-consuming. It can take hours to find a suitable region for study. In this time, repeated scanning to locate molecules can damage both the tip and the sample. Inspired by [39] and [40], we realized that our instrument was well-suited for label-free optical imaging. The optical image is acquired by scanning the beam across the surface and collecting the backscattered light. Furthermore, since the AFM tip position is registered to the laser focus, the optical and AFM images are also registered. This ability allowed us to quickly locate 5-nm-thick membrane patches on the surface, and also paved the way for registered tip exchange and return, where a worn tip can be exchanged with a fresh one, or one with different properties, returning to the same region of the sample. This work is discussed in Chapter 4, and much of it was adapted from [41].

Currently, force spectroscopy experiments must be completed quickly to outpace the effects of drift. Typically, the force is measured with the optical lever arm system, while the extension is inferred by the position of the translation stage. However, with the ultrastable AFM, we now have direct measurements of both conjugate variables: force and position. This dual measurement allows new types of experiments that include slow pulling, which allows the user to average Brownian motion and to observe events that would otherwise be missed; and extension clamping, which allows the user to isolate events to study for long durations in equilibrium conditions. Chapter 5 details the technical improvements enabling this position detection far from the surface, as well as results showing determination of the sample zero point and the advantage of slow pulling with dual detection. Much of the discussion in this chapter is adapted from [42].

Once we attempted to use dual-detection single-molecule force spectroscopy in protein folding experiments, we quickly found that position stability is only part of the problem: force drift also occurs. We traced the source of this force drift to the gold coating on the cantilevers. Gold is added

to AFM cantilevers to increase their reflectivity, and thus the sensitivity of the optical lever arm measurement. By removing the gold coating from AFM cantilevers, we reduced the drift at low frequency by a factor of 10. Our critical result was that, although the reflectivity and sensitivity were indeed decreased, the signal-to-noise ratio actually increased, resulting in sub-pN force sensitivity. This level of sensitivity is typically thought to be outside the capability of AFM [43]. In the course of this research, we also characterized noise for several types of cantilever, showing that smaller is not always better for force precision at low frequency. Chapter 6 is primarily adapted from our paper on this topic, Reference [36].

Using these new techniques, we studied the unfolding and refolding of the model membrane protein bacteriorhodopsin (BR). Membrane proteins represent an important frontier in biophysical research, as their characterization has lagged behind that of soluble proteins. In these experiments, a patch of membrane containing a 2D crystal of BR was adsorbed onto the surface, and one end of the protein was attached to the tip during various pulling protocols. We were able to observe hopping back and forth over a folding barrier using slow, dual-detection single-molecule force spectroscopy. This slow pulling was made possible by the extreme precision of the instrument. By then using a novel "extension-clamp" mode enabled by the ultrastable AFM near one of these transitions, we observed several events, and an occupancy distribution that was sensitive to the extension. However, the force drift discussed in Chapter 6 and other issues hindered a quantitative interpretation of the results. The status of this unpublished project is described in Chapter 7.

We also explored the folding and unfolding of a much simpler system, the small folding unit NuG2. This protein was computationally designed by the David Baker group to test understanding of protein folding pathways. Although the system is much simpler, we found that the folding and unfolding kinetics were also much slower than with BR. Even with reduced drift, extension clamping did not yield a sufficient number of events quickly enough to make quantitative statements about the kinetics. We therefore developed a technique where the extension is alternated back and forth between a point where folding is favored and one where unfolding is favored, expanding again on the novel extension clamp. Using this protocol, enough data could be collected to measure kinetics,

but a full description of the folding and unfolding pathways remains elusive. The work with NuG2 is detailed in Chapter 8.

In summary, by introducing two extra focused laser beams into the interaction region of an AFM, we were able to reap a number of benefits. In principle, this is a very general technique that can be applied across the field of scanning probe techniques, and combined with many other recent advancements to them. In the final chapter (9), I discuss future directions in our research into AFM and also review ways in which other researchers are making use of our technology.

Chapter 2

Optically stabilized AFM

This chapter describes the stabilized AFM instrument. In Section 2.1, I describe the instrument hardware and physical components. In Section 2.2, I describe the software, including FPGA control.

2.1 Hardware

In this section, I describe the ultrastable AFM. The stabilization system (Section 2.1.1) consists of two stabilized laser beams focused through an objective into the region near where the tip and sample interact. One laser beam is focused onto the tip itself, and one onto a silicon fiducial mark fabricated onto the sample substrate (Section 2.1.2). The backscattered light from these laser beams is first separated from the forward going light, then separated by color, and finally imaged onto two quadrant photodetectors. This assembly is built on a highly modified optical microscope mounted on an optical table, with many considerations for passive vibration control, as described in Section 2.1.3. In order to perform biological experiments, we required a fluid chamber, which is described in Section 2.1.4.

2.1.1 Optical detection

The stabilization system has been described previously in References [45, 44, 35] and [37]. In order to achieve a high degree of stability, the laser beams must have low pointing, mode, polarization, and intensity noise (unlike many applications, spectral stability is not particularly

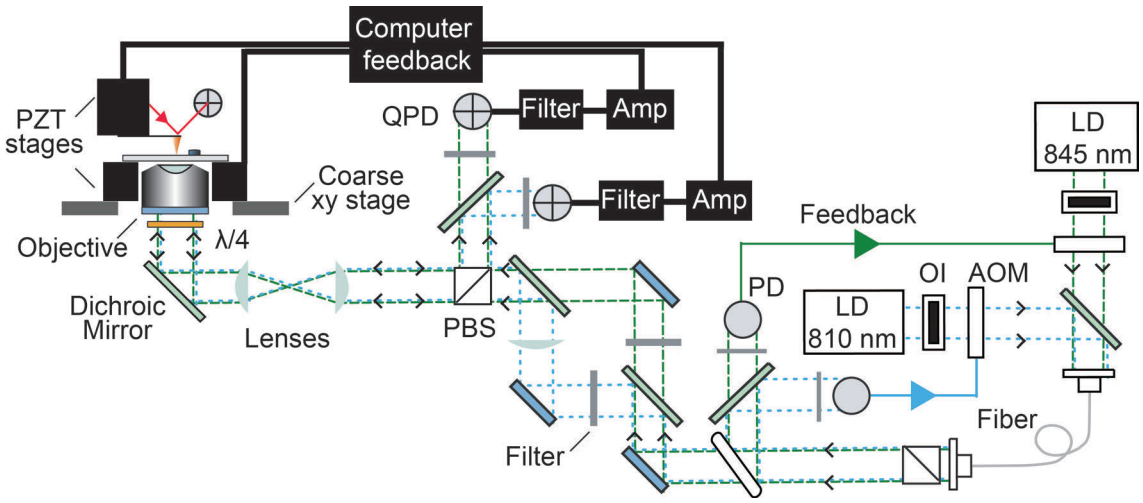

Figure 2.1: Schematic of instrument. Beams from two laser diodes (LD, λ = 810, 845 nm) were actively stabilized to minimize noise using feedback to acousto-optic modulators (AOM) [44]. These stabilized beams were launched from a common polarization-maintaining fiber to minimize differential pointing noise. They were then separated by wavelength for independent steering. A lens in one beam path vertically shifted one of the foci in the imaging plane so as to simultaneously maximize the scattering signal from the tip and the fiducial mark on the surface. The beams were recombined, and a high numerical aperture objective focused them near the sample surface, where they scattered off of the tip or features on the substrate. Backscattered light was efficiently separated using an optical isolator, formed by a quarter-wave plate ($\lambda/4$) and a polarizing beam splitter (PBS), and then collected onto quadrant photodiodes (QPD). The resulting signals were filtered with a cutoff frequency of 2.4 kHz (Filter), the sum signal was offset amplified (Amp), and computer feedback was used to control the PZT stages. PD and OI denote photodiodes and optical isolators, respectively. Figure adapted from Reference [41].

important here). To achieve this, the two low-power laser beams (λ = 810 nm and λ = 850 nm) lasers used for stabilization were simultaneously launched from a single optical fiber and sent through a polarizing beam splitter cube, which has the effect of collapsing pointing, mode, and polarization noise onto intensity noise. Coupling two lasers to a single fiber can be a daunting task. It is important to make sure that the two beams have the same diameter, so that they will both be properly focused onto the end of the fiber with the same lens. One coupling mirror for one beam (in our case, the 810 nm laser) will be a dichroic mirror, which allows the other wavelength (845 nm) to pass. In this situation, the 810 nm laser must be coupled into the fiber first, then the 845 nm laser. Otherwise, moving the dichroic mirror to couple the 810 nm laser will disrupt the coupling of the 845 nm laser.

The intensity at this point was held constant by a feedback loop to an acousto-optic modulator (AOM). We use a slightly less rigorous version of the Ziegler-Nichols method to tune these feedback loops. First, all gains (coarse proportional, fine proportional, and the PI corner) are turned all the way to zero (left). The in-loop photodiode signal is monitored by oscilloscope as each is adjusted. The coarse gain is turned up until oscillation begins, then turned back down one click. The fine gain is then turned up until oscillation begins, and turned back down two full turns. Finally, the PI corner is turned up until oscillation begins, and turned back down two turns. The feedback loops seem to perform best when the manual power is near the feedback setpoint. Typical values are 8V for the 845 nm laser, and 0.8 V for the 810 laser. If the feedback loops are unable to achieve these values at typical laser currents of 200 mA, there is likely a problem with either the fiber coupling, the AOMs, or the lasers themselves. As a final note, the position sensing QPDs can act as useful out-of-loop sensors for diagnosing problems with the intensity feedback loops. To do this, mount a featureless, reflecting sample (*e.g.* a gold-coated coverslip) and collect the backscattered light onto the QPDs.

Each laser was independently translated in the imaging plane by mirrors conjugate to the back aperture of the objective lens (PlanAPO-100X-IR, NA=1.4; Nikon) and vertically adjusted with a long focal length lens. The foci were laterally offset $y_{lasers} \approx 10\mu$m (Fig. 1a). The backscattered

signals are most symmetric, and therefore easiest to calibrate with, when the lasers are near the center of the objective, which corresponds to the center of the camera screen. A 2–5 m lens placed after the 845-nm beam-steering mirror imparted a slight vertical shift (∼500 nm) between the laser foci. This shift led to more effective scattering off of the tip, which is vanishingly small at the sample plane. Different types of tip could work best with different focal lengths for this lens, though the 5-m focal length lens seems to work well with the types of tip we use the most (Olympus Biolever and TR-400). If it is very difficult to find an operating z plane where the tip and sample are both well-calibrated, a different lens can sometimes help. The beams were focused through a high numerical aperture (PlanAPO-100X-IR, NA=1.4; Nikon) objective onto the surface, where the laser power on each was <1 mW. To reduce air currents, optics external to the microscope were enclosed in a box and beams were enclosed within 2.5-cm tubes wherever possible.

After the lasers scattered off of the tip and fiducial mark, the back-scattered light from each was efficiently separated from the incoming light using an optical isolator formed by a polarizing beam splitter (PBS) and a quarter waveplate ($\lambda/4$), which was mounted at an angle to reduce unwanted back reflections, and detected using a quadrant photodiode (QPD). To achieve the best signals, it is important to adjust the position of the QPDs so that the x and y signals are zero when the tip is near the surface, but the laser is not scattering off the tip or the fiducial mark. The laser power distribution on the QPD depends on the position of the scattering object in the laser focus. Ideally, the difference between left and right halves would be a function of the position in x, the difference between top and bottom halves a function of the position in y, and the total light falling on the detector a function of the vertical z position. By rotating the QPD while moving in one direction and observing the resultant signals, the crosstalk can be minimized, but not completely eliminated. The real geometry of the fiducial marks, and especially of the tips, is far from ideal, causing significant crosstalk between axes. The solution to this problem, a fully crosstalk-compensated calibration routine, is described in Section 2.2.

Cantilever-deflection sensing, based on an optical lever arm (Fig. 1b, *red*), was achieved with a 785-nm fiber-launched diode laser sensed by a third QPD. Unlike typical AFM, we intensity

stabilized this laser as well, although we have been unable to detect an improvement in AFM performance due to this stabilization. A lens on a translation stage moves the position of the beam, though in practice coarsely aligning the laser to the cantilever can be challenging. There are two protocols we have found to be useful in this process. In the first, a piece of paper is stuck over the end of the QPD tube (taking care not to touch the optical filter with either fingers or tape) so that the scattered optical lever beam can be observed with the IR viewer. Typically several beams can be observed here; the user should focus on the patterns that move when the lens is moved, and ignore all others. The user moves the beam in the y direction to find the edge of the cantilever chip, which is marked by a sharp transition from a "speckle" scatter pattern to no reflected beam. With the beam just off the chip, the user then moves the beam near the edge of the chip in x to find the cantilevers, which are typically spots that quickly appear and disappear. The second coarse alignment protocol is only recommended if the user is mounting a tip of the same type as the previously used one, so that the position of the tip is likely to be very similar. In this protocol, the user moves the tip mount a significant distance (1/2 coarse turn) in the $+y$ direction, then lowers the tip toward the surface until the chip, then the cantilever, can be seen by the camera. The user can then find the beam spot on the camera, and align them visually. Once the coarse alignment is complete, the QPD sum signal can be monitored to align the beam more carefully. In order to do this, both the x and y QPD signals must be on scale, and preferably near zero, which is achieved by moving the QPD itself. Section 2.1.4 contains more discussion of what to do when this is not possible. Then, the QPD sum signal should be approximately 2V for gold-coated cantilevers and 0.2V for uncoated cantilevers. If the beam is on the cantilever, the QPD sum signal should drop off quickly (within 1/2 fine turn on the lens translation stage) when the beam is moved in x. When the tip is touched to the surface, the deflection (y) QPD signal should decrease; if it increases, the beam is likely reflecting within the lens tube, causing an inversion.

The optical lever arm geometry is prone to artifactual position-based voltage change when the tip is moved vertically relative to the surface. These artifacts are commonly understood by the AFM community to be due to a combination of unwanted back-reflective feedback into the diode

laser and unintentional interference cavities. For instance, the light reflecting from the cantilever can interfere with the light reflecting from the sample surface. To minimize this effect, we reduce the average spectral coherence of the laser over time by dithering the laser current at ∼200 kHz.

2.1.2 Fabrication of fiducial marks

In order to stabilize the AFM instrument, the tip position must be referenced to the sample, which requires a scattering object on the sample surface to produce a backscattered signal. The simplest way to do this is to deposit and melt beads on the surface (Figure 2.2, a). However, beads stuck to the surface in this way move slightly and also produced a smaller backscattered signal compared to silicon posts [44, 45]. For best results with the AFM, we fabricated 1-mm^2 arrays of silicon disks (radius $\sim$ 250 nm, height $\sim$ 60 nm) in 10-μm grids on clean glass cover slips. The post size we require is slightly too small to be fabricated using optical lithography— if the posts are too large in diameter the backscattered signal will have a flat region— so it must be fabricated using electron or focused ion beam techniques. It is possible to directly write the posts onto resist deposited onto the glass (Figure 2.2, b), and for some applications this may be the best option. However, it suffers from two issues. First, it is an inherently serial technique, as each pattern must be individually written by the electron beam. Second, it has the potential to leave residue from the resist on the surface, which can interfere with sample deposition or coupling to the surface.

Therefore, we generally prefer a shadow mask technique, where the silicon is evaporated through the mask onto the slide. The masks are made from x-ray windows (1.5 $\times$1.5 mm, 100 nm thick, Silson, Blisworth, Northampton, England). There are two techniques for making a shadow mask. The first is to write the pattern into a resist on the window, develop it, and etch the window away. However, it is faster to directly write the holes into the window using a focused ion beam (FIB) instrument (Nova NanoLab, FEI, Hillsboro, OR), which uses a beam of gallium ions to remove material. The FIB is incorporated into a scanning electron microscope for inspection. The ions charge the fragile window to the point that it explodes (Figure 2.3, a), so we sputter gold onto the window before this step. The thin layer of gold is sufficient to diffuse the charge, and we are

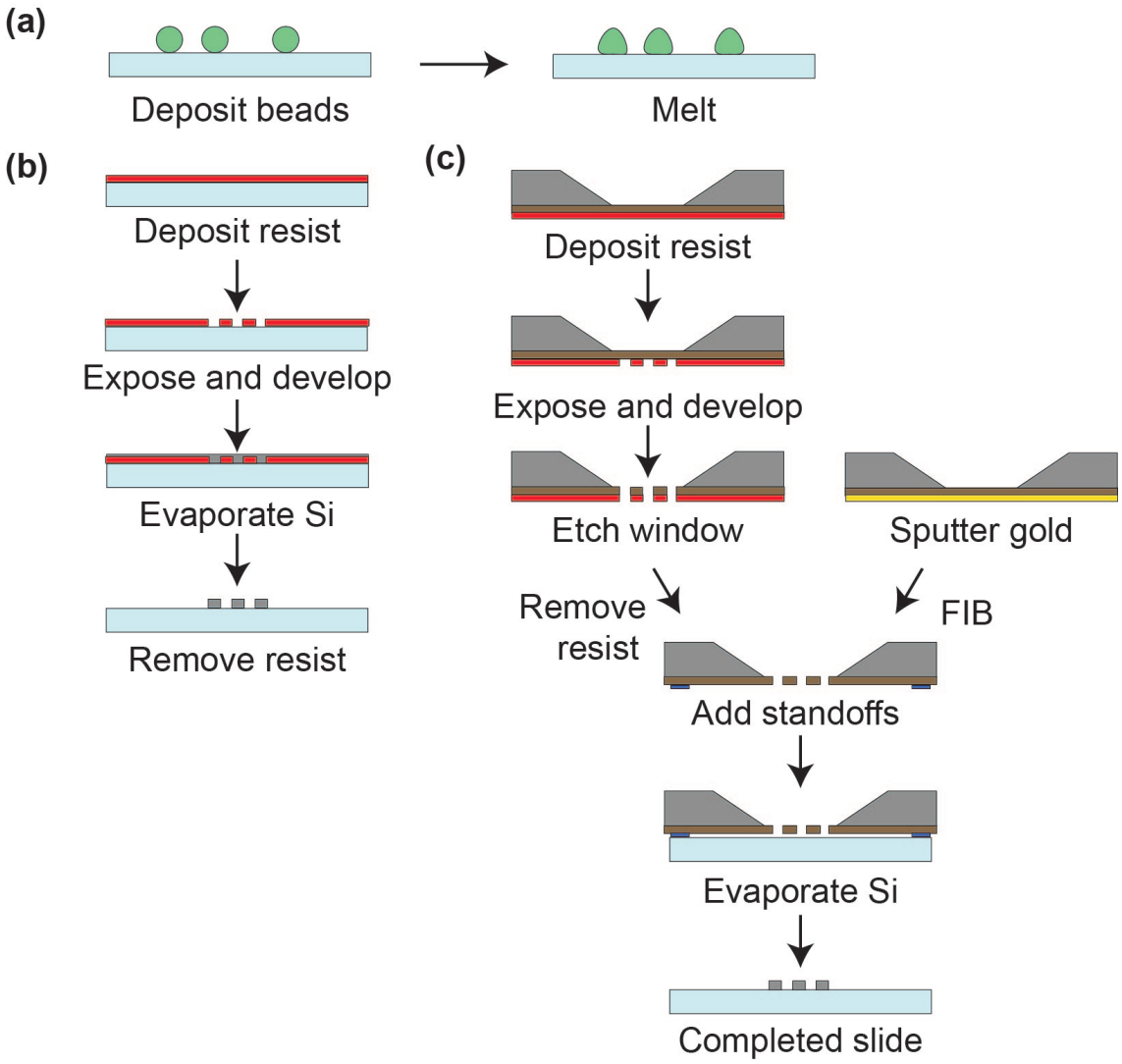

Figure 2.2: Summary of techniques for adding fiducial marks to surfaces. (a) In the stuck-bead technique, a solution of beads is added to the surface and the slide is heated to melt the beads onto the surface. (b) In the direct-write post technique, a resist is used directly on the sample surface. This resist is exposed with an electron beam, silicon is evaporated, and the resist is removed. (c) In the shadow-mask technique, an x-ray window is used as a shadow mask through which to evaporate silicon. The holes in the mask are made either through a resist or using focused ion beam milling.

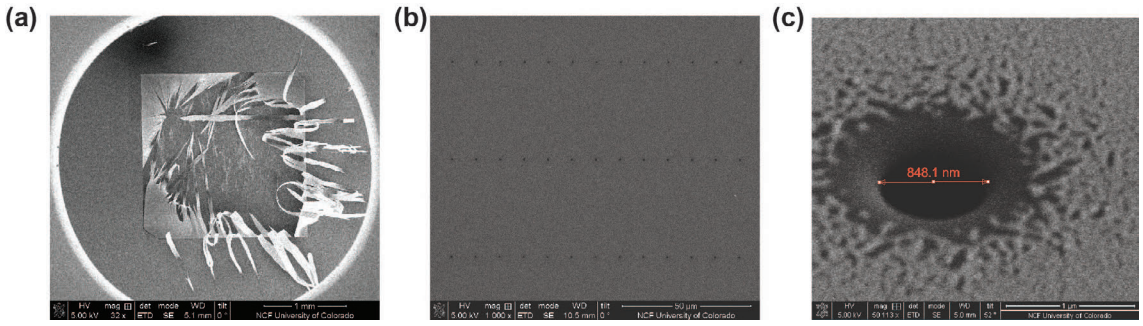

Figure 2.3: Fabrication of shadow masks from x-ray windows. (a) The focused ion beam can cause the thin mask to charge and explode. This effect can be avoided by adding a thin layer of gold to the mask before patterning. (b) Mask patterned with an array of holes. (c) Individual hole after milling, seen at an angle, and showing diameter of $\sim 1\mu$m. Remnants of the gold coating can be seen around the outside of the hole in this image.

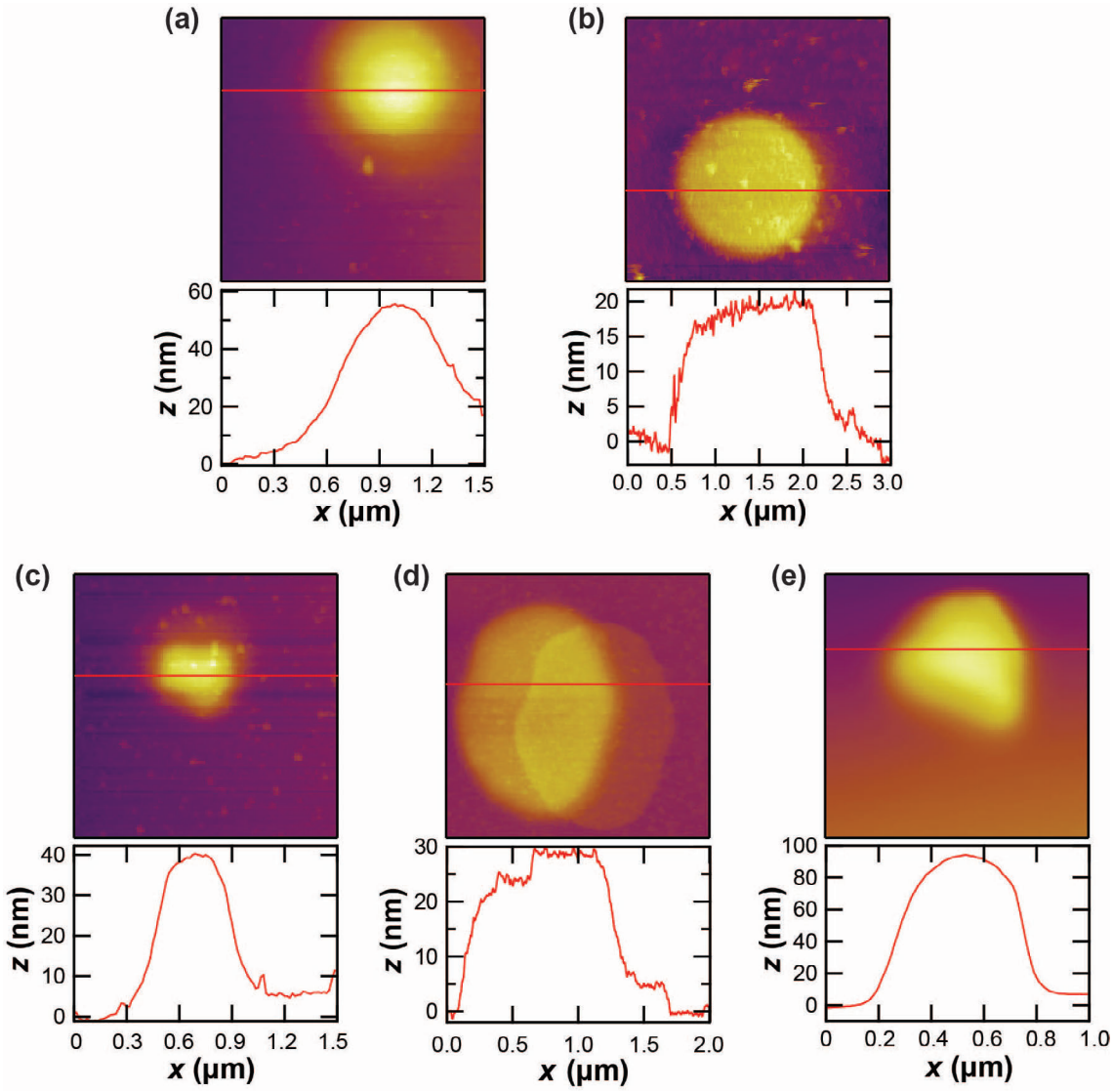

Figure 2.4: Gallery of AFM images of posts that produce good and bad backscattered signals. (a) The ideal post is just under 1μm in diameter (FWHM) and approximately 60 nm tall. (b) A post that is both too short and too wide; this one was almost completely non-reflective. (c) This post was too short and small. (d) This post produced poorly-shaped signals; it appears that the mask slipped during evaporation, causing a double post. (d) This post was too tall, and also produced signals that could not be used.

able to pattern an array of holes (Figure 2.3, b, c). We use the runscript feature on the FIB to create the patterns; an example of the scripting code is included in Appendix A. On the FIB, there is a tradeoff between speed and precision since higher powered beams are more difficult to focus well. A beam current of 0.92 nA and 1000×magnification produced good results, and each mask took approximately 20 minutes to mill.

Once the shadow mask is complete, we move on to the silicon evaporation step. Cover slips are cleaned using ethanolic KOH, using a recipe given in detail in [46]. We have also found that this step reduces the surface roughness of the glass cover slips, which can be critical to achieving good imaging results. We want to press the cover slips directly up against the holes in the mask. However, if we did this, the mask would stick to the cover slip and break when we tried to remove it. We therefore fabricate standoffs onto the mask with one of two techniques. The standoffs can be fabricated using a simple photolithography, with the photoresist SU-8 [37]. Alternatively, they can be drawn on with permanent (Sharpie) marker. We have found that three layers of marker, with a 1 minute bake in between layers, makes acceptable standoffs, though repeatability using this technique has not yet been established. Once standoffs are in place, the mask is put in a jig that holds the cover slip up tightly against the mask without slipping and mounts in the evaporator. Then we evaporate 60 nm of silicon through the holes in the mask onto the cover slip. Posts that are too big or too small, as shown in Figure 2.4, do not produce useful backscattered signals. Finally, we inspect the results in an optical microscope. By using this technique, we can create stable position reference marks for our experiment.

2.1.3 Mechanical system and passive stability

The ultrastable AFM was built on a modified optical microscope frame, with the AFM mounted on the condenser arm [35, 37]. Tip and sample motion were separately controlled using a pair of closed-loop 3D piezoelectric (PZT) stages (P363.3CD and P733.3DD, Physik Instrumente). The internal servo loops of these can be tuned to optimize their response under the typical load. The sample PZT stage was mounted on an ultrasonic substage (M-686.D64, Physik Instrumente),

which was quiescent during AFM and optical imaging but allowed for coarse motion over large areas (10×10 cm^2) with 0.1-μm repeatability. Using this ability, we could image over large areas ($\sim$1 mm^2) by patching together 30×30 μm^2 fields.

Passive stability was important to bring the noise down to a level that we could manage with the stabilization technique. Furthermore, motion in the mechanical loop from the tip to the sample (Figure 1.1) results in real motion of the tip on the sample that is identical to changes in topography. Typically, it is best to reduce the length of this loop, but in our proof-of-principle instrument it was relatively long. In particular, the condenser arm seemed to have a resonance at 20Hz that caused vibrations on the tip. We tried many different unsuccessful techniques to reduce the noise at 20 Hz, including placing weights onto the table and the AFM microscope itself, tuned mass dampers, and recabling the system with smaller BNC cables to reduce vibration traveling through them. However, a few interventions turned out to make a big difference in the noise. The set screw shown in Figure 2.7 is critical to achieving low noise. We also replaced the baseplate of the microscope with a more substantial version. This helped the noise substantially, as shown in Figure 2.5.

Originally, the entire instrument was enclosed in a heavy acoustic box mounted on the optical table made of layers of plastic, lead, and foam. The floating pneumatic optical table minimized floor noise. However, we found that the acoustic box walls were affecting the performance of the optical table, leading to added noise at low frequency, a result that was confirmed with an accelerometer (Vibration Analyser VA-2, JRS, Mettmenstetten, Zurich, Switzerland, Figure 2.6). This could be due to the sides of the box acting as a drumhead, to the entire box working as a "sail" to push the table, or by the raised center of mass making the table unstable. Before the replacement of the column, the box helped, but once the column was stronger, removing the box made the low frequency noise better. Currently we simply use curtains to block light and dust. Where space and money permit, the best solution would likely be to build a soundproof box anchored to the floor around the entire optical table.

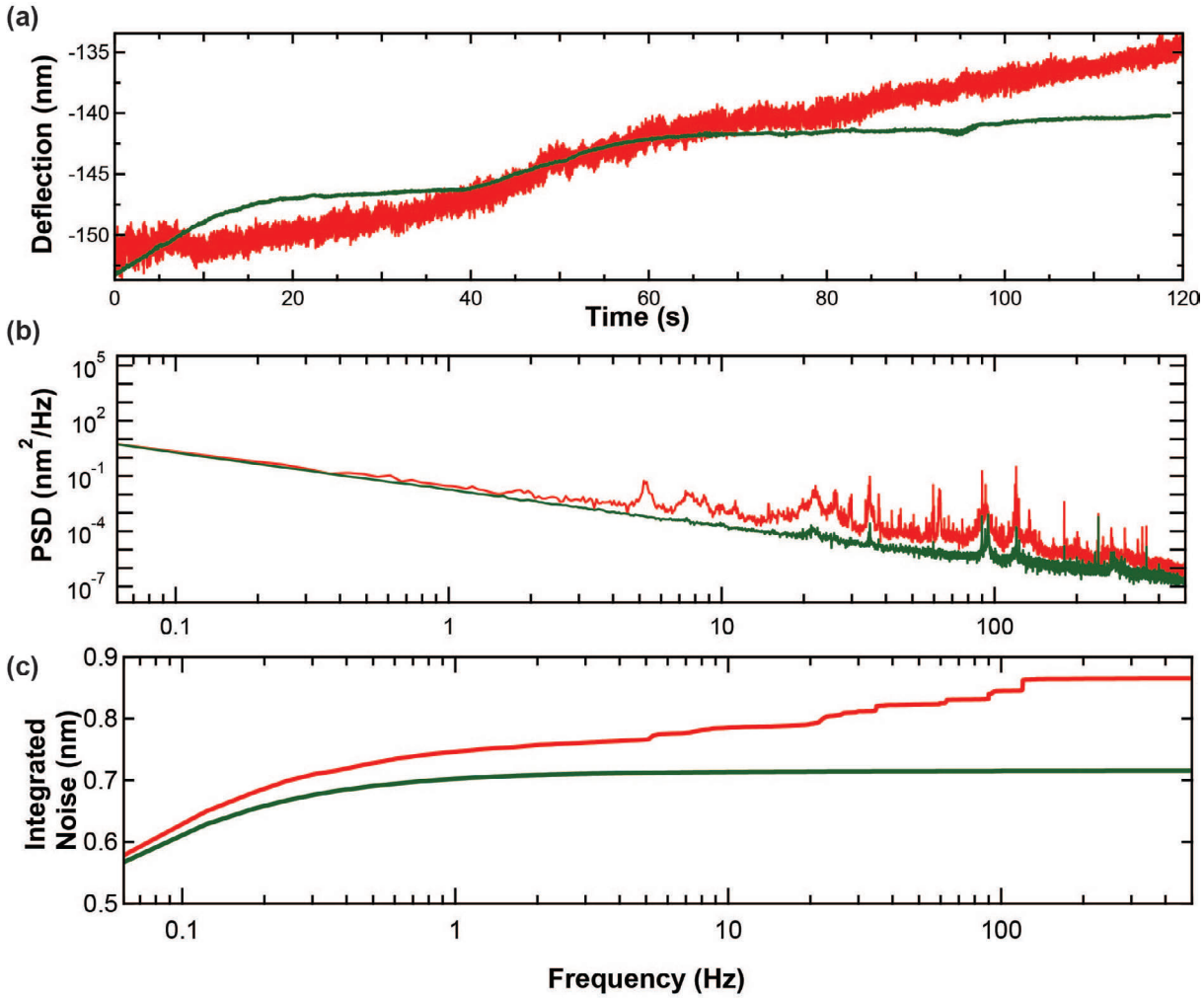

Figure 2.5: Reduction of noise with new robust column. (a) Deflection signal of the column with the tip engaged with the surface before (*red*) and after (*orange*) replacement of the original microscope column with a stronger one shows clear reduction in noise. (b) Power spectral density of the traces in (a), showing spectral properties of noise reduction. Peaks near 5, 20, and 100 Hz were especially affected.

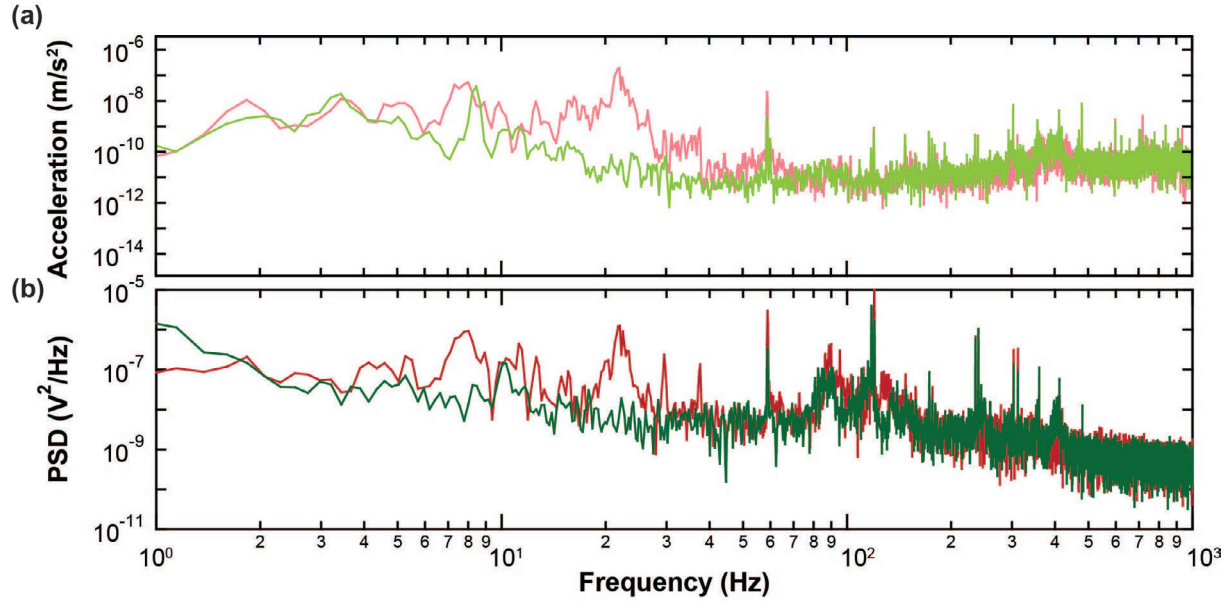

Figure 2.6: Reduction of noise without soundproof box. (a) Accelerometer data on the table with the soundproof box on (*pink*) and off (*green*) shows that the box added noise, especially around 20 Hz. (b) Power spectrum taken with the tip on the surface (*red*, with box and *green*, without box) confirms this result.

2.1.4 Fluid Cell

Biophysical experiments are done in liquid at relatively high salt concentrations (e.g.,150-300 mM KCl). To contain the fluid around the sample, we used a mechanically rigid fluid chamber with a sample holder on the bottom and a tip holder comprising the lid. Stabilities of the air-glass and the glass-water interfaces are important to assure a stable signal from the cantilever deflection laser. A major challenge in moving from operation in air to operation in biological buffer solution was to develop a robust method for holding the tip and allowing optical access to it. The original design (Figure 2.7, a) we used had two glass windows held together, and to the metal part of the tip holder, with glue (353ND, Epotek, Billerica, MA). However, glue expands when exposed to water, especially salty water. This expansion caused the window to move, which in turn caused extreme movement of the deflection laser on the QPD (Figure 2.7, c). Attempts to seal the epoxy joint with silicone helped remove this effect at first, but the joint ultimately still failed. We therefore redesigned the holder to use a single window attached to the metal support by a frit, which is a low-melting-point glass (Figure 2.7, d, e). Our custom-built fluid chamber was made of titanium (Figure 2.7, a), which is resistant to corrosion. Further, its thermal coefficient of expansion (8.6×10^{-6}/ ℃) matches that of soda lime glass (8.5×10^{-6}/ ℃). Thus, we can make a rigid bond between the glass and the titanium using a frit [G1009 (Vitta); thermal coefficient of expansion (9.0×10^{-6}/ ℃)] without fracturing the glass upon thermal cycling. To make the bond, we place the clean titanium-glass assembly in an oven in an angled jig so that the bond is flat. We turn the oven temperature up to 500 ℃, let it heat up for one hour, then turn the oven off and let it cool to room temperature with the door closed. We then attach the spring, which is spot-welded onto a tapped post, and seal the joint between the spring and the tip holder (Repro-Rubber Thin Pour, Flexbar, Islandia, NY).

The tip is mounted into the holder by lifting the spring, either with tweezers or with a tool that was designed for this purpose, then placing the cantilever chip into its pocket and lowering the spring. Care must be taken that the chip is properly aligned with the registration marks. If

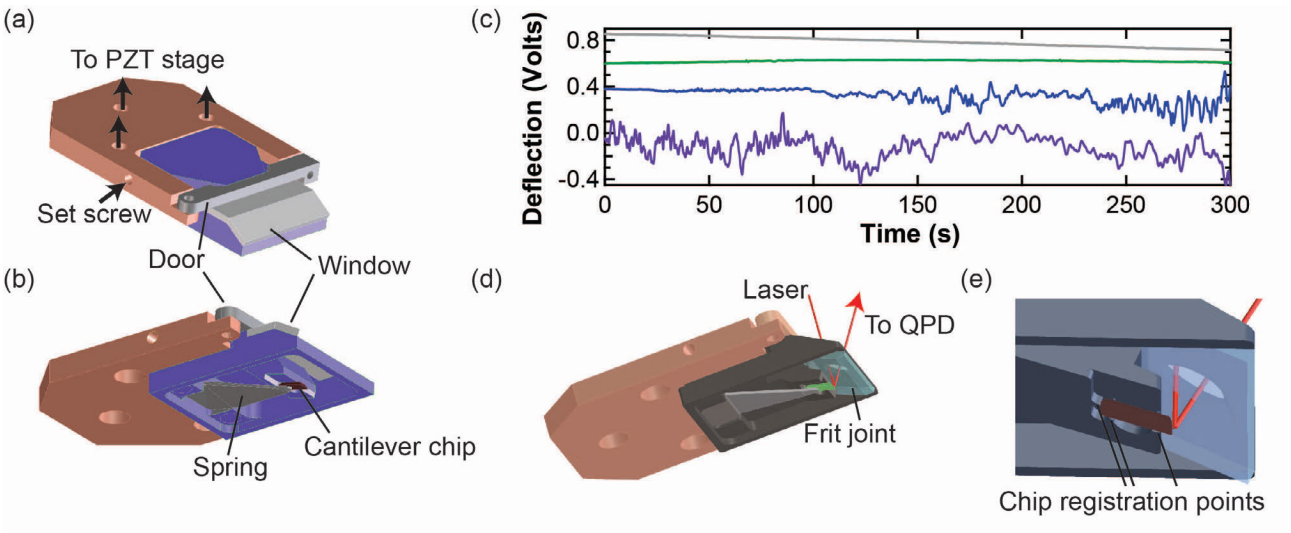

Figure 2.7: Evolution of tip holder design. (a) Overview of tip holder system. The removable tip holder (*purple*) slides onto a mounting plate (*salmon*) and is secured by a door (*grey*) and a set screw. In this first-generation holder, the window was made of two pieces of glass glued to each other and to the tip holder, which was made of aluminum. (b) View of the same design from below. Here the spring (*grey*) can be seen holding the cantilever chip in its pocket. (c) Instability caused by glue on window. The noise on the deflection signal in air (*grey*) is similar to the first five minutes after wetting in fluid (*green*). However, during the second five minutes (*blue*), the fluid begins to soak into the glue, causing the window to move and introducing noise into the deflection signal, which remains during the third five minute segment (*purple*) and thereafter. (d) Redesigned fluid chamber for stable operation in liquid. The tip holder, now made of titanium, attaches to the same mounting plate and uses the same spring mechanism. However, the window is now a single piece of glass held to the metal with a frit. (e) Expanded view of the chip in its pocket with the spring removed shows registration points for repeatable mounting.

the chip is placed too far back (sitting on the registration posts), it can break when the spring is released. The spring tightness can be adjusted by removing it and carefully bending it to the appropriate angle. The tip holder then slides onto a mounting plate on the bottom of the PZT stage, and is secured by a door and a set screw. These screws should be snug, but not too tight, as torques above 0.25 N-m can damage the PZT stage.

There are several versions of the tip holder. Because the optical lever QPD had a limited range of motion, we had a difficult time getting the optical lever signals onto the QPD near the center, so that we would be in the range of voltages we can measure ($\pm$10V). In order to solve this, we made tip holders with extra angles in addition to the original 15° mount. This way, we can mount a tip at a different angle to get the optical lever signal on scale. The TR-400 cantilevers seem to work best with no additional angle, while the Biolevers work best with a 4° mount. Additionally, the Biolever Mini has a thinner chip than most other AFM cantilevers, so we made a tip holder specific to that chip.

The sample holder is also an important part of the fluid containment. These were originally made from aluminum, which corroded in the salty buffer solution. For this reason, we began using titanium instead. The sample is a 22×22 mm glass coverslip, which is mounted over the hole on the sample holder with wax (Crystalbond 509) at 95°C. The wax is slightly soluble in water, so it is critical that it is completely underneath the coverslip and not exposed to buffer. Otherwise, the buffer will eventually be contaminated. Once the sample is mounted, attach the Teflon washer, and seal with Repro-Rubber.

Proper cleaning of the tip and sample holders are critical to ensuring good operation of the AFM. The tip holder is typically rinsed with alcohol (ethanol or isopropanol) and deionized water, repeated three times, between uses. Hold the tip holder with tweezers or other clean tool during this process; we have found that contamination from gloves (even powder-free ones) can be washed into the tip holder. Occasionally small pieces of dust or other contamination are apparent on the tip holder window, which can be detrimental to the optical lever measurement. These are removed by wiping with a lens tissue wrapped around a toothpick, sometimes dipped in window cleaner

(Windex). If window cleaner is used, the tip holder must be very thoroughly rinsed with deionized water afterward. To clean the sample holder, the sample must first be removed. This can be done gently by placing the sample holder on the hot plate at 95°C with a stack of Teflon nuts pressing on the sample from the bottom. The mounting wax is very soluble in acetone, so can be easily removed, and the Repro-Rubber residue can be rubbed off. The microscope immersion oil is more difficult to remove. Often we simply wipe off what we can, but occasionally it is good to wipe with the solvent EnSolv, which completely removes it. Once these coarse cleaning steps are complete, we sonicate in a hot detergent bath, then rinse three times with methanol and deionized water. We store the clean sample holders in sealed containers (*e.g.* petri dishes) to protect them from dust.

2.2 Software and FPGA control

An overview of the AFM calibration and control software is given in Figure 2.8. A comprehensive software package was critical to turning the ultrastable AFM from a proof of principle into a working instrument. The inputs to the software are the user controls along with the processed optical signals from the QPD electronics. The outputs are digital parallel control signals to the two three-axis PZT stages, and also to the coarse positioning ultrasonic stage. The software performs four basic tasks: (I) Initialize, prepare, and coarsely align both PZT stages; (II) calibrate the sample position, with the tip near the surface, as its presence changes the optical signal, but holding the tip far enough away from the surface to prevent it from uncontrolled contact with the surface; (III) calibrate the tip position and force; and (IV) allow the user to adjust parameters, view information about servo status, and perform AFM tasks such as imaging and force spectroscopy. Several output files may be written during this process; they are described in Appendix C.

In this section, I begin by discussing the FPGA-based crosstalk calibration in depth (2.2.1), then present results showing how this improved the instrument noise characteristics (2.2.2). Sections 2.2.1 and 2.2.2 are adapted from Reference [38]. I then present some details about the operation section of the software (2.2.4), focusing especially on the force spectroscopy program (2.2.5), as this was an area where novel techniques were applied, and therefore novel algorithms were necessary.

Finally, I briefly discuss our high-bandwidth data collection and spring constant calibration (2.2.6).

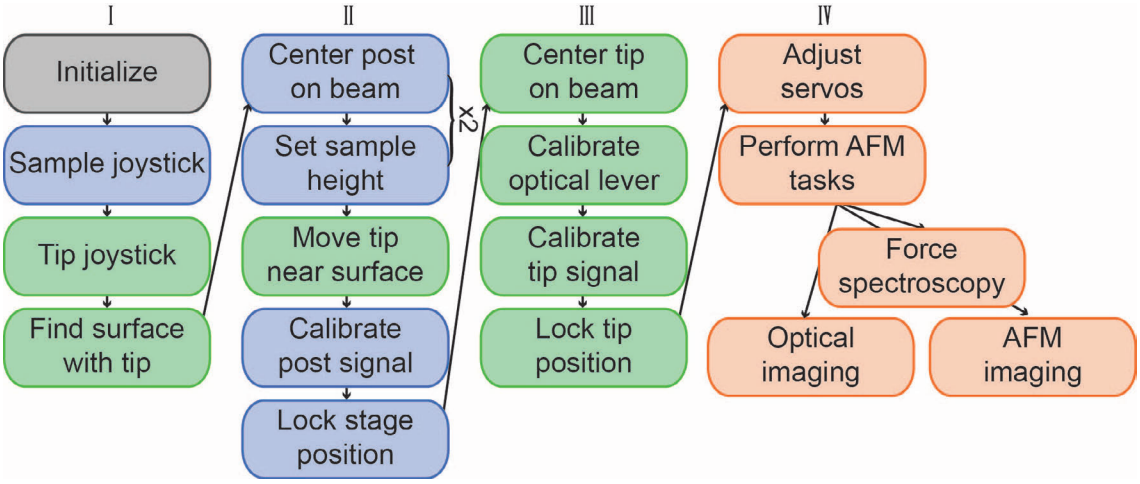

Figure 2.8: Block diagram of AFM calibration and control software. After initialization and coarse alignment steps (I), the sample is calibrated and position locked (II), followed by the tip (III). Finally, the user can adjust the system parameters and perform AFM tasks (IV).

2.2.1 FPGA-based crosstalk compensated calibration

To fully exploit the high bandwidth provided by laser-based detection, the feedback rate should be limited by mechanical responses (e.g., PZT stage). In the first iteration of backscattered detection [45], the feedback rate was limited to 100 Hz by a software-based control algorithm. Additionally, this software-based feedback did not provide deterministic timing; disk writes, operating system interrupts, and graphical updates to the user interface led to timing glitches that degraded performance. To overcome these issues, we developed real-time, deterministic control using a field-programmable gate array (FPGA) for higher feedback rates that significantly improved lateral stability and enabled more sophisticated signal processing, yielding highly accurate orthogonal scanning. Specifically, we used the position information from the back-scattered detection in an FPGA-based feedback loop. We controlled the sample position with a 3D, direct-drive, closed-loop PZT translation stage (Physik Instrumente, P- 733.3DD, E-710). Feedback was performed using data acquisition and control software (National Instruments LabVIEW 8.5 or 2009). The

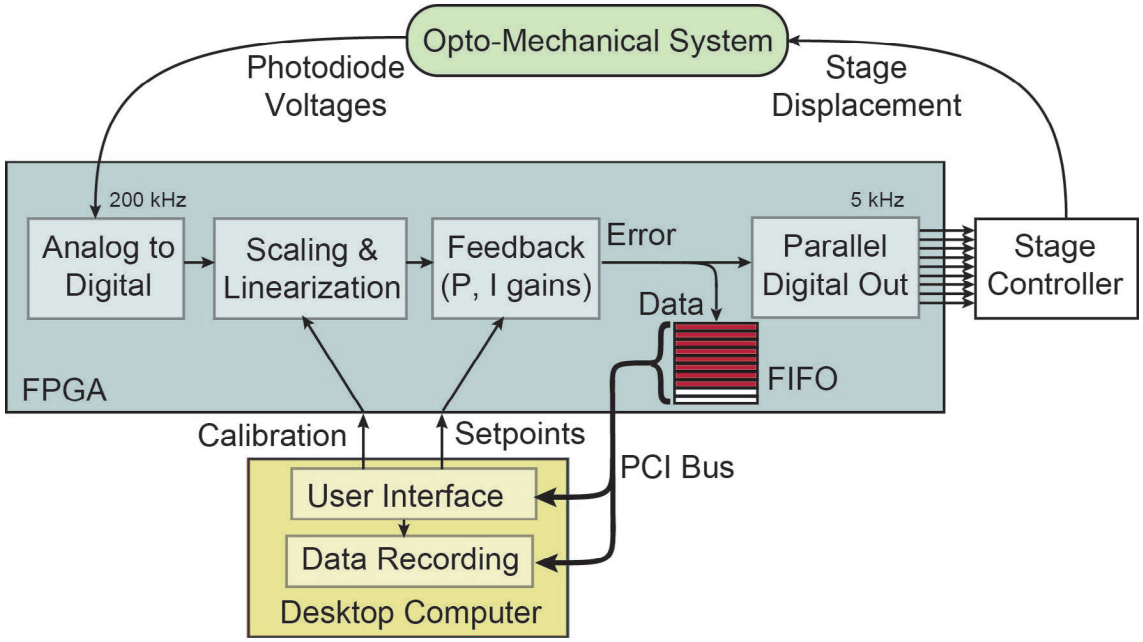

Figure 2.9: Block diagram for FPGA feedback control. The FPGA digitizes incoming signals from the opto-mechanical system. Then, linear algebra routines scale and orthogonalize the optical detection to allow accurate feedback control on the separate x, y and z axes of the stage. Parallel digital output allows for high bandwidth communication with the stage controller. The FPGA passes the raw and scaled data to the host computer for display and recording. The host computer provides calibrations and overall interactive control via changes in the setpoints, and records the full bandwidth data for subsequent analysis. From Reference [38]

FPGA chip (Xilinx Virtex-II or Virtex 5) was contained in a card (National Instruments PCI-7833R or PXI-7854R) along with memory, analog-to-digital and digital-to-analog converters, and input/output resources.

An FPGA chip mimics a dedicated patterned microchip by arranging blocks of logic to perform the requested task in hardware. Because it has a 40-MHz clock separate from the PC clock, the FPGA executes programs both quickly and with well-defined (i.e. deterministic) timing. As shown in Figure 2.9, all the functions required for the feedback loop were downloaded to the chip. The entire feedback loop was independent of the slower PC programs, which therefore allowed it to operate with higher feedback rates and deterministic timing. The limited logic resources of the FPGA chip constrain the complexity of the functions in the feedback loop. In the first implementation under LabVIEW 8.5, integers (64 bit) were used for on-chip calculations, as traditional floating point operations were not supported by the NI FPGA development software. Under LabVIEW 2009, this restriction was relaxed somewhat with the introduction of fixed-point numbers on the FPGA. Operations that are not time-sensitive (e.g., user interface, writing data to disk), executed on a desktop computer (Dell Dimension, 2.66 GHz Intel Core2Duo, LabVIEW 8.5 or LabVIEW 2009 under Windows XP, 7 or Vista).

A major novel task for the software was to align and calibrate first the sample, then the tip. We aligned the 845-nm laser focus laterally to a silicon disk (fiducial mark) on the cover slip by using either an automated routine or a manual one. The automated routine found the center by moving in each direction, then fitting $V_x(x)$ or $V_y(y)$ to its expected functional form, the derivative of a Gaussian. When we manually laterally align, we find the center by moving the fiducial mark until the voltage V_x or V_y is at the same value as it is far from the fiducial mark. Alignment in x and y are iterated until we converge on a solution. The height of the post relative to the tip focus is critical, not only to the calibration of the tip, but also to the calibration of the tip to its laser beam. The height is aligned by moving the post in z through the beam focus, and a position relative to the maximum scattering is selected. The correct height is determined empirically, by trying several heights until one is found that produces good sample and tip calibrations. A height

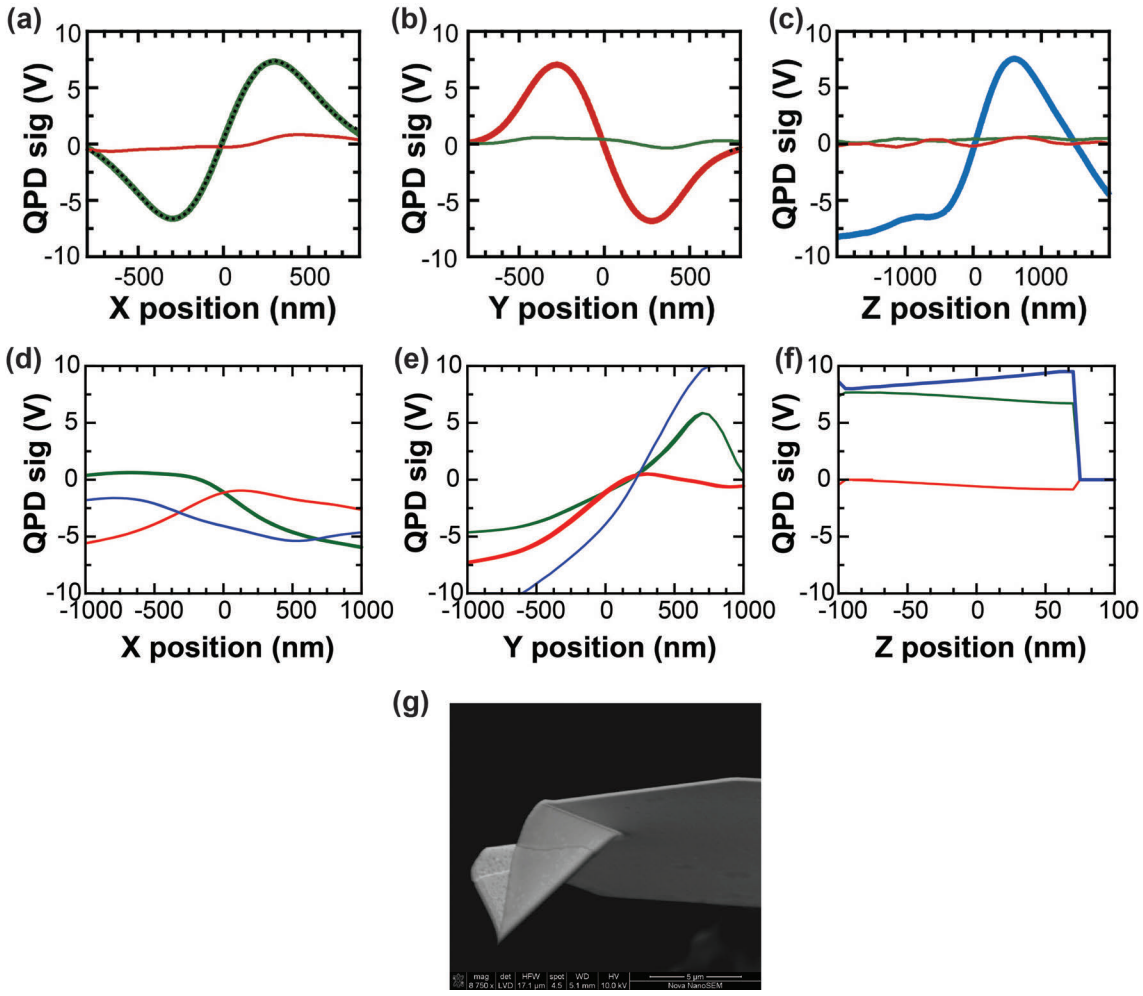

Figure 2.10: Centering signals on post and AFM tip (long Biolever, Olympus). (a)-(c) Signals on post as it is moved through the beam in x, y, and z, respectively. From Reference [37]. (d)-(f) Signals on tip as it is moved through the beam in x, y, and z, respectively. In the z direction, the tip touches the surface at about 70 nm. Notice the extra crosstalk and complexity in the tip signal. This is due to the asymmetric shape of the tip, as seen in the SEM image (g).

of 750 nm in the positive direction from the maximum scattering is a typical starting point. If a height cannot be found that produces good sample and tip calibrations, the lens that determines the relative heights of the two beams can be adjusted. We iterate lateral alignment and vertical alignment at least twice. Examples of post alignment signals are shown in Figure 2.10, a-c [37]. Since the presence of the tip can affect the sample signal, we move the tip near the surface, but hold it slightly away from the surface so that it does not crash. The calibration data itself is collected with a 3D raster scan through a cube, typically 11 steps on each side and $200\times200\times100$ nm^3 which constituted the calibrated range. Performing sample calibration took <1 min. We then fit to a polynomial, as described in detail below, and locked the sample position while we aligned the tip with respect to its laser.

Tip alignment was achieved by dithering the AFM tip along each axis sequentially and changing the center position of the dither. The dither curves in each axis have an optimal location where the calibration is possible. In general, the optimal shapes for these curves must be determined empirically for each type of tip. However, there are three criteria which seem to help produce the best calibrations. First, that the slope of at least one voltage response (V_x, V_y, or V_z) for each axis must have sufficient sensitivity. It is not required that this be the "on axis" response, since the calibration is completely symmetric. Second, the slopes should be unique for each axis of motion. For instance, if, when moving in x, V_x has a positive slope, V_y has a positive slope, and V_z has a negative slope, this particular qualitative pattern should not be repeated for either of the other two axes. Finally, the inverse of each response along each axis (*e.g.* $x(V_x)$ or $y(V_z)$) should be single valued, so that there will be a function that fits the data. An example of the optimal location for a Biolever is shown in Figure 2.10. A typical calibration range might be 20×20 nm laterally, and range from 10-110 nm above the surface. We acquired raster scan data in this range, as for the sample calibration, and fit it to the 4^{th} order polynomial.

The computational power of the FPGA allowed not only fast feedback but more complex mathematical operations. We took advantage of this computational power to minimize crosstalk using a routine adapted from optical trapping applications [47]. Previously, each position (x, y,

z) was parameterized only in its corresponding voltage. For instance, V_x used a polynomial of the form

$$x(V_x) = \sum_i a_i V_x \tag{2.1}$$

that does not take off-axis or cross terms into account. However, this was not generally a good simplification, particularly for the tip, which can have a very anisotropic shape and also is typically mounted at an angle of 10–15°. The 3D raster scans for tip and sample data described above yielded the backscattered signals (V_x,V_y, V_z) corresponding to stage movements could be scaled using a parameterization of the form

$$x(V_x, V_y, V_z) = \sum_{i=0}^{i+j+k=4} a_{ijk} V_x^i V_y^j V_z^k \tag{2.2}$$

for each axis x, y and z. Coefficients (a_{ijk}) were determined by a nonlinear least-square fitting routine to the data. Scaling the data at high speed according to this complex parameterization — 35 coefficients per axis for a fourth-order fit — was made possible by the high clock rate of the FPGA chip. The feedback signal was calculated with set points controlled from the host computer, which allows for scanning and, more broadly, interactive user-driven control. We used a standard proportional (P) and integral (I) control loop with$1 \leq P \leq 2$ and $0.01 \leq I \leq 0.02$. Control signals were sent directly to the stage controller via a 16-channel, fast (5 kHz) parallel output interface.

As the feedback loop executed, the raw and scaled data were written to first-in, first-out (FIFO) memory structures. Subsequently, the non-deterministic software (LabVIEW) running on the desktop computer read from this FIFO enabling collection of lossless, high bandwidth data.

2.2.2 Stability improvement with FPGA control

After first establishing the high lateral sample stability provided by FPGA control (10 pm), we next demonstrated rapid stabilized scanning (2 ms step duration). Finally, we show excellent orthogonal scanning over a large area using a computationally intensive, crosstalk-compensation algorithm. All of our results were determined by "out-of-loop" detection of the fiducial mark using

the second detection laser. Thus, they are an accurate representation of the true performance within the differential measurement reference frame established by the pair of detector lasers.

Implementation of FPGA control significantly improved lateral stability performance (Figure 2.11, a, color). We compare these new results to prior results using slower (100 Hz) software-based feedback (Figure 2.11, a, grey). To quantify stability, we monitored the position of the fiducial mark for 100 s. We boxcar averaged the data within a 50 ms window, which preserves a 10 Hz frequency component. Next, we decimated the data to 20 points per second. This analysis yielded a standard deviation of 10 pm in both x and y. These results are more than a threefold improvement over prior results of 33 and 42 pm in x and y, respectively, and exceed the manufacturer's specifications. A complementary analysis based on fitting histograms of the position records yielded identical results (Figure 2.11, b). Thus, our lateral stage control is sufficient for studying single atoms under ambient conditions and an order of magnitude smaller than the length of the OH bond in a water molecule (100 pm) [48].

FPGA-based control provided enhanced stability over a broad frequency range (Δf = 0.1–50 Hz). To demonstrate this improvement, we plot the power spectral density (PSD) of the stabilization records (Figure 2.11, c). At low frequencies (<20 Hz), we achieved PSDs that were an order of magnitude better than prior results, in agreement with the approximately threefold improvement in real space data, based on simple dimensional considerations (PSD is in units of nm^2/Hz, and $32 \approx 10$). An excellent alternative metric for calculating stabilities is to integrate the PSD within a specified bandwidth. We computed the integrated noise from 0.1 to 50 Hz, a broadly useful bandwidth for SPM and optical trapping experiments. The standard deviations were 30 and 28 pm for x and y, respectively. Calculating the equivalent metric on real-space data yields similar results as required by Parseval's Theorem. The results presented in Figure 2.11 used a proportionality gain of 2, which appears to have caused some excess noise at ~200 Hz. We have yet to fine tune the feedback loop parameters, and currently use only proportional and integral gain. Feedback loop parameter optimization should enhanced performance.

Performance of advanced optical trapping and AFM experiments are improved by rapid,

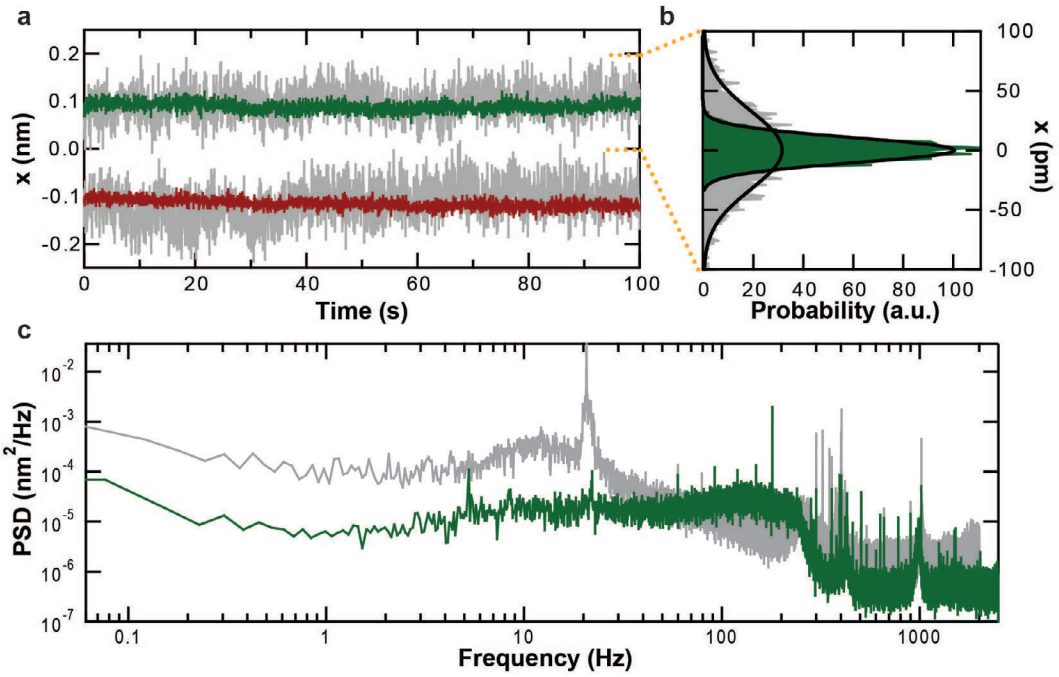

Figure 2.11: Demonstration of improved performance provided by FPGA-based feedback control. (a) Lateral stabilization records (x, *dark green*; y, *dark red*) achieved with 500-Hz FPGA control in comparison to control achieved with 100 Hz software-based feedback (*light grey*). Both data sets are filtered to 10 Hz and offset for clarity. (b) Histograms of the x signal corresponding to the FPGA-based feedback and the software-based feedback are well fit by histograms with standard deviations of 10 and 33 pm, respectively. (c) Power spectral density analysis shows improvement in stability over a range of frequencies from 0.1 to 50 Hz (same color coding as in a). From Reference [38]

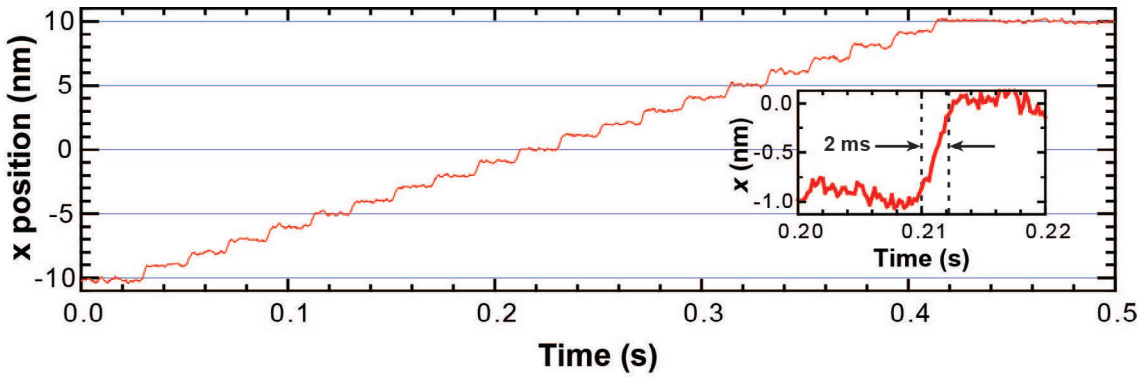

Figure 2.12: Fast stepping enabled by parallel FPGA feedback control. (a) A record of sample position from a series of 1-nm steps filtered to 2 kHz. Sample position, independent of the servo-loop, was measured with the 845-nm laser. (Inset) Rise time for requested motion was 2 ms with the total step completed 3 ms after the request. From Reference [38]

deterministic motion of the sample. For optical traps, such stage motion can maintain constant force on molecular motors [49] Higher bandwidth stage motion provides more accurate control of force. For AFMs, stepping is the basis of scanning for image acquisition and optical detection of sample motion provides for stabilized scanning [45]. FPGA-based control enabled both rapid communication with the PZT stage controller and rapid stabilized stepping. As shown in Figure 2.9, communication between the FPGA and the stage controller was done using a parallel digital output. This communication protocol led to a 1 ms delay between the requested motion and its onset (data not shown). These requested changes in the stage position led to a staircase of 1 nm steps that were well resolved even at data filtered to 2 kHz. The nominal rise time (10-90%) per step was ∼2 ms (Figure 2.12, inset), which approaches the fastest step our stage (resonance frequency ∼1000 Hz) could be expected to achieve. Thus, the overall delay between requesting and completing a step was 3 ms. We expect that optimization of the control code of the FPGA, faster stage controllers, and better feedback parameters can improve this delay by a factor of two. Further improvements will require stiffer stages with higher resonant frequencies.

An ideal ultrastable measurement platform should provide both excellent stability in 3D about a particular location and accurate orthogonal scanning in all axes. Yet, optical crosstalk can lead to inaccurate positional control; motion in x leads to voltage changes in all three detection axes. Additionally, the QPD detection axes may not be perfectly aligned to the lateral axes of the PZT stage. More significantly, crosstalk increases as the reference mark is moved further out of the laser focus. Such crosstalk is well known from optical trapping experiments [47, 50]. To address these issues, we adapted a previously published control algorithm [47] for use on an FPGA. Because of the computation speed provided by FPGA control, we were able to implement this cross-talk compensation algorithm without degradation of feedback bandwidth. Crosstalk compensation significantly improved control of the stage position, particularly near the edges of the calibrated region, where discrepancies were more pronounced. To demonstrate the degree of improvement, we compared this difference in scanning control between linear fits ($x = a_1 V_x + a_0$) and fully cross-talk compensated detection (Equation 2.2) by moving the stage in a grid of points with 10 nm spacing

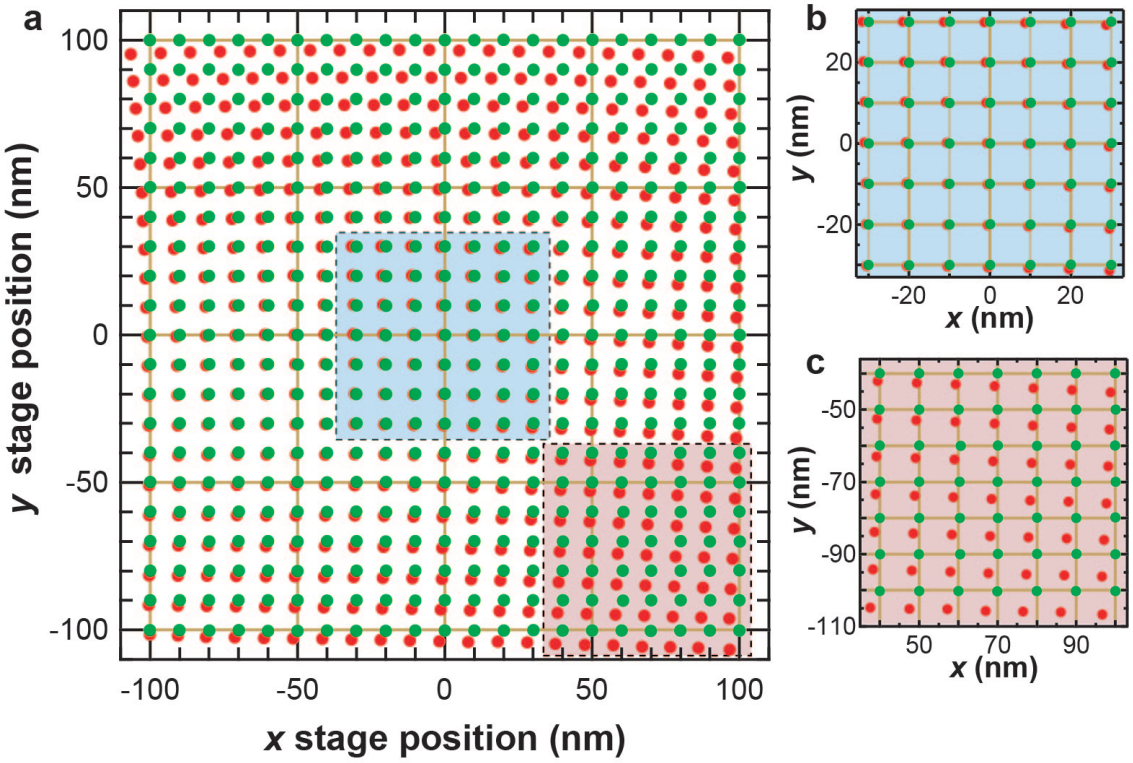

Figure 2.13: (a) Two-dimensional scanning with (*green circles*) and without (*red circles*) cross-talk compensation. Sample position, independent of the servo loop, was measured with the 845-nm laser. (b & c) Enlarged plots of the center and corner regions, respectively. (b) Scanning within a restricted area near the origin leads to less crosstalk. (c) Highly accurate scanning far from the origin was achieved with crosstalk compensation (*green*) while uncompensated points are subject to large systematic errors (*red*). From Reference [38]

over the entire 200×200 nm^2 calibrated range, pausing at each point for ∼100 ms, and recording the x and y position as measured by the out of loop detector laser. We computed the average error (the difference between the requested and actual positions) in two regions. Near the center of the calibrated range (Figure 2.13, b, *blue region*), this test yielded an average residual error of 1000 pm using a linear calibration versus 54 pm using full cross-talk compensation, an ∼18-fold improvement. Near the corner of the calibrated range (Figure 2.13, c, red region), a similar analysis yielded residual errors of 5120 pm with the linear calibration versus 121 pm with the parameterization described in Equation 2.2, a >40-fold improvement. Thus, the crosstalk compensation software allows for precise and accurate scanning over a much larger area while maintaining excellent sample stability.

In this section, we demonstrated a robust, ultrastable measurement platform based on local optical measurements in conjunction with real-time FPGA-based control of sample position. This feedback scheme provided atomic-scale active stabilization even in the presence of the large external perturbations due to ambient operating conditions. The approach relied on precise optical measurement of sample position local to the measurement point. A FPGA-PCI card then rapidly processed these optically generated voltages into position and generated orthogonalized error signals. Communication occurred in parallel to the sample stage controller, allowing for rapid movement in all three axes. Furthermore, this control occurred in real time, buffered from the indeterminacies of the operating system and other interrupts. With this FPGA system, we achieved a threefold improvement over our prior software-based stabilization results. This degree of lateral localization stability (10 pm) represents an order-of-magnitude enhancement over the manufacturer's nominal (100 pm) resolution of the stage. We have also demonstrated the added benefit of a full 3D optical calibration for highly linearized and orthogonal control over a 200×200×100 nm^3 calibrated range. Looking forward, we expect that the intrinsically parallel and deterministic control provided by FPGA architecture will become increasingly valuable for future precision nanoscience applications, such as optically stabilized AFM, that demand real time control of many (> 3) independent axes. Moreover, as newer generations of FPGA-PCI cards become available, they will likely provide higher feedback bandwidths coupled with more reconfigurable logic blocks

that will allow for high-precision displacements over a larger dynamic range.

2.2.3 Calibration and control software overview

This section describes the structure and use of the main calling program "Top level flexible.vi" in greater detail. This program is set up as a state machine, with the user inputting the list of states to execute before running the program. An example of a set of instructions given to this program is shown in 2.14. Here, I describe each case that the user can choose from.

Initialize performs necessary initial tasks including starting and the FPGA vi and initializing the FIFO structures; generating the correct file structure and time stamp; and moving the translation stages to their starting positions. It should therefore always be run first.

Sample Joystick and **Tip Joystick** allow the user to move the sample and tip translation stages, respectively, in x, y, and z. This is usually used for coarse alignment, but is also used for complete lateral alignment in the case of the sample. The final position when the vi is stopped is written as an offset, so that future motion is referenced to it as zero.

Substage Joystick allows the user to adjust the large-area translation stage under the sample PZT stage. It is generally preferable, however, to call this program by running "Initialize Substage.vi" or "Recover connection to substage.vi" rather than through this menu; otherwise, there is sometimes a communication issue with the substage.

Stage manual height takes a curve $V_z(z)$ and allows the user to put a cursor on the curve to specify the desired height, which is determined by a desired distance to the maximum scattering, and updates the zero point for future programs.

Stage auto center and height uses fits to the derivative of a Gaussian to laterally center the sample position sensing laser (λ=845 nm) on the post, sets the height a user-specified distance from the maximum scattering, and repeats the lateral centering. It updates the zero point for future programs. This routine is sometimes used, but often we find that it is simpler to use the joystick program and manual height to perform this task by hand. **Autocenter tip** does the lateral alignment for the tip, but is currently not reliable enough for general use.

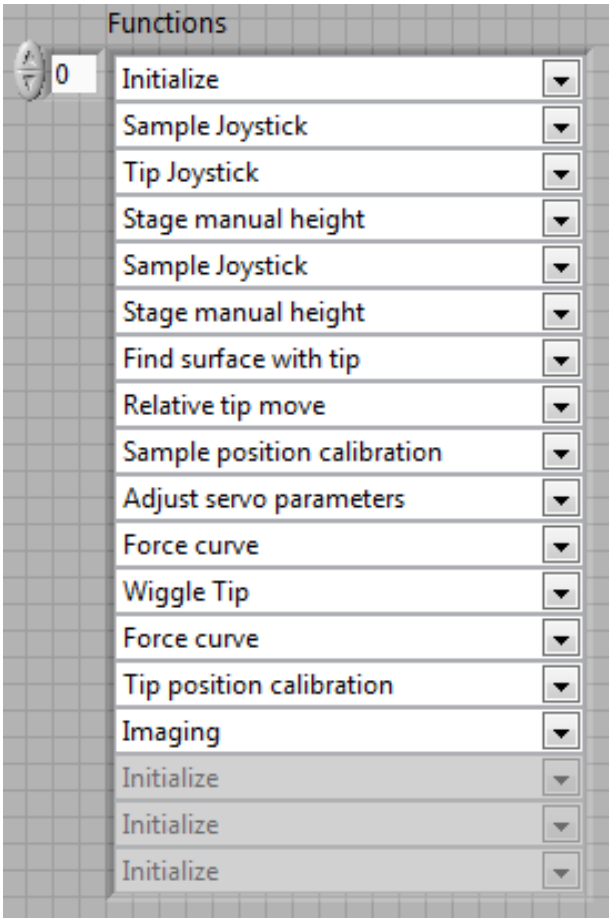

Figure 2.14: Screenshot of a typical set of instructions provided to the main calling program for full locked operation of the instrument.

Wiggle tip and **Wiggle Stage** are yet another method of aligning the tip and sample to the beams. They move the tip or sample, respectively, back and forth through the laser focus in each axis, and display graphs of V_x, V_y, and V_z as a function of whichever axis is being moved. (See Figure 2.10 for examples.) The user can adjust the center of this motion to align the tip or sample, which becomes the zero point for future programs. In typical operation, this is used for the tip, but not the sample.

Find surface with tip and **Force curve** both touch the tip to the surface and produce a measurement of the optical lever sensitivity. **Find surface with tip** should be used initially, when the tip starts out far from the surface. It takes one long force curve, then moves a user-specified distance from the surface and produces another force curve for the optical lever sensitivity. This avoids problems stemming from artifacts (described in Section 2.1.1) when the tip is above the surface. It also produces an error message if the surface is not found within the range of the translation stage, so that the user may make a coarse adjustment and try again.

Relative tip move and **Relative Stage Move** simply move the tip or sample a user-specified distance from its current position. "Relative tip move" is mainly used to move the tip to a safe height before sample calibration, as shown in 2.14; "Relative Stage Move" is not normally used.

Sample position calibration and **Tip position calibration** calibrate the sample and tip, respectively, to their usual position sensing lasers— λ=845 nm for the sample and λ=810 nm for the tip. They do this by the 3D raster scan and fitting algorithm described in 2.2.1. We have tried different orders of polynomials for these in order to balance the tradeoff between space on the FPGA chip and performance. Currently, they are both calibrated to a 4th order polynomial.

Tip Position Calibration with 845 and **Cal stage with 810** perform the same 3D raster scan and 4th order fit, but with the opposite lasers. The primary purpose for this is to generate out-of-loop stability data to assess performance of the instrument. In this type of assay, we would focus both beams on the same object (with the offset lens removed) and calibrate with both beams, then compare the measurements produced by the two beams. **Fake sample cal** writes "1" to all

calibration coefficients, which is useful for some assessment and debugging tasks.

Once the calibrations are complete, **Adjust servo parameters** allows the user to turn the servo loops on and off, and change the set points and gains. It displays graphs of measured position, requested position, and output, so the user can check the servo loop performance. It can also be used to write all of the servo loop data to a file.

User message displays a pop-up box with a message to the user, **Pass** moves on to the next instruction without doing anything, and **Stop** stops the program.

2.2.4 AFM operation

The AFM operation vis for operating in various modes share a common wrapper that deals with y motion, plotting, and saving. Within this wrapper, each type of imaging or force spectroscopy creates an x line scan. In the case of force spectroscopy, a force spectrum is created and dealt with as if it is an x line scan. This wrapper also writes to an info text file. Parallel loops keep track of user input and update servo parameters.

Lossless data collection using the FPGA is a critical task. It is complicated by the fact that the FPGA is collecting data very quickly (5 kHz), while the program writing the data goes much slower (100 Hz). The FPGA has a FIFO memory structure to deal with handing data to the host computer; however, only three memory items are allowed at a time. We need to transfer 22 data streams. We therefore needed to interlace the data on the FPGA and de-interlace it on the host computer.

2.2.5 Force spectroscopy

The force spectroscopy runs in a state machine structure to handle different cases. In this way, it can execute a series of instructions that can change based on the logic. Instructions that can be executed include things like: go down until a force threshold is reached, wait a specified time, go up until either a molecule is attached or the tip is a certain distance from the surface (these three instructions begin almost every program), arm the force clamp or position clamp on the FPGA,

and allow the user to manually adjust the tip height with a joystick video game controller. Using these building blocks, various programs were written to do specific tasks. Pseudocode for these programs is included in Appendix D. In order to run quickly enough, much of the logic for force spectroscopy takes place on the FPGA chip.

2.2.6 Spring constant calibration

The spring constant calibration software runs on a different FPGA vi so that it may acquire data at a higher rate than the AFM operation vi, which runs at 5 kHz. Spring constant calibration data must be acquired significantly above the resonant frequency of the cantilever; typically we filter this data at 60 kHz and acquire at 120 kHz. The spring constant calibration program acquires several short (1s) time records, takes power spectral densities of each, then averages several power spectral densities. To find the spring constant, the peak or roll-off of the power spectrum A as a function of frequency ω is fit to a simple harmonic oscillator [51]:

$$A(\omega) = \frac{A_{dc}\omega_0^2}{\sqrt{(\omega_0^2 - \omega^2)^2 + \frac{\omega_0^2\omega^2}{Q^2}}}, \tag{2.3}$$

where A_dc is the DC amplitude, ω_0 is the peak frequency, and Q is the quality factor. The fit is performed using the built-in LabVIEW vi "Nonlinear Curve Fit.vi", and the spring constant k is calculated using:

$$k = k_B T((\pi/2)\omega_0 A_{dc}^2 s^2)^{-1}, \tag{2.4}$$

where s is the sensitivity of the optical lever arm in nm/V.

Chapter 3

Atomic-scale stability and registration in ambient conditions

This chapter is adapted from Reference [35].

3.1 Image-based demonstration of extreme AFM stability

We used imaging as the most authentic test of long-time-scale stability, so we required a sample that could withstand over an hour of continuous imaging in ambient conditions. Thus, we imaged single 5-nm diameter gold nanospheres, which are known to be robust and incompressible [52]. Specifically, we imaged with a silicon-nitride tip while stabilizing the 3D position of the sample and the lateral position of the tip as described in Chapter 2. The z position of the tip PZT stage was adjusted to maintain a constant tip-sample interaction force ($F \sim 200$ pN), which was determined via the cantilever-deflection-sensing laser. We acquired seven sequential images. Representative images at the beginning, middle and end of the time course are displayed in Figure 3.1, a-c. Line scans through these images showed no significant lateral motion (Figure 3.1, d).

To demonstrate atomic-scale stability and registration, we performed a 2D cross-correlation analysis (Figure 3.2). This analysis precisely tracked the nanosphere's location during 82 minutes of continuous imaging (Figure 3.1, e). The residual lateral drift rates were 4 and 5 pm/min in x and y, representing a 250-fold reduction of the inherent instrumental drift rate, as seen from the drift compensation applied to the instrument during imaging (Figure 3.3). These residual rates, achieved in air at room temperature, are close to those found in cryogenic conditions ($\sim$1 pm/min, 8 K [57]). The precision of this control (and analysis technique) are further verified by small average

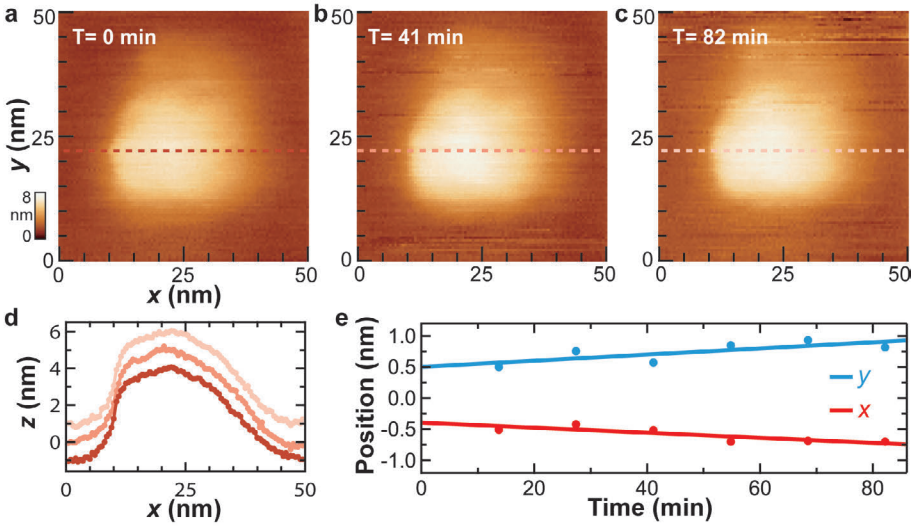

Figure 3.1: Ultra-stable AFM imaging. (a-c) Images of a 5-nm gold nanosphere taken at times T = 0, 41 and 82 minutes, respectively. (d) Line scans through the center of each image. (e) Relative lateral position of the nanosphere plotted versus time as determined by a cross-correlation analysis [x (*red*), y (*blue*)]. From linear fits to the data (*lines*), we deduced residual lateral drift rates of 4 and 5 pm/min in x and y, respectively. Traces in panel d and e offset vertically for clarity. From Reference [35].

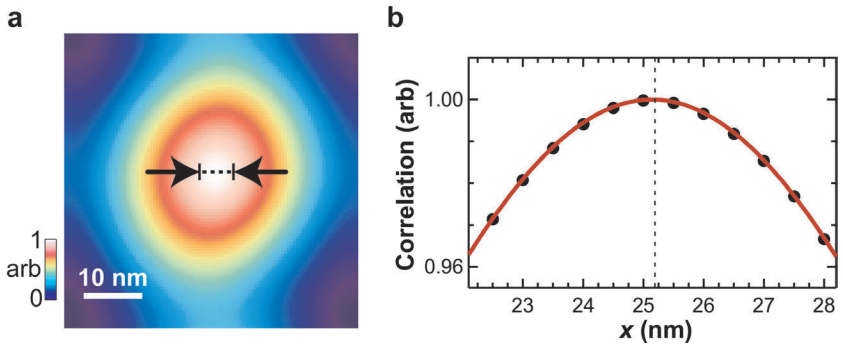

Figure 3.2: To localize the gold nanosphere and deduce the residual drift rate, we calculated 2D cross-correlations [53, 54] between the images shown in Figure 3.1. We used the first image as the kernel to analyze the subsequent six images. (a) The 2D cross-correlation between the first and last images shown in Figure 3.1. Each cross-correlation yielded a Gaussian-like peak. The lateral location of the nanosphere (Figure 3.1, e) was determined by fitting a 2D Gaussian to the central 5-nm region of each cross-correlation peak. (b) A 1D slice (*dots*) through the 2D cross-correlation is plotted with the corresponding Gaussian fit (*red line*). This 1D slice is centered vertically on the 2D cross-correlation peak (black dotted line in a). The nanosphere's location [$x_p = 25.199 \pm 0.004$ nm (peak $\pm\sigma_{fit}$)] is indicated graphically in b (*dashed line, line thickness* $= 5\sigma_{fit}$). We achieved localization precision (σ_{fit}) of <10 pm for all data presented. Thus, the uncertainty in the analysis contributes a small error (<10%) to the reported residual drift (Figure 3.1, e). We note that achieving localization precision on the order of 1/10th of a pixel is routine in correlation analysis of AFM images [27]. From Reference [35].

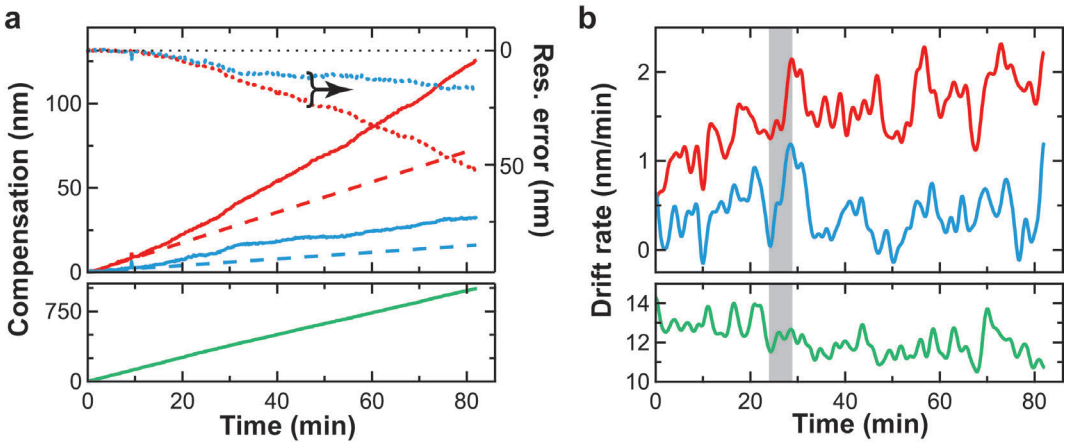

Figure 3.3: (a) Aggregate lateral compensation [x (*solid red*), y (*solid blue*)] applied to tip and sample PZT stages during the imaging period shown in Figure 3.1. Since the imaging signal was deduced from the tip PZT stage, we plot only the vertical compensation to the sample PZT stage (*green*); while this drift (12 nm/min) is substantial, it is consistent with current z-axis stabilization results (11 nm/min[55]). We fit lines (*dashed*) to the first 5 minutes of the data and extended those lines to the end of the data. This is equivalent to assuming a constant drift rate used in linear predictive techniques (e.g., feedforward tracking[24]). By taking the difference between this assumed drift and the measured drift, we deduced the residual error (*dotted*). At two minutes into this extrapolation, the residual error exceeded 1 nm. (b) Lateral and vertical drift rates calculated from the active compensation shown in a. We observed large variations in drift rate ($\sigma_{lateral} = 0.46$ nm/min; $\sigma_{vertical} = 0.80$ nm/min). These variations limit the accuracy of predictive approaches[24, 27]. For example, on the time scale of typical image acquisition [5 minutes (*grey shaded region*)], drift rates varied by more than 1 nm/min on a single axis. While it is common to postpone imaging to let an instrument "settle" [56], drift rate variations in our data persisted. Nonetheless, we achieved atomic-scale stability over long time scales (Fig. 3.1). Thus, our active 3D stabilization method provides a path to robust and routine imaging with atomic-scale stability even in the presence of time-varying drift rates. From Reference [35].

deviations— 23 and 40 pm in x and y, respectively— of the nanosphere's location from the linear fits. While we refer to the time evolution of the correlation-peak position as "residual drift" of the nanosphere's location, this apparent motion could also arise from instability of the nanoparticle relative to the cover slip [44] or from tip-sample degradation. We achieved atomic-scale stability and registration over 10s of minutes. It is this registration and stability, not resolution, that is the unique feature of this instrument.

In this early implementation, we used transparent substrates in air, but we have also achieved proof-of-principle, tip-based BSD signals in several conditions including in liquid and through both birefringent substrates and thin metal films on glass (mica and gold, respectively; see 3.4). In addition, nanometer-scale metallic particles (5-nm gold nanospheres) scanned through the tip-stabilization laser did not degrade the optical signal. Thus, BSD-based tip detection is robust to small optical changes in the local detection volume and, in principle, compatible with several different environments and substrates. However, bulk metal and opaque substrates are not compatible with our current implementation of BSD.

3.2 Improvement in signal-to-noise ratio and image quality by slow scanning

In principle, the signal-to-noise ratio in an image can be increased by scanning slower to average cantilever response. AFM cantilevers are subject to Brownian motion in addition to other noise sources which often couple into cantilever motion (e.g., acoustic, mechanical). Thermal motion, which has a zero mean, can be averaged at the expense of temporal resolution. In general, when studying slowly varying or static samples, it is preferable to average data for a long time with respect to the response time of the cantilever ($\sim$100 μs) as well as the characteristic time of other noise sources, as shown in Figure 3.5. However, in practice, most AFM images are acquired quickly, often to avoid drift. The prospects for increasing the signal-to-noise ratio are predicated on effective averaging of cantilever response. We demonstrated this reduction by acquiring cantilever response at a single stabilized pixel (Figure 3.6, a). We observed a fivefold reduction in the standard deviation of the deflection signal from 0.47 nm to 0.09 nm for data smoothed to 5 kHz and 50 Hz,

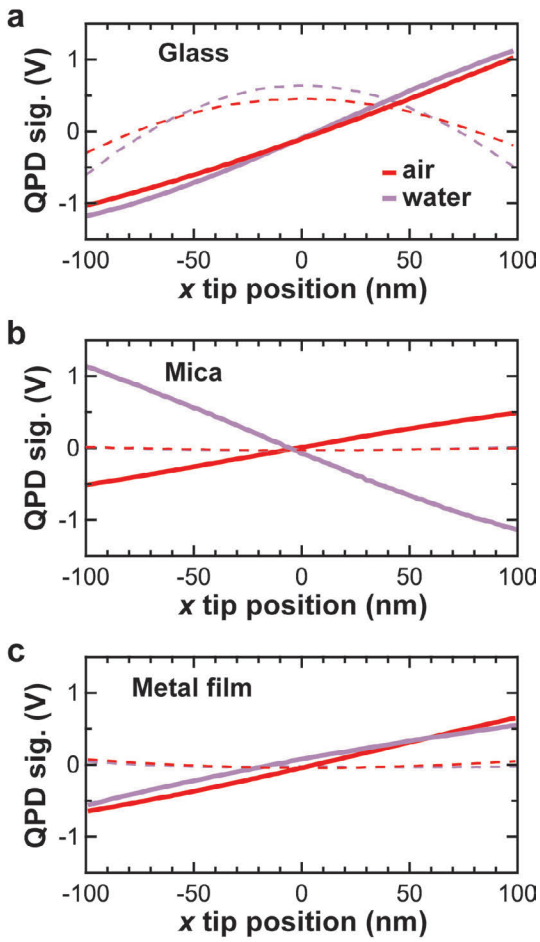

Figure 3.4: (a) Quadrant photodiode (QPD) signals as the tip was scanned along the x-axis through the detection laser. These records were measured through microscope cover glass with the tip in air (red) and submerged in water (*purple*). On-axis signals (solid lines) and lateral crosstalk signals (dashed lines) are displayed. (b-c), Analogous records acquired through muscovite mica (V-1 grade, SPI) and through a thin metal film (2 nm Ti + 6 nm Au) on glass, respectively. We note that a sign change in sensitivity for back-scattered detection (BSD) for changes in optical condition has been previously reported[58, 59]. These proof-of-principle signals suggest that BSD is compatible with birefringent substrates and thin metal films. From Reference [35].

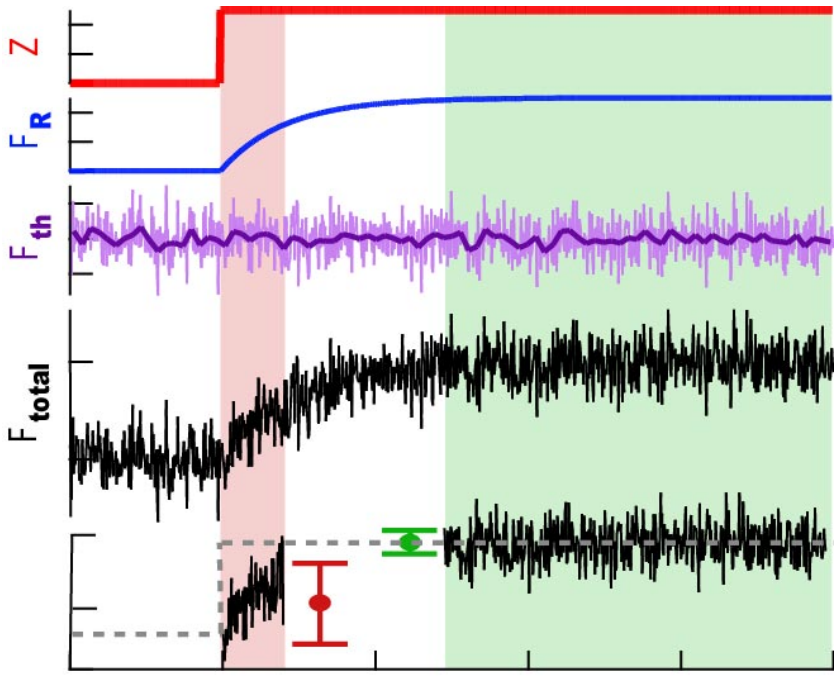

Figure 3.5: Conceptual illustration of advantages of slow scanning. When the cantilever encounters a sharp change in topography Z (*red line*), its response F_R is limited by its natural frequency (*blue*) and is also subject to thermal fluctuations F_{th} (*purple*), so ultimately the response is F_{total} (*black*). If the data are collected quickly (*red shaded region*), the resulting pixel value (*red point*) contains more noise and is an inaccurate measurement of the step height. If, on the other hand, data are collected more slowly (*green shaded region*), the resulting pixel value (*green point*) is less noisy and more accurate.

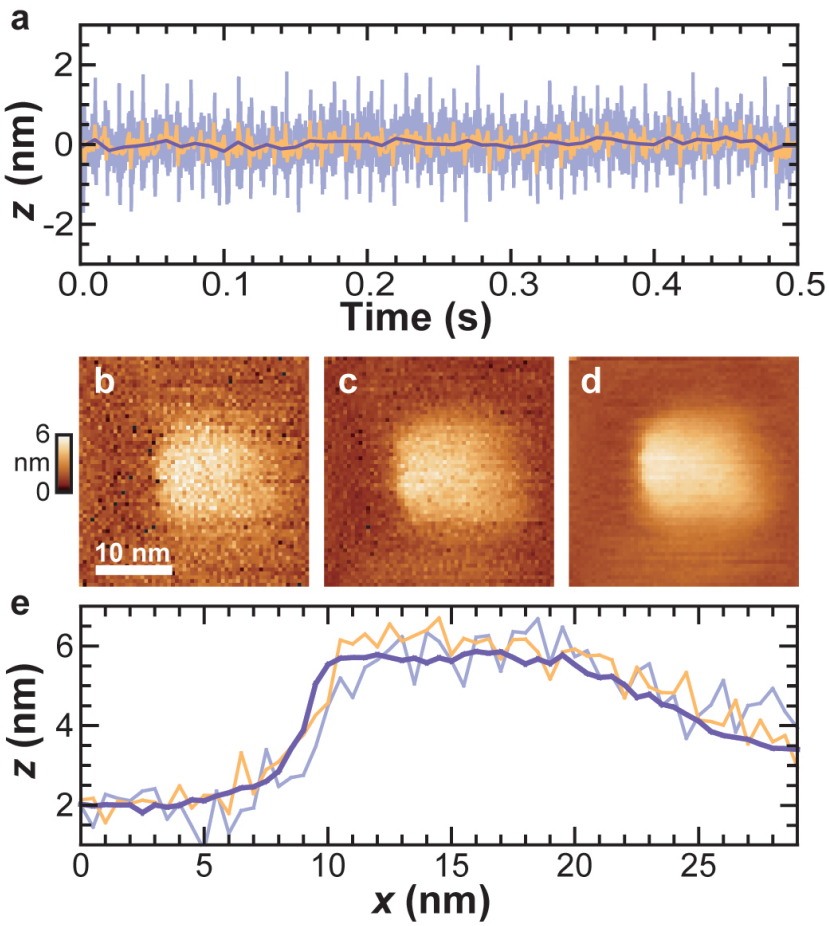

Figure 3.6: Slow scanning to improve image quality. (a) Time record of the cantilever- deflection signal when the tip was engaged on the surface and held stable at a single pixel. Analysis of these records showed standard deviations of 0.47, 0.24 and 0.09 nm when low-pass filtered to 5 kHz (*light purple*), 500 Hz (*orange*) and 50 Hz (*dark purple*), respectively. (b-d), Sequential images of a 5-nm gold nanosphere taken with increased averaging. Specifically, the averaging times per pixel were 0.2, 2 and 20 ms for panels b-d respectively. (e) Line scans through the center region of images [b (*light purple*), c (*orange*) and d (*dark purple*)]. From Reference [35].

respectively (Figure 3.6, a). Ideally, averaging white Gaussian noise over two orders in frequency should result in a tenfold reduction in noise. Thus, we achieved substantial (5×), but not ideal, averaging of the cantilever response. We expect that most of the difference was mechanical loop noise, which has since been greatly reduced (Figure 2.5).

Next, we achieved improved imaging by stabilized slow scanning. Specifically, we acquired three 30 × 30 nm^2 images of the same 5-nm gold nanosphere, increasing the averaging time per pixel (0.2 ms, 2 ms and 20 ms for Figure 3.6, b, c and d, respectively). Improvement in image quality is visually apparent. Quantitatively, line scans through the center of each image (Figure 3.6, e) also revealed a fivefold reduction in the r.m.s. surface roughness over the center of the nanosphere. Thus, the successful reduction in cantilever noise at a single pixel was recapitulated during imaging.

3.3 Methods

The ultrastable instrument is described in detail in Chapter 2.

Gold nanospheres for imaging were attached to the surface with poly-lysine. Specifically, the cover slips were coated with poly-lysine at 0.1% (w/v) for 60 s, rinsed in ultra-pure H_2O and blown dry with nitrogen. Gold nanospheres (5-nm diameter, CV < 15%, BBI) were diluted 1:2 in ultra-pure H2O from stock solution (OD 1), applied to the cover slip, allowed to bind for 5 min., rinsed, blown dry and incubated at 60 ℃ for at least 1 hour. Large-area open-loop AFM imaging showed uniform coverage at 10 nanospheres/μm^2. If the gold nanosphere was outside the calibrated region, we found it in one of two ways: (i) We translated the 845-nm laser (with respect to the tip) using its steering mirror to explore a new region of the surface. Or (ii) we coarsely translated the sample stage to one of many (∼5,000) identical fiducial marks patterned over a 1 ×1 mm^2 region of the sample surface. Imaging with forces <1 nN in contact mode should not compress the nanospheres [52].

Although such 5-nm gold nanospheres are roughly 10^4-fold smaller by volume than the silicon fiducial marks, we attempted to measure their optical signal, since such signals could lead to

erroneous tip positioning. At the gain amplifications used for measuring tip motion, we found no signal. However, larger gold beads (diameter = 15 and 40 nm) produced small perturbations on the AFM tip signal (2 % and 7 %, respectively). In principle, the optical signal of a scattering sample could be recorded prior to imaging and subtracted. Atomic-scale sample stability and registration [45] assure that no significant drift will occur and that such background subtraction will remain valid for long durations.

During imaging, all three axes of the sample and the lateral position of the tip were simultaneously and independently stabilized based on the back-scattered optical signals (see Chapter 2). The z position of the tip was controlled via optical detection of the cantilever-lever deflection. We imaged in contact mode with a tip-sample force of $\sim$200 pN. To improve force precision and adjust for drift which can occur in the cantilever-deflection-sensing opto-mechanics, the force was recalibrated (via an automated routine) at the beginning of each linescan throughout each image. The need to do this was due, at least in part, to the force drift of gold-coated cantilevers. This problem and its solution are described in detail in Chapter 6. At all times during imaging, the tip was held at a fixed lateral position with respect to its BSD detection laser. The sample was simultaneously scanned and stabilized by periodically updating the sample-position set point in the feedback loop. Spacing between pixels was 0.5 nm. We averaged 20 ms of data at each pixel into a single point (unless otherwise stated). Images were processed by subtracting an offset from each line and false colorized with WsXM [60] with the vertical full ranges shown.

Chapter 4

Label-free optical imaging of membrane patches for atomic force microscopy

This chapter is adapted from Reference [41], except for Section 4.3.5, which has previously been described in a US patent application [61].

4.1 Introduction

In biological applications of AFM, the sample is often prepared by allowing molecules of interest to adsorb randomly onto the surface. The user then images over a large area to find a desirable region for detailed study. Unfortunately, this process risks damage to the tip, as shown in Figure 4.1, and the sample. Mechanical wear or adsorption of surface-bound proteins to the tip can degrade the tip's imaging capability. Moreover, alteration of the tip's chemical specificity by unwanted modification hinders chemical force microscopy [62] and coupling of biomolecules to the tip via covalent linkages [15]. Finally, the high scan rates typically used for large-area imaging can damage delicate biological samples due to decreased force control. (As an example, see Figure 4.7, where a horizontal line was accidentally scratched into a purple membrane patch during imaging.) Thus, while AFM-based studies clearly require tip-sample interactions, minimizing or even eliminating tip-sample interactions while locating biological samples for detailed study is desirable.

Small protein structures and even single proteins can be detected using wide field optical microscopy. For instance, video-enhanced differential interference contrast (DIC) microscopy can detect bacterial flagella [63], which are tubular protein assemblies with an outer diameter of 15

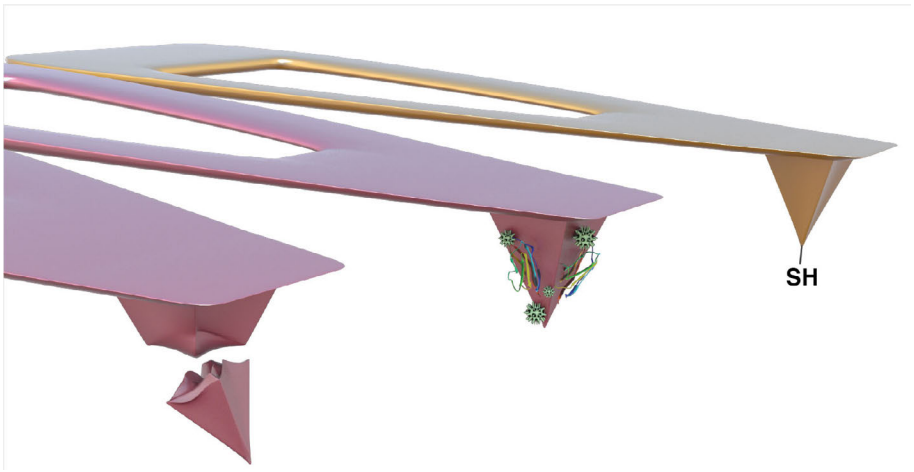

Figure 4.1: The AFM tip can become degraded in multiple ways by scanning. It can break, proteins and other contaminants can adhere to it, and desired chemical surface treatments can become contaminated.

nm. Unfortunately, DIC microscopy is challenging to incorporate with AFM [64]. Fluorescence microscopy, which is quite compatible with AFM, has located single fluorescently labeled proteins with nanometer-scale precision [65]. Researchers have integrated fluorescent imaging into AFM, including AFM tips with an embedded microphotodetector [66] as well as AFMs combined with wide field [67] and total internal reflection [68, 69] excitation.

Notwithstanding these successes, it is desirable to locate biomolecules without the need for fluorescence. Such label-free detection offers many advantages [40], most notably the use of native (or unmodified) proteins. Recently, label-free detection based on scanning the sample through a focused laser, called iSCAT [39], imaged both microtubules and virions (diameter = 45 nm) by detecting the back-scattered light [40]. We previously used back-scattered light [45] to detect and thereby control the position of an AFM tip to achieve an ultrastable AFM [35]. The similarity between the optics used for label-free detection and our stabilized AFM suggested a tip-free means to optically image a sample prior to AFM-based studies.

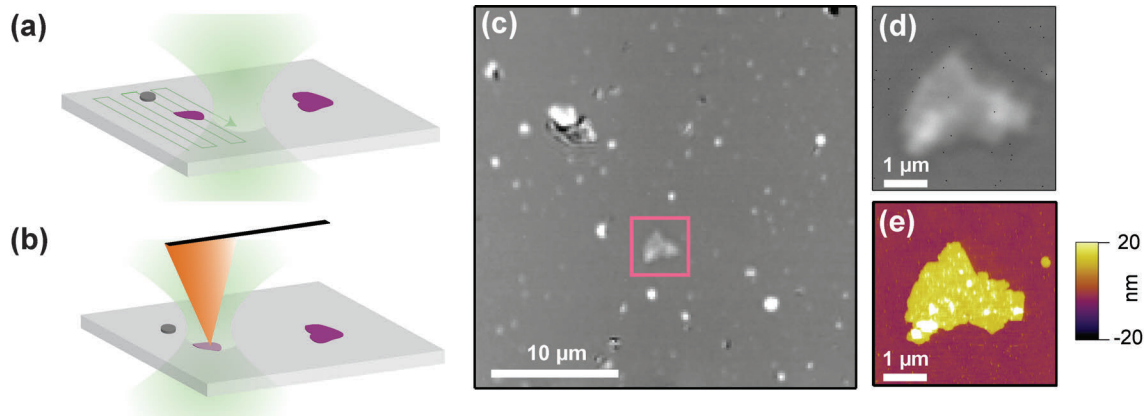

Figure 4.2: Label-free location of a region of interest for study by AFM. (a) With the tip retracted far from the surface, the sample is raster-scanned through the focused laser beam to obtain an image. (b) An AFM tip, aligned to the laser used for imaging, can probe an optically identified feature for detailed study. (c) A representative 30 × 30 μm^2 optical image (pixel size = 150 nm) revealed several surface features. The pink box denotes a purple membrane patch suitable for further study. (d) An optical image of area in the pink box (pixel size = 20 nm). (e) An AFM image of the same area shows it to be a purple membrane patch (pixel size = 4.2 nm). From Reference [41].

In this chapter, we demonstrate the integration of label-free optical imaging of biological samples with AFM. The efficient optical imaging over a large area (30 × 30 μm^2) allowed us to select regions containing purple membrane patches for study with AFM (Figure 4.2). Using the ultrasonic sub-stage, we can also patch these 30 ×30 μm^2 areas together to make a much larger image. Crucially, the optical image was inherently spatially aligned (or registered) to the subsequent AFM images with nanometer-scale precision (∼40 nm). Further, it was sensitive, detecting ∼6-nm tall patches of purple membrane, bacteriorhodopsin (BR) embedded in a lipid bilayer, with a high signal-to-noise ratio (S/N ≈ 20). This registration arises because both imaging modes share a common reference frame; the optical axis of the laser used for optical imaging is also used for aligning the tip. Thus, label-free optical imaging of biological samples prior to AFM investigation provides a means for increased reliability and performance in AFM by locating sparsely distributed biological samples while preserving the sharpness and chemical specificity of tips for high resolution imaging and force spectroscopy applications.

4.2 Materials and methods

4.2.1 Sample preparation

The protocol for adsorption of patches of BR from Halobacterium salinarum (Sigma) was adapted from [70, 71] for use on glass cover slips (Corning). The cover slips were cleaned by etching in 6M ethanolic KOH for 3 min. Silicon posts were added as fiducial marks via physical vapor deposition through a shadow mask as described in Section 2.1.2 and Reference [45]. Previous work from our group has shown that samples can be vertically aligned using a polystyrene bead stuck to the surface [45]. Although substrates with stuck beads are simpler to fabricate, we prefer silicon posts for AFM applications because the posts are uniformly distributed, preserve the surface chemistry, and are more stable. The cover slips were oxygen plasma treated for 4 min (PlasmaStar, Axic). Lyophilized BR was diluted to a stock concentration of ∼250 μg/mL in 0.01% NaN_3. Immediately after the plasma cleaning, we applied 50 μL of adsorption buffer [300 mM KCl, 50

mM MgCl, 10 mM Tris HCl (pH 7.4)] onto the surface, then mixed in 20 μL of stock BR. After ∼30 min incubation, the sample was rinsed with imaging buffer [300 mM KCl, 10 mM Tris HCl (pH 7.4)] and mounted in a liquid cell. We note that light absorption inherent in BR was not the origin of our label-free imaging. BR-containing membrane is referred to as "purple membrane," due to its absorption maximum at 568 nm that extends out to 650 nm [21]. Our imaging light (810 nm) was far detuned from this absorption.

4.2.2 Data collection and analysis

To optically image the sample, it was raster scanned through the focus by alternately moving the stage and collecting data. The back-scattered light was collected onto a QPD (YAG 444-4A, Perkin-Elmer Optoelectronics: sensitivity ≃0.5 A/W at 810 nm) combined with a transimpedance amplifier with a gain of 100 kΩ. This signal was sent to custom low-noise electronics, designed and built in-house, that incorporated an offset amplifier. This offset amplification better matched the varying portion of the sum signal to the 20 V input range of the FPGA card used for data acquisition. For all data shown here, the gain was 100. We note that the gain could be increased significantly for label-free imaging, but was limited in this instrument to accommodate application to AFM stabilization [35]. Finally, we low-pass filtered the data at 2.4 kHz using a programmable multipole filter (Frequency Devices) and digitized at 5 kHz with a bit resolution of 0.3 mV. Each pixel in the optical images represents an average of 10 data points for a total observation period of 2 ms. During this process, the tip was retracted from the surface by ∼2 mm, unless otherwise noted. AFM images were acquired in constant-force contact mode at ∼200 pN, using silicon nitride tips (OMCL TR-400, Oympus, $k_{cantilever} \approx 80$ pN/nm). The measured height of the purple membrane patches was ∼8 nm. This value is consistent with prior reports of the height of purple membrane measured by AFM, which has been shown to range from 5-10 nm depending on ionic conditions and the substrate [72]. AFM images were flattened using software from Asylum Research.

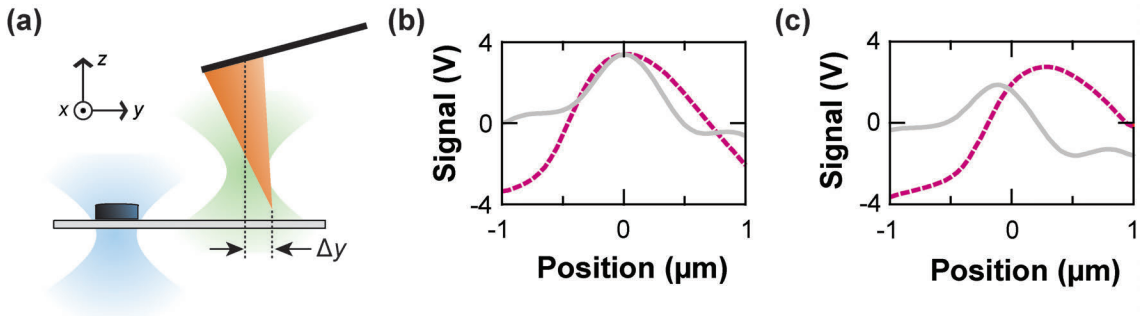

Figure 4.3: Alignment of the tip to the optical axis of the laser (*green*) used for label-free imaging. (a) For increased precision, we aligned the position of the surface with respect to the laser foci by scattering a second laser beam (*blue*) off a silicon post. (b) The QPD sum signal as a function of tip position in x (*grey solid line*) and y (*purple dashed line*) aligned to maximize the sum signal. (c) The final alignment of the QPD sum signal as a function of lateral position after positioning to compensate for the fixed offset between the optical and the AFM image. From Reference [41]

4.2.3 Alignment

As a first step, we sequentially aligned the sample and then the tip to the pair of laser foci using the sample surface as the vertical reference ($z = 0$) (Figure 4.3). Specifically, we scanned the silicon fiducial mark through the sample detection laser focus using the sample PZT stage and observed the position at which the signal was maximized. We then set the position of the sample to a predetermined offset from this maximum [45] ($\Delta z = 1.5$ μm for all data shown in this chapter). Next, the vertical position of the tip was determined by touching the tip to the surface using the AFM PZT stage and then retracting it 60 nm. This protocol also yielded the sensitivity (V/nm) for the optical lever arm. We note that the laser foci are vertically offset by 2 μm to simultaneously maximize the scattering from the tip and the sample for application to ultrastable AFM [35]. If desired, a similar vertical alignment can be accomplished with a single laser.

Next, we laterally aligned the tip to the optical axis of the tip-detection laser (Figure 4.3, a, *green*). To do so, we sequentially scanned the tip along each lateral axis (Figure 4.3, b) and set the tip position to maximize the sum voltage along each line scan. We note that the precision of this alignment procedure ($\sim$10 nm) greatly exceeds the diffraction limit ($\sim$200 nm). We determined an offset (e.g., Δy) between this empirically derived tip optical center and the tip's actual point of contact with the surface by comparing the position of the patch center using a two dimensional cross-correlation analysis (see Section 3.3). This offset was repeatable and remained constant for different tips of the same type, but varied between different types of tips. We measured an offset of 100 nm in x and 300 nm in y with an Olympus TR400 tip tilted at 15° to the surface and aligned to a beam whose focus was approximately 500 nm above the surface. Finally, we incorporated this offset into the alignment procedure by positioning the tip away from the maximum of the optical signal (Figure 4.3, c).

4.3 Results

AFM studies of sparsely distributed biological structures would be accelerated by a tip-free, label-free means to find regions of interest. We first show that ∼8-nm tall membrane patches were near the detection limit of optical imaging via back-scattered light, but offset amplification of the optical signal led to a 60-fold increase in the S/N (Section 3.1). The quality of the image was also enhanced (though to a lesser degree) by the presence of the AFM tip near the surface (∼3 μm), but such images were altered along the cantilever's long axis (Section 3.2). Next, we show that these optical images could be registered to subsequent AFM images with nanometer-scale precision (Section 3.3). Finally, the lateral signals from the QPD rather than the sum signal can be used to highlight edges (Section 3.4).

4.3.1 Visualizing membrane patches with improved S/N

Nanometer-scale biological structures lead to small optical signals. The inherent back-scattered signal from ∼8-nm tall patches of purple membrane with the tip far from the surface (shown schematically in Figure 4.4, a) yielded images with sufficiently low S/N that membrane patches were difficult to resolve (Figure 4.4, b). We quantified the signal by computing the normalized contrast $(I_{patch} - I_{glass})/I_{glass}$ between the on-patch signal (I_{patch}) and the off-patch signal (I_{glass}) [39]. The contrast from the membrane patches was 30-fold smaller than prior results on virions (45-nm dia.) [40]. The proposed contrast mechanism is an interference between back-scattered waves. Within this model, the expected normalized contrast for BR was estimated using a simple plane-wave model [73] with the appropriate index of refraction [74] and crystallographic height [75]. This estimate of 0.07% was consistent with the measured normalized signal of 0.06%. Thus, the low contrast was an inherent physical feature of the system and could not be increased for better image quality. Therefore, we sought to improve S/N by decreasing noise. We note that the measured contrast is not inherently normalized: rather, the measured signal is a small modulation on top of a comparatively large signal, which is proportional to laser intensity (I). Hence, uncorrected fluc-

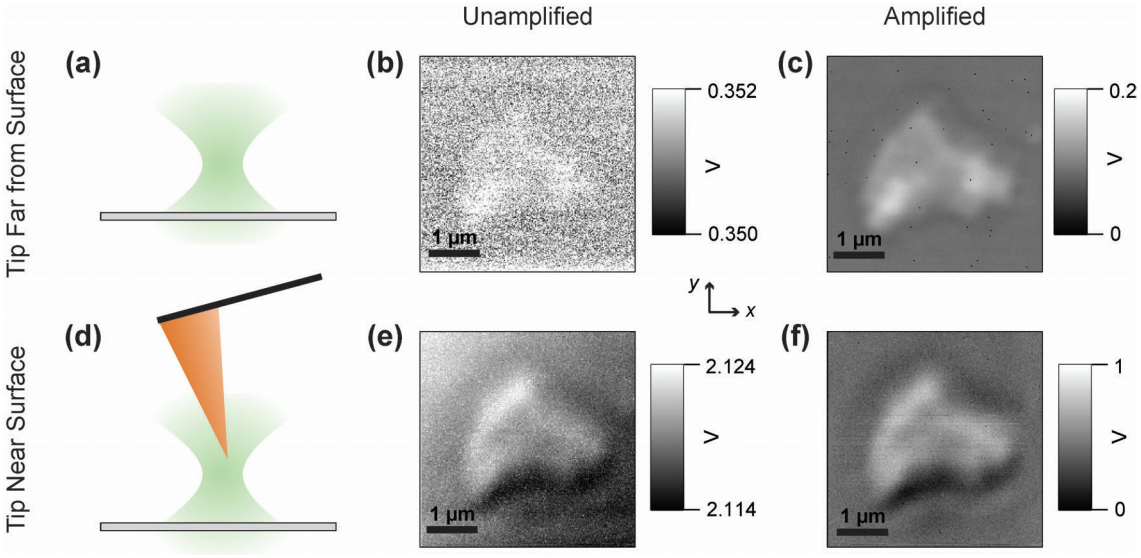

Figure 4.4: Effects on the image of offset amplification and tip presence near the surface. When the tip was far (∼2 mm) from the surface (a-c), the signal before amplification (b) was nearly lost in the noise, but the amplified image has S/N ∼ 20. Interestingly, with the tip near the surface (∼3 μm, d-e), the membrane patch was clearly resolved even before amplification (e), though amplification still improved image quality (f). Both of these images show an asymmetric contrast along the y-axis— the long axis of the cantilever. Pixel spacing is 20 nm in all images. Amplified images were re-zeroed in post processing. From Reference [41].

tuations in I lead to noise in the image. But, in the images shown, the laser was actively stabilized ($\delta I/I < 0.002\%$; $\Delta f = 0.02 - 100$ Hz). Thus, fluctuations in I were not the origin of the low S/N. On the other hand, the absolute change in the inherent signal was only 0.2 mV, smaller than the voltage change associated with a single bit [0.3 mV (20 V/2^{16})]. Thus, our image suffered from digitization noise. One solution would be to increase laser power, as has been done previously [39]. However, we sought a different solution for our AFM-based application, since even relatively small laser powers can lead to substantial deflection of the cantilever. Hence to minimize the perturbation to the tip and cantilever, we used a minimal laser power ($\sim$400 μW). An analogous problem exists in measuring the vertical motion of optically trapped beads with a detector laser sufficiently weak that it does not also act as a trap. In trapping, vertical bead motion also corresponds to the QPD sum signal and has traditionally been limited to nanometer-sized measurements. Previous work from our lab has showed that the combination of intensity stabilization in conjunction with offset amplification allowed for significantly enhanced vertical sensitivity in comparison to intensity stabilization alone [44]. Using this same combination of techniques, single patches of purple membrane were well resolved (Figure 4.4, c). Quantitatively, the 100-fold gain used in the offset amplification led to a 60-fold increase in the S/N. From this improved image, we determined the lateral resolution of the optical images. Specifically, the rise in signal from the off-patch to on-patch region (10% to 90% of the signal) occurred over $\sim$200 nm, consistent with previous reports [39]. In this image, we also notice a faint line of unknown origin around the patch boundary.

4.3.2 Enhanced optical image due to nearby AFM tip

The presence of an AFM tip retracted $\sim$3 μm from the surface (shown schematically in Figure 4.4, d) enhanced the image formed from the unamplified signal (Figure 4.4, e). Given this micron-scale tip-sample separation, we note that this enhanced contrast is not consistent with a near-field effect. The presence of the tip also altered the nature of the contrast along the long axis of the cantilever, producing an asymmetric edge effect qualitatively similar to DIC images. Offset amplification further enhanced this image (Figure 4.4, f). Note that there is a 5-fold increase in

the voltage range between Figures 4.4, b and 4.4, e, and between Figures 4.4, c and 4.4, f. While further work is needed to understand the origin of this enhanced contrast, optical imaging with the tip in the vicinity of the surface could be valuable for three reasons. First, this enhanced contrast obviates the need for offset amplification for imaging membrane patches. Second, coarse motion of the tip (outside the 5-μm range of the PZT stage) is not required between acquisition of the optical and AFM image. Finally, tip-enhanced contrast suggests a means to image even smaller label-free biological structures via back-scattered, far-field optical imaging.

4.3.3 AFM image inherently spatially registered to optical image

These label-free optical images were inherently registered to AFM images, because the tip was aligned with the optical axis of the imaging beam. Initially, there was a lateral offset between the optical image (Figure 4.5, a) and the AFM image (Figure 4.5, b). This offset was due to the difference between the optical center of the tip and the tip's point of contact with the sample. As discussed above, the optical center of the tip was determined through a routine that maximized the signal from the back-scattered light (Figure 4.4, b). We note that such scattering most likely occurred from the body of the tip near the focus rather than the true apex of the tip. Indeed, measurements showed that the geometry of the tip and the vertical height above the surface affected this offset. We would also expect it to be dependent on the tilt of the cantilever. By cross-correlating these two images (Figure 4.5, c), we measured an offset of 100 nm in x and 300 nm in y (Figure 4.4, c). Once this offset was determined, it was eliminated in future image acquisition by compensating the alignment of the tip relative to the optical axis, as shown in Figure 4.4, c.

The geometric origin of this offset suggests that it should be constant over time. To test this idea, we acquired a new set of optical and AFM images (Figure 4.5, d-e). The cross-correlation analysis (Figure 4.5, f) revealed a nanoscale alignment between the two images (40 nm in x; 30 nm in y). Note that the second set of images was acquired with a different tip on a different sample two weeks after the lateral offset was originally determined. Thus, the nanoscale registration and alignment between the label-free image and the subsequent AFM was robust and repeatable.

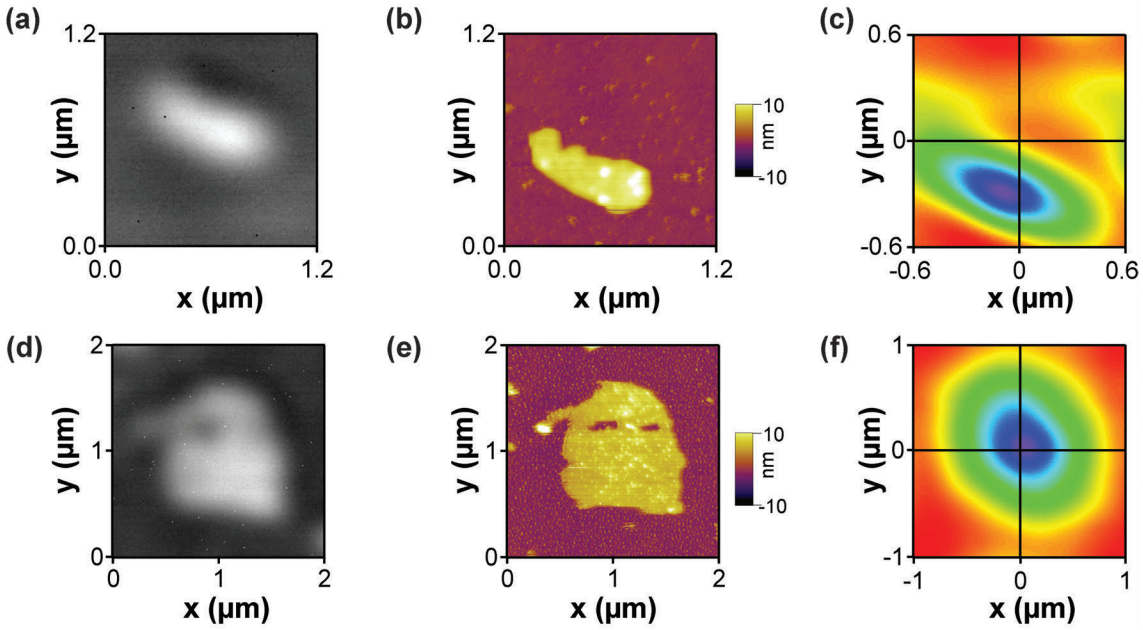

Figure 4.5: Spatial registration between optical and AFM images. When the tip is positioned at its optical center, an optical image (a) and AFM image (b) of the same region show the same feature, but with an offset. (c) Cross-correlation analysis was used to quantify this offset to be 100 nm in x and 300 nm in y. After centering the tip to account for this effect, an AFM image (d) and an optical image (e) of the same area. Cross-correlation analysis (f) showed nanoscale alignment of the two images (40 nm in x and 30 nm in y). Pixel size was 4 nm and 10 nm in the AFM and optical images, respectively. From Reference [41].

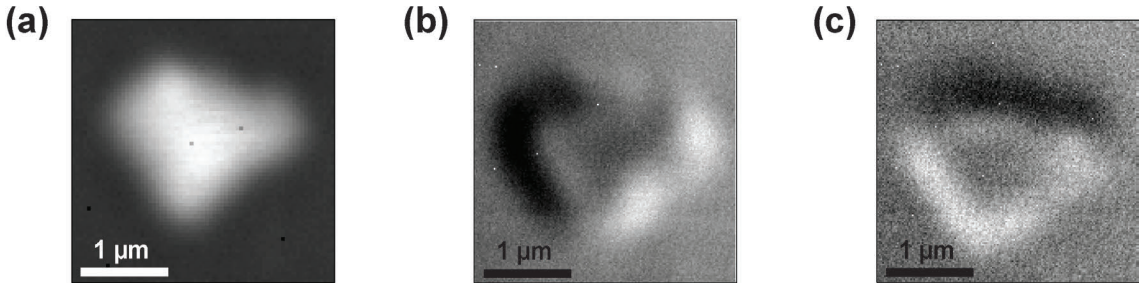

Figure 4.6: Edges highlighted on the x and y channels of the QPD. (a) The sum signal. (b) The signal from the x channel highlights the left and right edges of the feature. (c) Similarly, the signal from the y channel highlights the top and bottom edges of the feature. From Reference [41].

4.3.4 Enhanced edge signals using the lateral signals from the QPD

For completeness, we note that a QPD provides for lateral signals (e.g. the difference between the left and right halves) in addition to the sum of all light falling on the detector (Figure 4.6, a). The images from these lateral signals enhanced the edges of features (Figure 4.6, (b-c)), again reminiscent of images taken with DIC. Future work may be able integrate these lateral signals with the sum signal to allow for better feature extraction or detection of smaller objects.

4.3.5 Registered tip return and exchange

Returning the same tip or a different tip to the same region of a sample is a task that would be very helpful to do with an AFM, but was not previously possible. This would enable the user to return to the same feature after a long incubation, replace a broken or contaminated tip with a fresh one, or change to a different type of tip to perform a different task. Since our tip position is registered to the laser-based reference frame, we can return to the same feature after retracting the tip or changing tips with a high degree of precision, as seen in Figure 4.7. Here, the same purple membrane patch was imaged over several hours with two different tips. The utility of this approach can best be seen by comparing panels (e) and (f). In panel (e), the tip has become contaminated and the image quality degraded. After removing the tip from fluid, wetting with buffer, and returning to the surface, the image quality recovered (f). The dewetting process removes loosely-adhered contaminants from the tip through the meniscus force. In principle, by taking advantage of the array of fiducial marks on the surface, we could separately and repeatedly address many different features in a sample over an extended period of time.

4.4 Conclusion

By enhancing a new label-free imaging technique [40, 39], we successfully produced images of biological assemblies that had an inherent contrast 1/30th of those imaged in prior work [40]. In spite of this low inherent contrast from individual membrane patches, the resulting images had

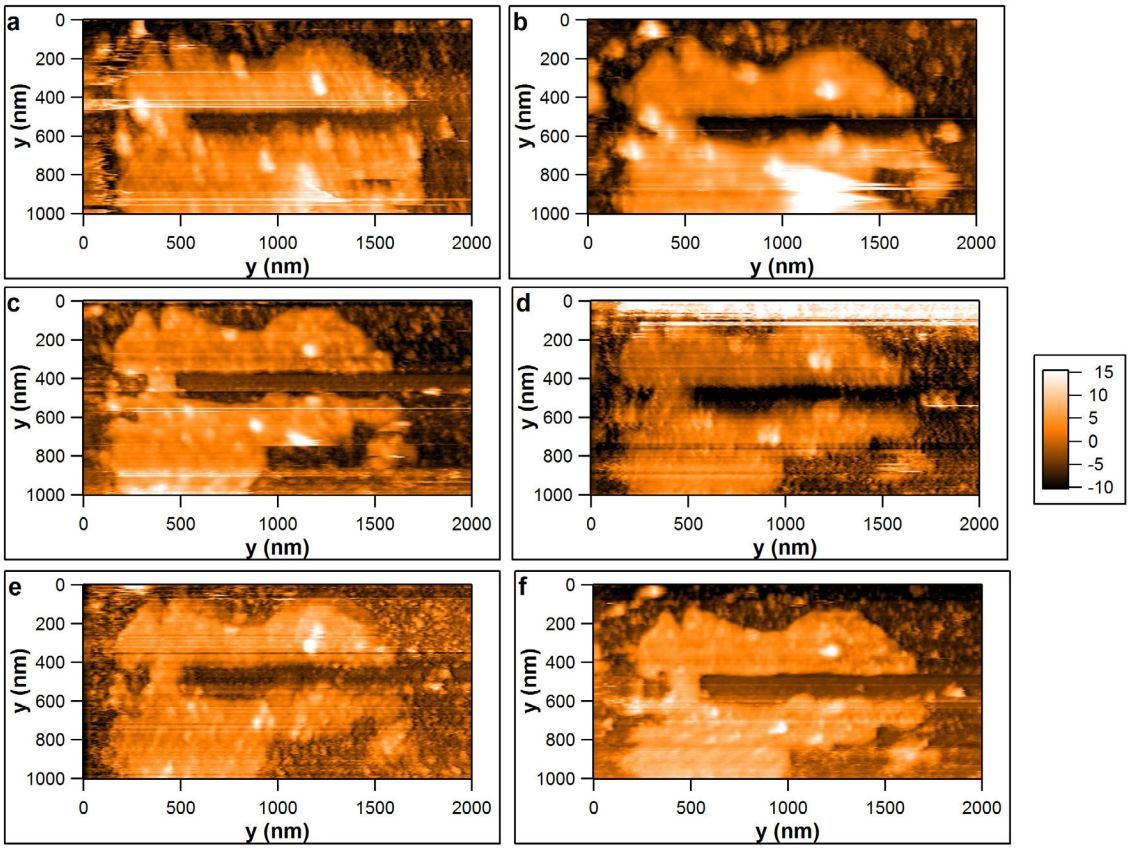

Figure 4.7: Registered tip return and exchange demonstrated with a series of images of the same purple membrane patch. (a) The first image of the patch. (b) A second image with the same tip, after retracting it fully out of the fluid, rinsing the sample with fresh buffer, and re-wetting, taken about three hours later. (c) A third image with a new tip taken about two hours later shows return to the same feature. (d) and (e) Two subsequent images. During these images the tip became contaminated and image quality degraded. (f) A final image taken about twenty minutes after (e), after dewetting the tip, rinsing the sample with fresh buffer, and rewetting the sample. This process cleared the contamination from the tip, and the image quality was restored.

an excellent S/N of 20. Given the high S/N in these images, we expect label-free imaging to be successful for protein assemblies that are smaller or have a lower inherent contrast. We further showed enhanced contrast when the tip was near the surface, a fact that could be exploited to image even smaller objects. Further exploration of the physical origin of this effect could lead to interesting findings and improvements in this label-free optical imaging. From a practical perspective, the simplicity and non-destructive nature of optical imaging enables us to assess the cleanliness and overall quality of samples over very large areas. The registration of the tip to the optical beam also allows for registered tip return and exchange. The registration and alignment of the optical image with the AFM image allows us to optically locate the sparsely distributed patches without unwanted degradation to the tip or the sample. This nanometer-scale alignment arose from the static offset between the tip's optical center and its point of contact with the surface. Importantly, this offset was constant, allowing a single offset value to be used for multiple tips of the same type over several weeks. Locating regions of interest by optical scanning can increase throughput of data collection, often a limiting factor in single-molecule studies. For force spectroscopy and other manipulation processes, it bypasses the need to image with the tip, opening up new possibilities for high-strength covalent attachment between the tip and the sample under study. For instance, the tip can be deterministically brought down onto either a clean region of the surface or a membrane patch without prior AFM imaging. Thus, we expect the combination of label-free optical imaging with AFM to be a valuable addition to biological AFM.

Chapter 5

Independent measurements of force and position in atomic force microscopy

This chapter is adapted from Reference [42], except for Section 5.5.

5.1 Introduction

In a typical force spectroscopy experiment, an AFM tip is coupled to a surface-adsorbed protein by pressing the tip into it. Force-extension curves are then generated by retracting the tip at a constant velocity using a piezoelectric (PZT) stage. Force is measured by cantilever deflection. Extension, or more precisely tip-sample separation, is deduced from the PZT stage position used to control the vertical tip position. Thus, this deduced extension is sensitive to mechanical drift of the AFM assembly ($\sim$10 nm/min) [55]. In order to minimize the effect of drift, experiments are often performed quickly ($\leq$1 s). Even state-of-the-art force clamp experiments, which observe the dynamics of molecules over long time scales (>50 s), are sensitive to this drift [18]; they stabilize cantilever deflection (force) with no independent gauge of the conjugate variable, tip-sample separation. Thus, there is a clear need for an independent measurement of the tip position. Such a measurement would enable the dynamics of protein unfolding and refolding to be studied over arbitrarily long periods, increasing both precision and the range of proteins whose properties can be studied by force spectroscopy. Long-term vertical control of tip-sample separation could also increase the reliability of tip-based nanomanufacturing techniques such as dip-pen lithography [8].

A number of techniques have been put forth to control the vertical tip-sample spacing, with

varying degrees of success and usability. Cantilevers with fluorescent beads conjugated to the apex of the tip enabled measurements of vertical position to 0.4 nm using an evanescent wave [76]. For broad applicability, however, one would like a technique compatible with commercial tips. A differential z-measurement using commercial AFM chips containing two cantilevers achieved 15-nm stability over 3 hrs, but with 5–10 nm short-term vertical noise, which is too high for precision force spectroscopy [55]. In this work, we demonstrate that this pair of focused lasers provides an excellent ($\sigma_z = 0.3$ nm) surface-referenced determination of the tip-sample separation in biologically relevant conditions (in liquid). This new positional measurement is independent of, and complementary to, cantilever deflection (force) and insensitive to mechanical drift of the AFM assembly [45].

5.2 Linearization by 3D calibration

There is some optical crosstalk between the detection axes that leads to an erroneous signal on one axis when moving another. We often observed substantial crosstalk ($\sim$20%) when calibrating the AFM tip, because it is a geometrically asymmetric object tilted at 15° with respect to the y-axis (the cantilever's long axis). Field-programmable gate array (FPGA) cards (PCI-7833R and PCI-7831R, National Instruments) were used to provide the computational power to parameterize and minimize such crosstalk via linear-algebra-based algorithms [47, 38]. FPGAs also provided for more rapid (500 Hz) and therefore precise controlling of all six axes of motion, leading to tip control of $<$0.04 nm in 3D in air.

Future high-precision force-spectroscopy applications demand long-term positional control of the tip while it is disengaged from the surface. Toward that end, we first show how we calibrate the detection laser scattering off the apex of the tip. We then show that this new detection technique provides a measurement of tip position complementary to cantilever deflection. Finally, we show that determinations of the surface ($z = 0$) by the two techniques concur.

For accurate and precise tracking of the AFM tip in 3D, we had to calibrate the substantial optical crosstalk between the nominally orthogonal detection axes. This process is described in detail in 2.2.1 and 2.2.2. In this calibration, the tip was raster scanned in 3D through its detector

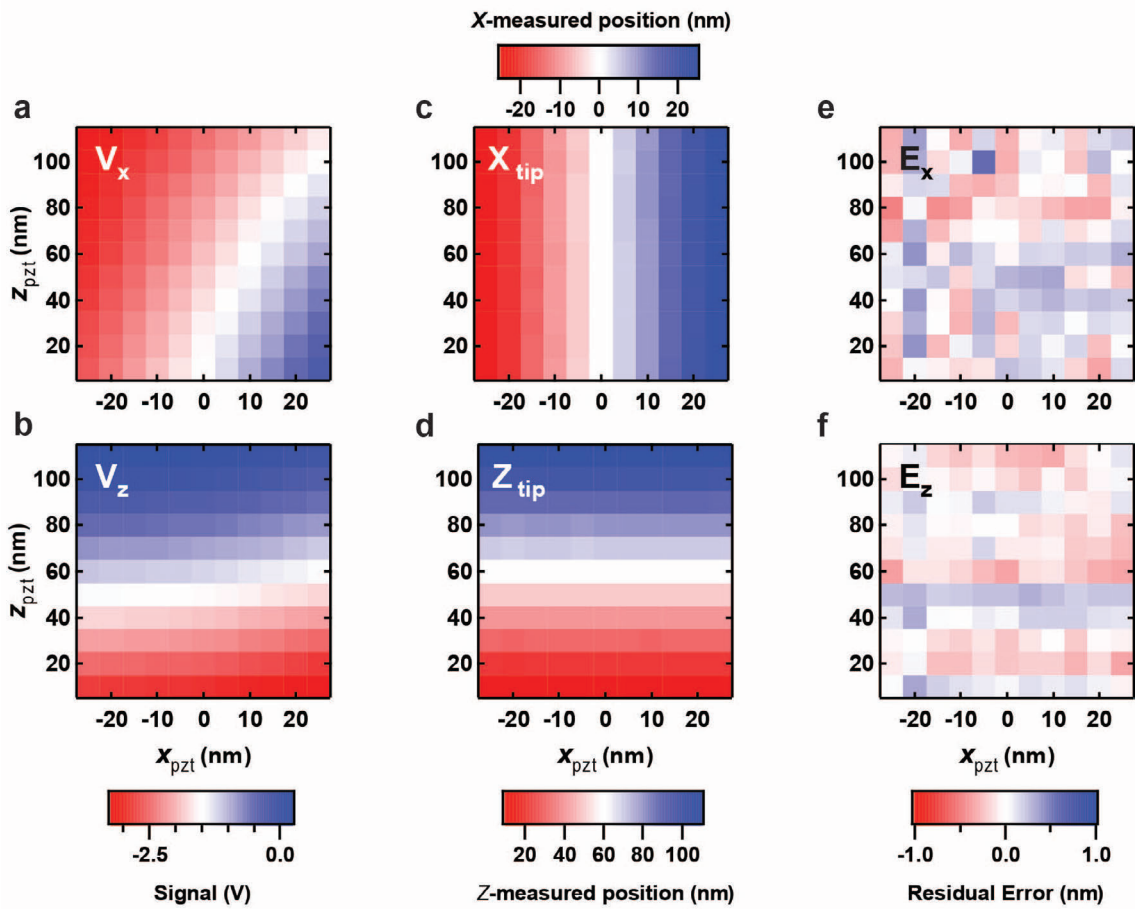

Figure 5.1: 3D calibration of the AFM tip. (a,b) Plots of the QPD voltages (V_x,V_z) as the tip was scanned in the x-z plane. (c,d) As a self-consistency check, tip positions (x_{tip}, z_{tip}) were calculated from the calibration set using the 4th-order crosstalk-compensation routine. (e,f) Residual errors (e.g., $E_x = x_{tip} - x_{pzt}$) are plotted. Plots are in the x-z plane at $y = 0$.

beam using a closed-loop PZT stage. The resulting back-scattered signals (V_x,V_y, V_z) corresponding to stage movements (x_{PZT}, y_{PZT}, z_{PZT}) (Fig. 4a,b) could be scaled using a parameterization of the form

$$x(V_x, V_y, V_z) = \sum_{i=0}^{i+j+k=4} a_{ijk} V_x^i V_y^j V_z^k \tag{5.1}$$

for each axis x, y and z. Next, the coefficients (a_{ijk}) were determined by a nonlinear least-square fitting routine to the 3D calibration set. This complex parameterization — 35 coefficients per axis for a fourth-order fit— should yield orthogonal detection of position along the coordinate axes (defined by the PZT stage). A simple check of this orthogonalization was performed by plotting the requested stage position versus the measured tip position (e.g., x_{tip}, y_{tip}, z_{tip}). The 2D slices shown in Figure 5.1, c,d demonstrate successful linearization. The error in this calibration was quantified by calculating the residual errors (Figure 5.1, e,f), revealing no systematic error in z_{tip} [<0.5% over the vertical calibration range (100 nm)]. Overall, this 3D calibration led to a linear and orthogonal detection of the tip, an asymmetric object. The robustness of this linearization technique successfully compensated for substantial optical crosstalk. On the other hand, the technique is sensitive to mechanical drift during this calibration process (t_{cal} = 20 s), so short-term mechanical rigidity (∼10 nm/min) of the instrument is important.

5.3 Independent position and force measurements

Our new measurement of tip position should be independent of the standard measurement of cantilever deflection, since it is not based on the force applied across the cantilever but rather on the position of the tip relative to its stationary detection laser. To test for this independence, we generated a set of curves in which a tip, initially engaged with a clean glass surface, was retracted by moving the tip assembly via a PZT stage (z_{pzt}) at 20 nm/s. Data were recorded at 5 kHz using a 2 kHz antialiasing filter. The resulting tip position (z_{tip}) and cantilever deflection (z_{lever}) were determined from prior calibrations, as outlined above for z_{tip} and by standard methods for

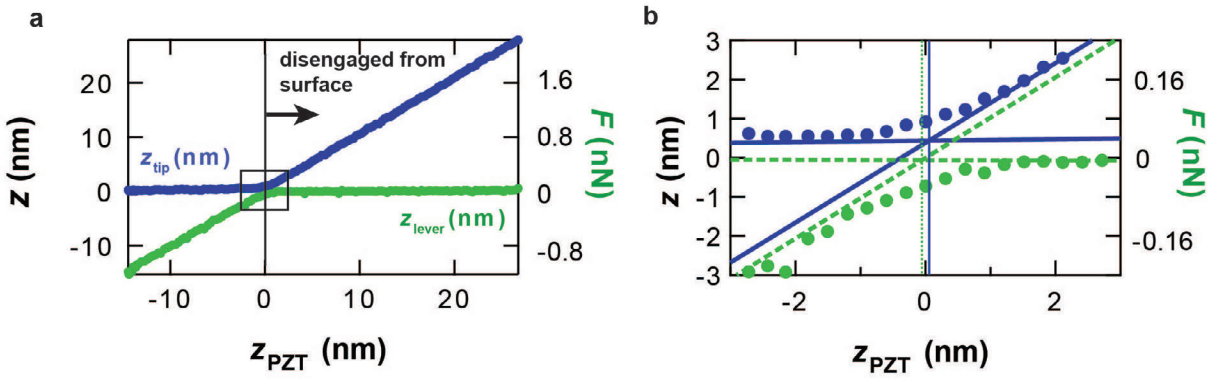

Figure 5.2: Independent measurement of position and force applied to an AFM tip. When the tip is touching the surface, measurement of tip position yields no displacement ($z_{tip} = 0$) but cantilever deflection yields a substantial force (z_{lever}, $F < 0$). As the tip disengages from the surface, F goes to zero but z_{tip} linearly increases. Force was computed from z_{lever} and the nominal cantilever stiffness ($k = 0.08$ N/m). Surface determination by position [z_{tip} (*blue*)] and cantilever deflection [z_{lever} (*green*)] measurements agree. The surface ($z = 0$) was defined as the intersection between first-order fits to the separate linear regions.

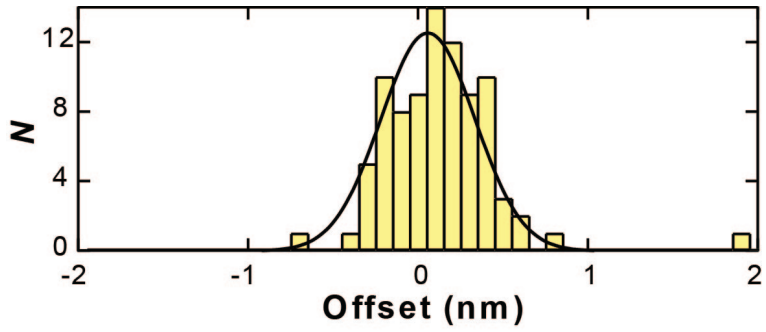

Figure 5.3: A histogram of the difference in surface location between the two measurement methods is shown (N = 86). The distribution is centered at 0.01 nm with a standard deviation of 0.3 nm.

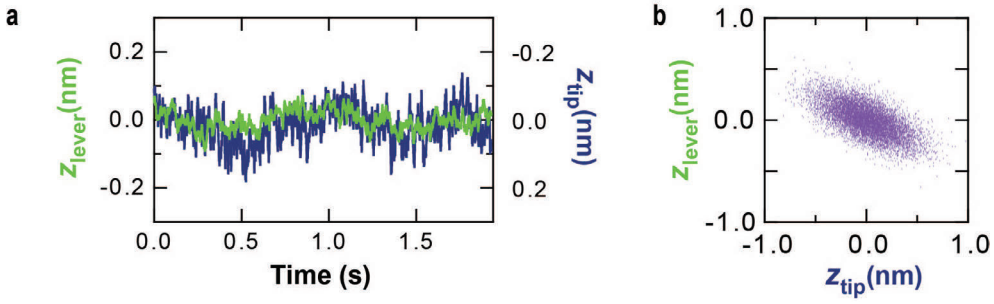

Figure 5.4: Force and position measurements of random tip fluctuations are correlated. (a) Time trace showing deflection measured by the optical lever laser (z_{lever}, *green*) and vertical position measured by the focused laser beam from below (z_{tip}, *blue*). (b) Scatter plot of the two traces in (a) plotted against each other shows good, but not perfect, correlation.

z_{lever}. As shown in Figure 5.2, z_{tip} (*blue*) and z_{lever} (*green*) were indeed independent. When the tip had a substantial load, z_{lever} showed deflection but z_{tip} showed no motion, as expected for an incompressible surface. The converse was also true. When the tip was above the surface, z_{lever} went to zero but z_{tip} increased linearly. More quantitatively, if the calibrations were accurate, linear fits to the two regions of z_{lever} and z_{tip} should yield slopes of either 0 or 1. When the tip was engaged with the surface (z < 0), z_{lever} had a slope of 1.03 ± 0.01 (fit $\pm\sigma_{fit}$), while z_{tip} had a slope of 0.019 ± 0.003. Conversely, when the tip was above the surface (z > 0), z_{lever} had a slope of -0.003 ± 0.002 while z_tip had a slope of 1.021 ± 0.005. Summarizing, measurements of z_{tip} and z_{lever} are independent, providing for simultaneous measurement of the conjugate variables (position and force).

In force spectroscopy, changes in the internal state of the molecule should lead to changes in both extension and applied load on the cantilever. Such correlations between force and extension are a hallmark of a real signal as opposed to instrumental noise. Current experiments do not have access to independent measure of extension and force as our apparatus does. To test for this correlation in the absence of externally applied load, we observed the Brownian forces exerted by the liquid on the tip. As shown in Figure 5.4, the force and extension measured by z_{lever} and z_{tip} were correlated. However, the correlation is not perfect. Measurements of z_{tip} are noisier in part due to less optical power on the QPD and, we speculate, to noise in the tip detection laser. Nonetheless, this correlation highlights the precision of the apparatus, since the magnitude of the resolved motion is small (0.1 nm).

5.4 Determination of sample zero point

Determination of the point where the tip begins to engage the surface ($z = 0$) can be difficult in AFM experiments. Moreover, it is desirable to know the absolute height of the tip over the surface. Traditionally, two lines are fit to the linear regions of a standard AFM calibration curve (Figure 5.2, *green*). The intersection of these lines defines the zero point. However, there is no independent measurement of how accurate this determination is. Direct detection of tip position

(z_{tip}) provides a means for such verification. Inspection of Figure 5.2 shows excellent correspondence between surface determination via z_{tip} and z_{lever}. Line fits to the separate linear regions of z_{tip} and z_{lever} yielded a difference of 0.11 nm (Figure 5.2, b). To quantify this agreement, we repeated this analysis on 86 records. The average difference was essentially zero: 0.01 $\pm$ 0.03 nm (mean $\pm$ std. err.) (Figure 5.3). Since surface determination is usually done once, a better metric for the uncertainty in the absolute height is the standard deviation of the data, which was also quite small (0.3 nm). This verification of surface location provides an accurate zero for measurement of tip height over the surface. Such a surface-referenced measure of z_{tip} will lead to increased confidence in assigning changes in force-extension curves to the structure of the protein or other polymer under study.

5.5 Slow locked pulling and extension clamping

Independent force and position measurements during force spectroscopy applications enables high-precision, slow pulling. Typical pulling rates for AFM force spectroscopy range from 10 nm/s to 10 μm/s; in exceptional cases [22], speeds as low as 1 nm/s are used. The duration of the experiment must be shorter than the time it takes the instrument to drift significantly. However, with a surface-referenced tip height, the pulling speed can be arbitrarily slow (Figure 5.5). This can allow observation of dynamics and intermediates that may be missed with a faster pulling speed, and a greater range of speeds for dynamic force spectroscopy analysis [17]. The slowest possible pulling is, of course, to stop altogether. As will be discussed in Chapters 7 and 8, this "extension clamping" allows the dynamics of folding and unfolding to be observed over long periods of time.

5.6 Conclusion

The traditional observable in AFM is cantilever deflection, which measures the net force applied to the cantilever. In force spectroscopy, a molecule's response to force is measured as a function of extension [14, 15] However, this extension is inferred and is thus sensitive to the mechanical drift of the tip-sample separation. In this chapter, we demonstrated a new method based

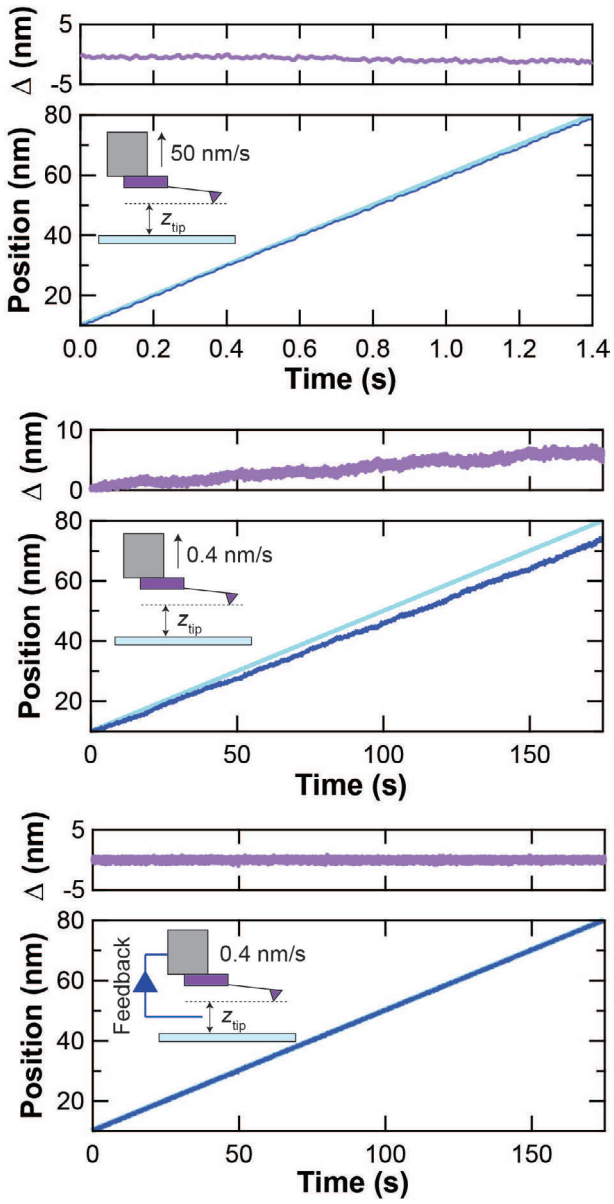

Figure 5.5: Moving the tip under three different conditions shows the benefits of position clamping during slow pulling. (a) At a moderate velocity of 50 nm/s, the requested tip position (*light blue*) is very similar to the measured tip position (*dark blue*), varying only a small amount (*purple*). (b) However, at the very slow speed of 0.4 nm/s, the difference is substantial by the end of the pulling range. (c) Adding feedback alleviates this effect.

on local optical measurements that allows for direct measurement of tip-sample separation in 3D. Surface determination via cantilever detection and this new local optical technique was essentially identical [0.0 ± 0.3 nm (mean ± std. dev, N = 86)], providing confidence that this technique can ultimately measure absolute tip-sample separation. In conjunction with feedback control of sample position, this work provides a means for long-term control of the tip-sample separation that is insensitive to drift of the AFM assembly. Three dimensional control of tip-sample separation will enhance studies of protein refolding experiments, whose sensitivity to drift is exacerbated by the short contour lengths of proteins. In addition to force spectroscopy applications, this new direct measurement of tip position can be used in several interesting and potentially useful ways, including imaging based on z_{tip} while holding the force constant based on z_{lever}. Further, we expect that variation in feature width in tip-based nanomanufacturing (e.g. dip pen lithography) due to fluctuations in meniscus dimensions can be minimized by stabilizing the tip-sample separation.

Chapter 6

Routine and timely sub-picoNewton force stability and precision for biological applications

This chapter is adapted from Reference [36].

6.1 Introduction

Up to this point, this thesis has been primarily concerned with reduction of positional drift. Yet, if one wants to make precise measurements over long periods (seconds to tens of minutes), positional drift is only part of the problem. Force drift also occurs.[21, 77] Force drift is particularly troublesome in force spectroscopy, an exciting class of experiments that includes mechanically unfolding and refolding individual proteins [14, 18, 78, 79, 15, 23, 80]. DC modes of imaging also suffer from this drift [21]. Originally we reduced the effect of force drift during imaging by taking a new force curve at the end of each line in an image, as described in Section 3.3. A related problem is the extended periods of time, often hours or even overnight [22], required for the AFM to "settle" after loading an AFM tip. Ideally, one could routinely load cantilevers and have effectively zero force drift after a minimal settling time. Many AFM-based experiments would also benefit from sub-picoNewton (pN) force precision, which has yet to be achieved over a broad bandwidth in liquid. Sub-pN force precision in a limited bandwidth has been demonstrated for protein folding using lock-in detection [34]. However, this approach limits the force detection to a narrow bandwidth around the drive frequency (20 Hz), and complicates interpretation due to a significant drive amplitude (5 nm). Thus, both force stability and force precision in liquid need improvement. For broad utility,

such improvements should use commercially available cantilevers.

Force measurements with AFM rely on an underlying assumption: changes in tip deflection (Δz) arise only from changes in the applied force (F). Or, in other words, the zero-force position of the cantilever (z_0) does not depend on time. Force is then determined using $F = -k\Delta z = -k(z_{tip} - z_0)$, where k is the cantilever stiffness and z_{tip} the instantaneous deflection of the cantilever (Figure 6.1). In this chapter, we show that, for an important class of silicon nitride cantilevers, z_0 is not constant, but drifts significantly. Further, we show that the short-term (0.1-10 s) and the long-term (minutes to hours) force noise of these soft (k = 5-60 pN/nm) cantilevers is dominated by the gold coating. By removing the gold and the underlying chromium, we achieved a force precision of ∼0.5 pN over a broad bandwidth (0.01-10 Hz) in liquid with a minimal settling time.

6.2 Results

6.2.1 The AFM cantilever is the primary source of force drift

Cantilevers are coated in gold primarily to enhance reflectivity, which is assumed to increase the signal-to-noise ratio [81]. Yet, coating cantilevers only on the back side leads to a substantial thermal-induced force drift due to the bimetallic effect [82, 83]. Coating the cantilever on both sides maintains increased sensitivity while minimizing such temperature-induced drift (e.g., Figure 6.2). Even for fully coated cantilevers, recent work points to material properties of the gold coating itself as the primary limit to low-frequency force precision [84]. Paolino and Bellon uncovered this effect by measuring the positional power spectral density (PSD) of gold-coated and uncoated silicon cantilevers (k = 200 pN/nm) in air at room temperature [84]. The main difference in the PSDs was at low frequency (f) in a bandwidth (3–100 Hz) well below the resonance frequency of the cantilever. Specifically, the low-frequency PSD of the gold-coated cantilevers rose as $1/f$ while those of the uncoated cantilevers remained flat, leading to a ∼100-fold difference in the PSD at 3 Hz. The authors quantitatively modeled their data by incorporating a viscoelastic term into the mechanical response of the cantilever. More qualitatively, gold's contribution to low-frequency

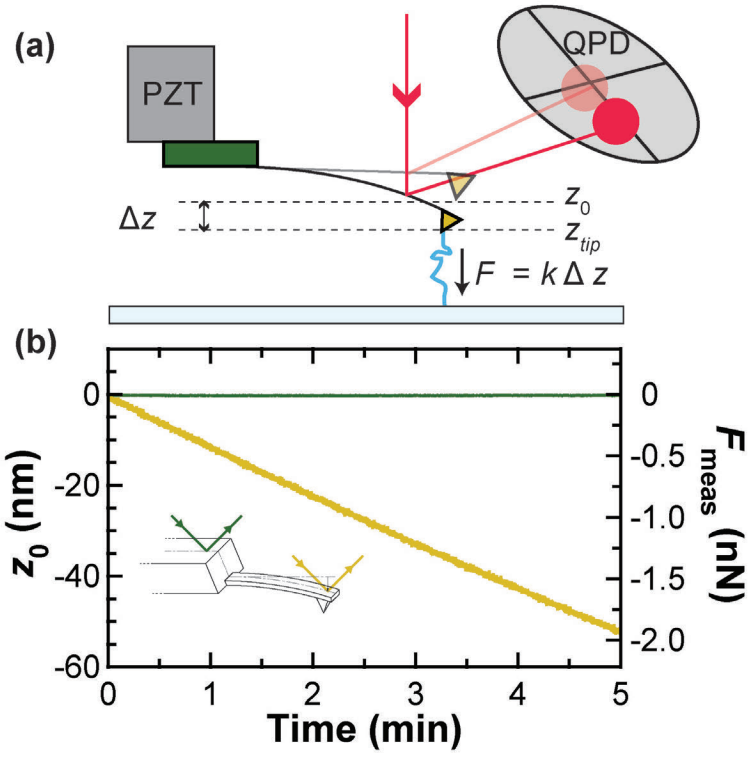

Figure 6.1: The cantilever is the primary source of force drift. (a) Schematic of a force spectroscopy experiment. The AFM tip is attached to a molecule and retracted from the surface. The force that the molecule exerts on the cantilever is determined by the deflection ($z_{tip} - z_0$), as measured on a quadrant photodiode (QPD). (b) With no molecule attached, the zero force position z_0 (*gold*) of a cantilever (short Biolever) was measured as a function of time two hours after wetting. A similar record (*green*) was measured after repositioning the detection laser onto the chip holding the cantilever and scaled using the cantilever's sensitivity (S = 0.043 V/nm) and stiffness (k = 37 pN/nm). This comparison demonstrates that the primary source of force drift is the cantilever. From Reference [36].

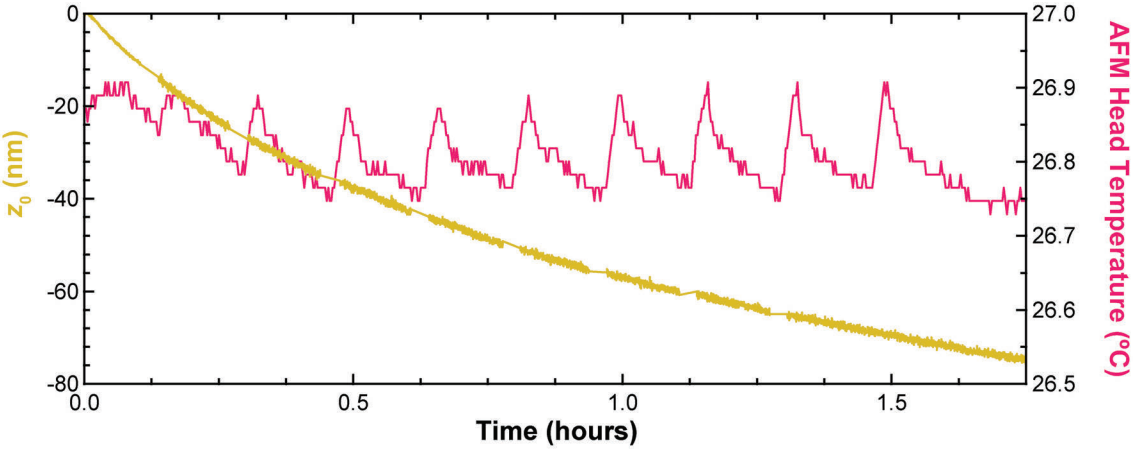

Figure 6.2: Drift in z_0 was not correlated to temperature. In this experiment, the temperature stabilization and the data collection were briefly turned off every ∼10 min starting 1 hr after mounting a gold-coated cantilever (short Biolever). The AFM head temperature (*pink*) varied periodically, while the zero force position of the cantilever (*gold*) drifted monotonically. From Reference [36].

force noise is described with terms like "cracking" and "aging"— in scientific discussions, if not often in the scientific literature. We sought to determine the relevance of Paolino and Bellon's work to biophysics by exploring (*i*) long times (hours), (*ii*) a liquid environment, (*iii*) softer cantilevers (5–60 pN/nm), and (*iv*) effects of a nearby surface. Our work focused on changes in z_0 over hours as well as a bandwidth (0.01–10 Hz) useful for force spectroscopy. Force spectroscopy, like most biological applications of AFM, is done in liquid, where viscous damping is much larger than in air. Also, force spectroscopy typically uses the softest cantilevers available, where the positional PSD in liquid is >100-fold larger at low frequency (∼1 Hz) than for the stiffer cantilevers (k =200 pN/nm) in air. This difference arises because soft cantilevers are no longer resonant when they are within a few hundred nanometers of the surface [85]. Rather, they are overdamped due to the increased hydrodynamic drag that distributes the thermal energy over a broad bandwidth. A simple test using a commercial AFM (Cypher, Asylum Research) pointed to the cantilever as the primary source of force noise in liquid for a fully coated cantilever. In this test, [82] we compared the drift of the cantilever to the apparent drift of the chip on which the cantilever was mounted (Figure 6.1, inset). More specifically, we loaded a cantilever (k = 37 pN/nm, short Biolever, Olympus), let the AFM settle for 1 hr, and measured z_0 for 5 min. Next, we positioned the detection laser to reflect off of the chip and acquired data for another 5 min. We determined an effective force drift for the chip by using the cantilever's spring constant and sensitivity (S = 0.043 V/nm). As shown in Figure 6.1, b, the drift rate on this cantilever (gold) was ∼800-fold higher than effective drift rate on the chip (380 vs 0.5 pN/min, respectively). This experiment isolated the cantilever as the primary source of drift, rather than the external opto-mechanical system (e.g., laser-pointing noise, mechanical drift in the QPD, and voltage drift in the electronics).

6.2.2 Long-term drift characteristics

Long-term drift in z_0 was substantial, moving beyond the range of the AFM's detection system. We accommodated this drift by periodically re-zeroing the QPD. Specifically, we mounted long Biolevers [k = 6 pN/nm (nominal); Olympus], performed a sensitivity calibration, retracted

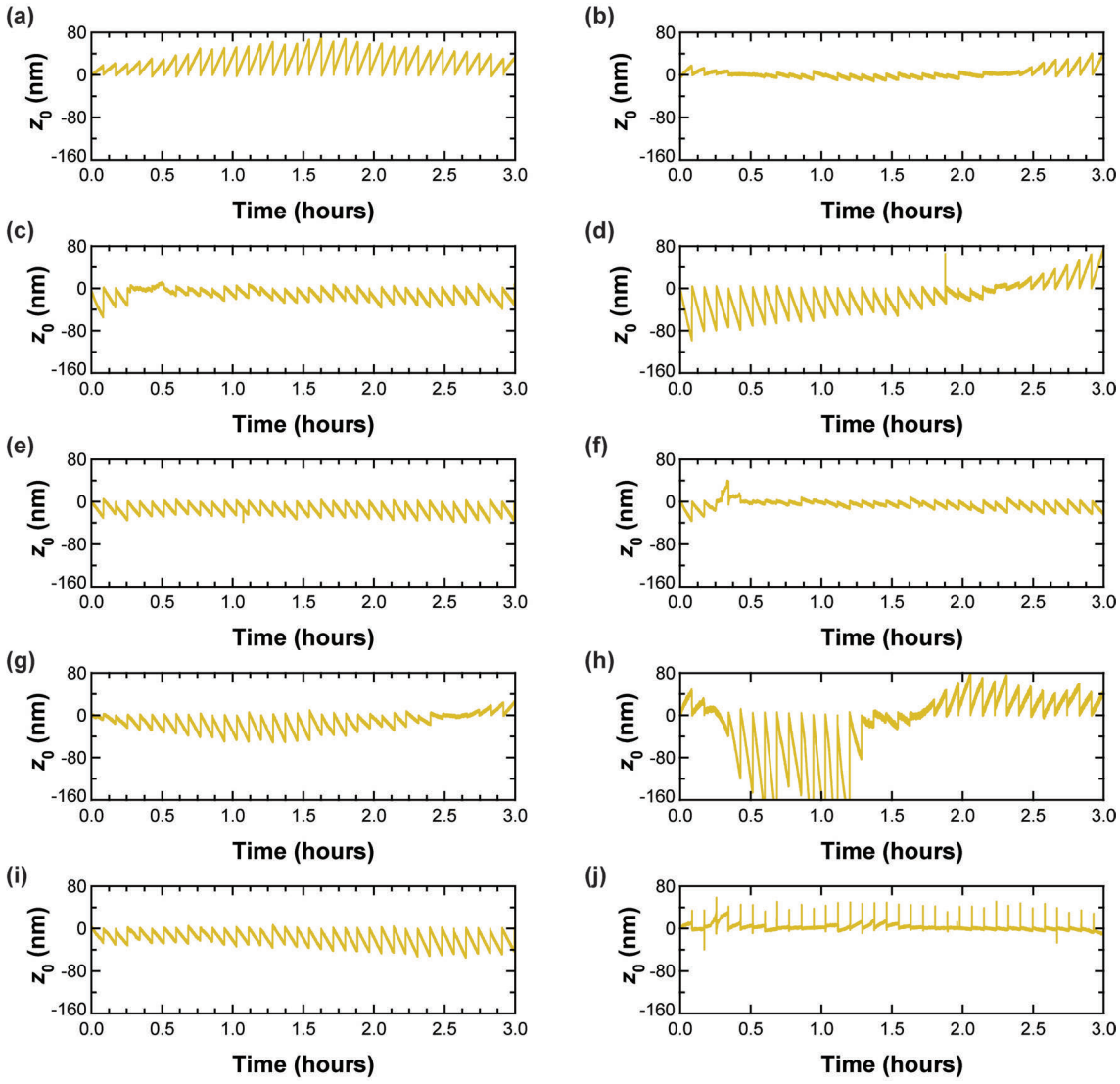

Figure 6.3: Raw data traces of gold-coated long Biolevers. In order to keep the laser spot in the linear region of the detector, we touched the surface and re-zeroed the QPD every 5 min. However, this caused discontinuities in the trace. To create the continuous traces shown in Figure 6.5, we developed a simple splicing algorithm that (*i*) finds the discontinuities by differentiating the trace and looking for peaks, (*ii*) finds the value of the trace before and after the discontinuity by averaging 20 points on each side of it, (*iii*) takes the difference between these values, and (*iv*) shifts the portion of the trace after the discontinuity by this difference. Individual points, used as delimiters, were also removed. In traces (a) through (i), the data collection was paused during the process of touching the surface. In trace (j), due to an update of the AFM software, the data collection was continued during the process of touching the surface, leading to large spikes. For this trace, the data during those periods was also removed during splicing to make this record consistent with the prior records. From Reference [36].

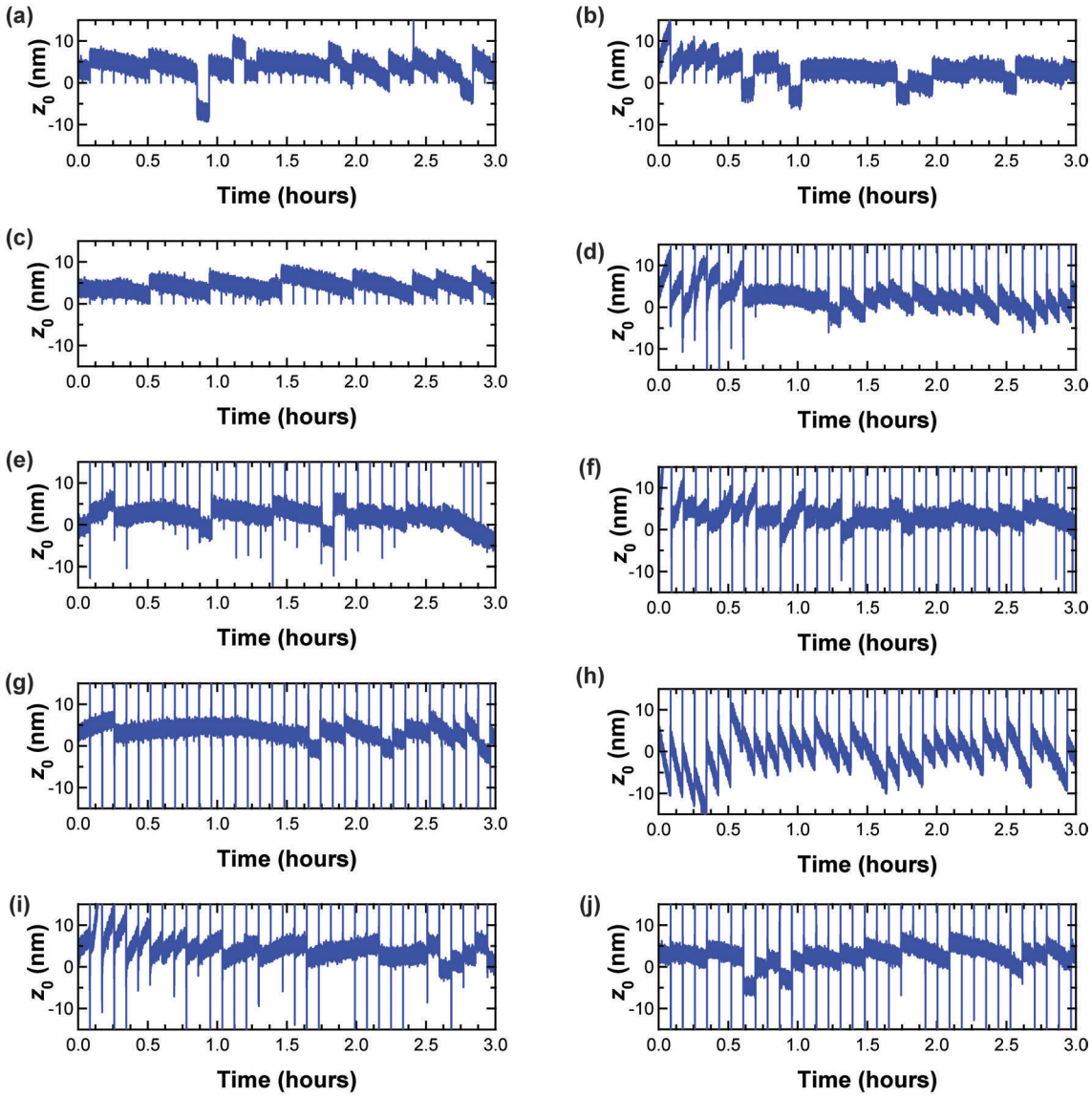

Figure 6.4: Raw data traces of uncoated long Biolevers. These records were processed as described in Figure 6.3. The final seven records (d-j) show large spikes due to an update in the AFM software, which led to data collection during the process of touching the surface. For these traces, the data during those periods was also removed during splicing to make this record consistent with the prior records. From Reference [36].

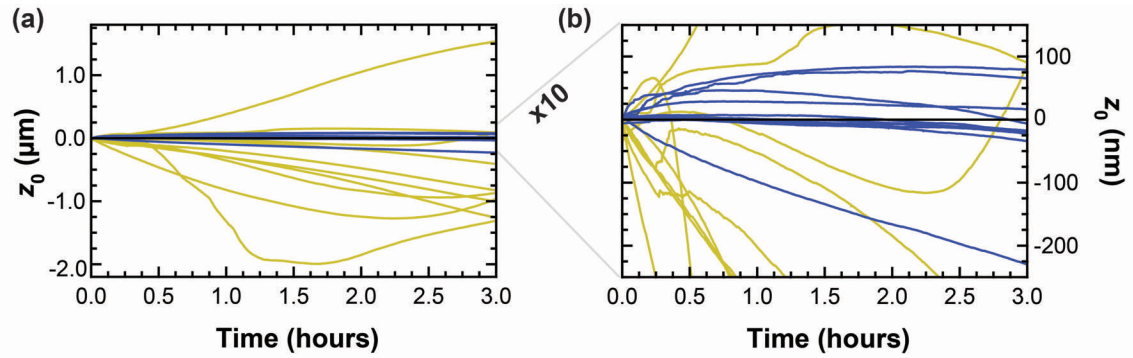

Figure 6.5: Drift in the zero force position (z_0) on gold-coated (*gold*) versus uncoated (*blue*) cantilevers. (a) Three-hour-long traces of z_0 show that gold-coated cantilevers drift significantly more than uncoated ones. (b) Ten-fold expanded scale shows residual drift on uncoated cantilevers. From Reference [36].

the tip 100 nm, and then started data acquisition. Every 5 min, the tip was touched to the surface, repositioned 100 nm above the surface, and the QPD was rezeroed. Individual 5-min records (Figures 6.3 and 6.4) were algorithmically stitched together into single long records (Figure 6.5). Using this protocol, we quantified drift over arbitrarily long periods, limited by evaporation from the fluid cell (a difficulty in our semi-arid climate). All the gold-coated cantilevers tested exhibited significant drift in the initial several hours after mounting (Figure 6.5, gold). The sign of the initial drift was not constant, nor was the drift monotonic. Hence, the transiently low drift rate seen in several traces did not imply a stable z_0 was being reached. Rather, many of these traces showed an onset of substantial drift in the opposite direction. Therefore, a single observation of low drift at a particular time does not guarantee low force drift during subsequent experiments. Finally, independent of the details of individual records, the magnitude of this drift and its persistence is noteworthy.

6.2.3 Drift not correlated with laser intensity

We speculated that the cause of the drift was the laser damaging the gold. Under this hypothesis, the drift rate should be a function of laser intensity. Hence, we measured z_0 for 100 s at three hours after mounting at different intensities both on the commercial AFM and on our custom AFM [35]. The latter's detection laser was very stable ($\sim$0.002 % , Δ f = 0.02-100 Hz). The resulting long-term drift rate on both instruments was independent of the laser power (Figure 6.6), suggesting that slow drift in z_0 is not caused by straightforward light-induced effects.

6.2.4 Removing gold improves stability

In contrast, removing the gold from the cantilever had a profound effect on drift (Figure 6.5, blue). Drift for uncoated long Biolevers was reduced 10-fold over 2 hrs in comparison to gold-coated ones: 70 nm vs. 900 nm (N = 10, rms), respectively. Moreover, a majority (60%) of the uncoated cantilevers were even quieter, with an average drift of 12 nm (rms). The uncoated cantilever with the worst integrated force noise (1.6 pN) outperformed the quietest gold-coated cantilever (2.6 pN),

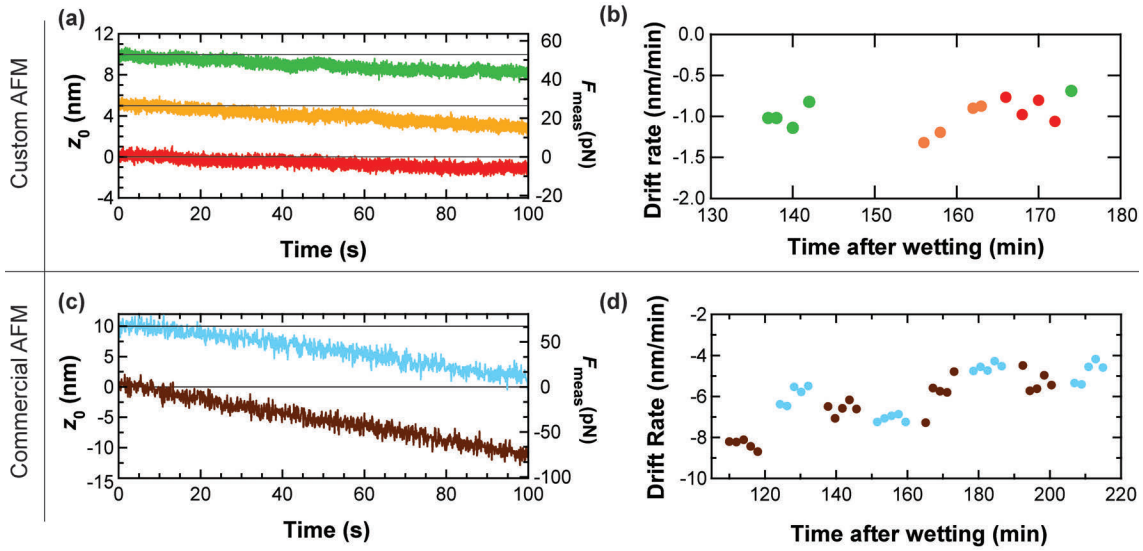

Figure 6.6: Long-term drift was not correlated with laser intensity on two instruments. (a) Zero-force position and resulting apparent force are plotted for three different laser powers: 0.02 mW (*red*), 0.04 mW (*orange*), and 0.08 mW (*green*) on the custom AFM. Traces displaced for clarity. The grey lines denote the initial z_0 for each record. (b) Drift rate as a function of time at various laser powers colored as in (a). Data collected with gold-coated tip (short Biolever, Olympus) starting 130 minutes after wetting. (c) Zero-force position and resulting apparent force plotted for 0.1 mW (*cyan*) and 0.9 mW (*brown*) on the commercial AFM with gold-coated long Biolever (Olympus), where 0.9 mW is the normal laser power for the commercial instrument. To obtain these traces, we manually changed the laser power, recorded data with the Cypher's Logger function, and scaled the traces by the optical lever sensitivity. Traces displaced for clarity. (d) Drift rate as a function of time at various laser powers, colored as in (c). Hence, at 2 hours, the drift rate on both systems and for both short and long Biolevers was not correlated with laser power. From Reference [36].

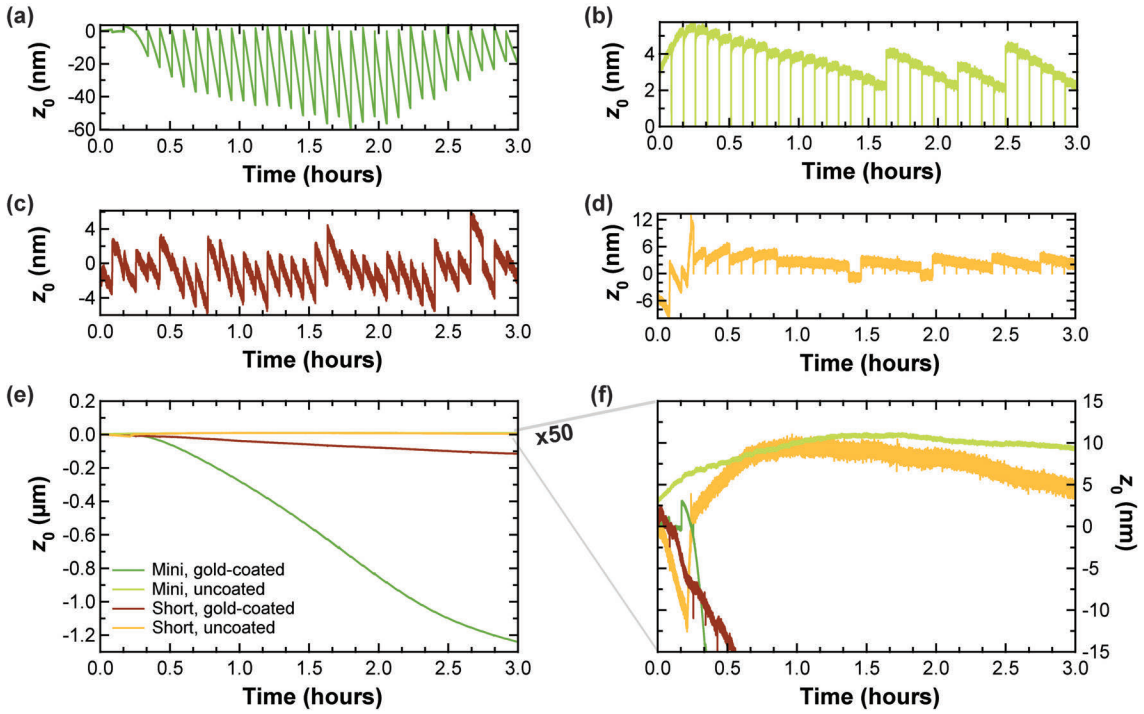

Figure 6.7: Zero-force position drift of different types of cantilevers. (a)-(d) Unspliced data on Biolever Mini (Olympus) with (a) and without (b) gold; and on short Biolever (Olympus) with (c) and without (d) gold. (e) Drift over three hours, with same color scheme as in (a) through (d). (f) The same traces with a smaller vertical scale. From Reference [36].

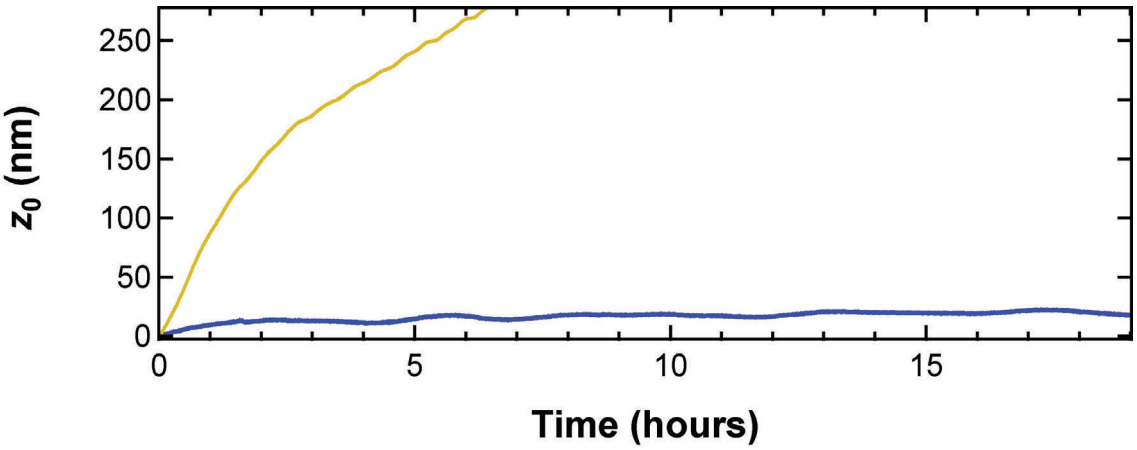

Figure 6.8: Force drift on gold-coated (*gold*) versus uncoated (*blue*) cantilevers, as measured in the custom AFM. The traces show zero-force position (z_0) over 19 hours, although the gold-coated cantilever drifted out of range of the detector after only 6 hours. Evaporation effects were not an issue on the custom AFM because it contains up to about 3 mL of fluid as compared to the small volume ($\sim$200 μL) of the commercial AFM. We note this plot assumes the QPD voltage is linear over its full voltage range with cantilever deflection, a condition that may not be true at higher deflections (e.g., $>$ 150 nm).

From Reference [36].

when both cantilevers were allowed to settle for 3 h. We obtained similar results for two other types of cantilevers (short Biolever and Biolever Mini; Figure 6.7) and using the custom AFM (Figure 6.8). Hence, gold was the primary cause of long-term drift in z_0. This result is consistent with prior work using a variety of cantilevers and conditions (e.g., cantilevers coated on one side in liquid [82, 83, 86] and partially [87] or fully [84] coated on one side in air).

6.2.5 Removing gold improves precision

Removing the gold coating came with a roughly 10-fold loss in reflectivity from the cantilever. On the commercial AFM, this loss led to a substantial decrease in sensitivity (volts per nanometer) (Figure 6.9, a). Despite the reduced reflectivity, uncoated cantilevers showed improved precision, both in position and in force. To highlight these improvements, we measured z_0 for 100 s at ∼3 hrs after mounting a long Biolever (Figure 6.9, b). The trace for an uncoated cantilever (Figure 6.9, b, *blue*) shows significantly less drift than one using a gold-coated cantilever (Figure6.9, b, *gold*). The PSD of uncoated records show less positional noise than corresponding gold-coated records (Figure 6.9, c). Moreover, this improvement existed over three decades of bandwidth (0.01-10 Hz). At higher frequencies, the coated cantilevers had comparable noise to uncoated ones. Hence, reduced reflectivity does not limit the force precision. Rather, the gold coating limits force precision and stability on both short- and long-time scales (Figure 6.9, d), a result confirmed on the custom AFM, which did not have reduced sensitivity due to differences in electronics (Figure 6.8 and 6.10). We expect that this insight will generalize to other classes of cantilevers, instruments and assays, as long as there is sufficient light incident upon the QPD so that signal is not limited by detector noise. To illustrate this generalization, improved force precision was maintained when using an uncoated cantilever in conjunction with a gold-coated substrate (Figure 6.11), a common surface preparation in biophysics [88, 89] and nanoscience.[8, 90]

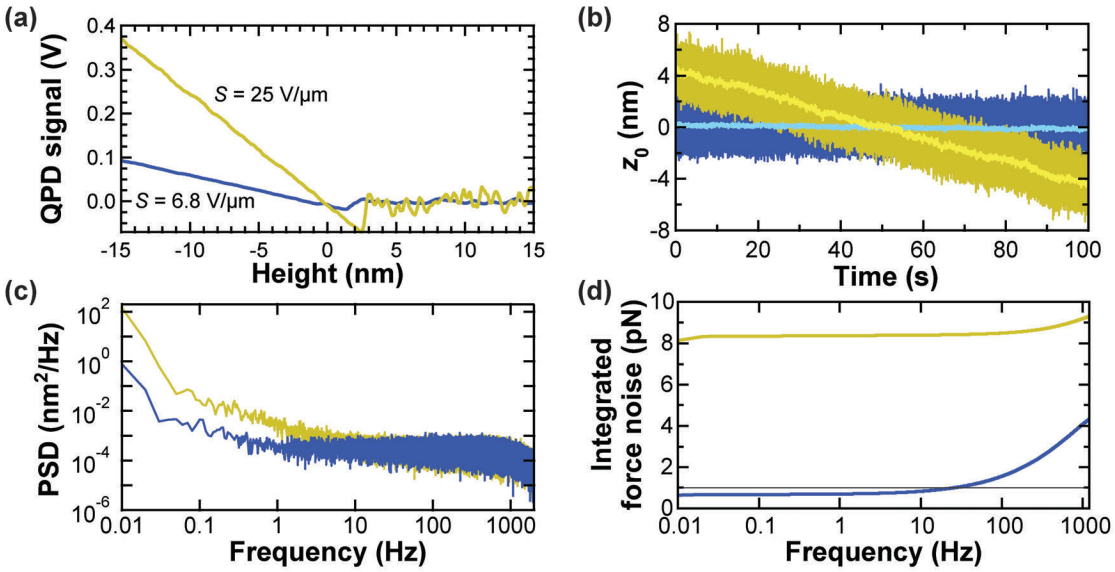

Figure 6.9: Effect of gold removal on sensitivity and precision. (a) Sensitivity of gold-coated (*gold*) and uncoated (*blue*) cantilevers. (b) Time records of zero-force position (z_0) for gold-coated (k = 6.8 pN/nm) and uncoated (k = 7.1 pN/nm) cantilevers. High-bandwidth data (2.5 kHz) is shown in dark colors and smoothed data (10 Hz) in light colors. Note that, while the gold-coated cantilever has an approximately linear drift, there can be significant short-term fluctuations. (c) Averaged power spectral density of five consecutive 100 s records such as those shown in (b). (d) Integrated force noise from the records shown in (c). Data taken on the commercial AFM. From Reference [36].

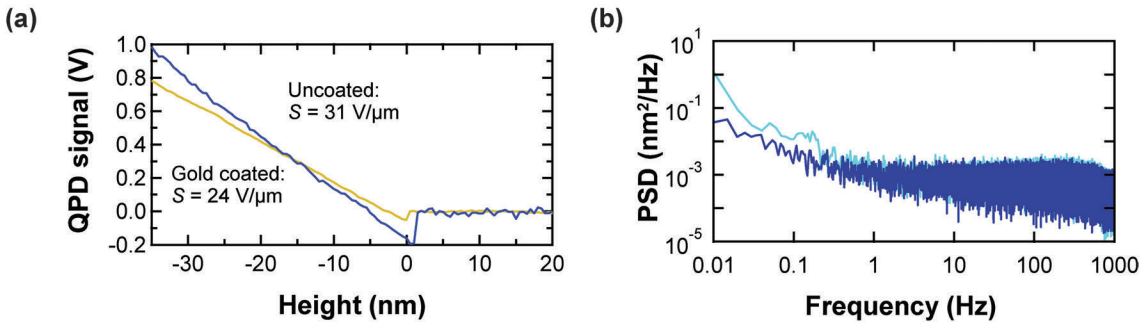

Figure 6.10: Effects of gold removal on sensitivity and PSD in z_0 on the custom AFM. (a) Typical sensitivity calibration curves on gold-coated (*gold*) and uncoated (*blue*) levers (long Biolever, Olympus) show similar sensitivity, in contrast to the commercial AFM. The commercial instrument's sensitivity is dependent on the total reflected light, while the custom AFM is not. On the commercial AFM, deflection is based on the difference in light falling on the upper and lower halves of the QPD $[(A+B)(C+D)]$, where A, B, C, and D represent the four quadrants, while the optically stabilized AFM is based on the normalized difference $[((A+B)(C+D))/(A+B+C+D)]$. (b) PSD of z_0 of an uncoated cantilever acquired with the custom AFM (*dark blue*) is similar to that acquired with the commercial AFM (*light blue*).We note that the analog divider used in our electronics did not add observable excess noise at relevant frequencies (<10 kHz) for these soft cantilevers. From Reference [36].

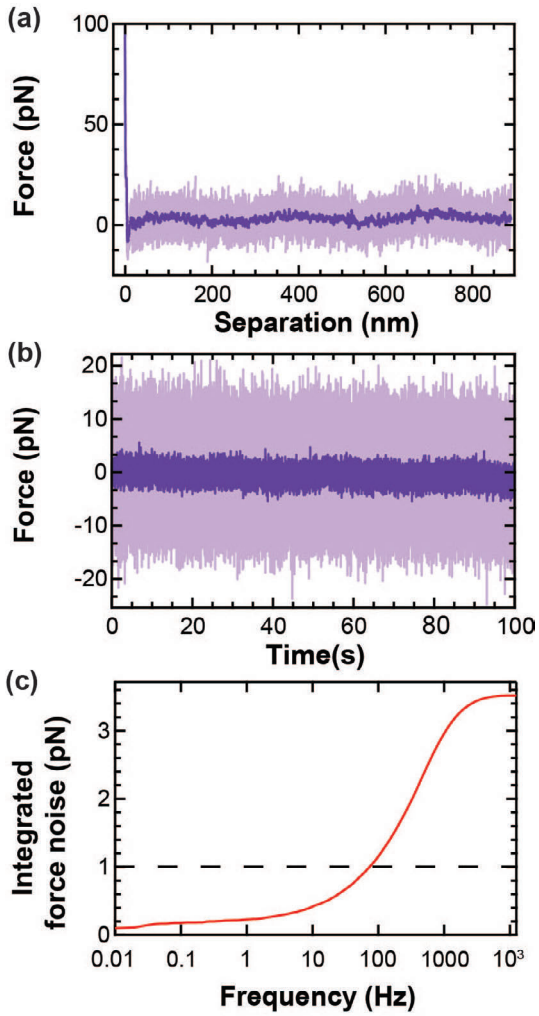

Figure 6.11: Force calibration curve and measurement of force noise of an uncoated long Biolever when using a gold-coated substrate. (a) A representative approach portion of a force curve at 2.5 kHz bandwidth (*light purple*) and data smoothed to 50 Hz (*purple*) when using a gold substrate (1 nm chromium and 4 nm gold layer). (b) Time record of z_0 for uncoated long Biolever 100 nm above the gold substrate collected at 2.5 kHz bandwidth (*light purple*) and smoothed to 50 Hz (*purple*). (c) Corresponding integrated force noise of the uncoated lever shown in (b) showing a sub-pN force precision below 76 Hz. Overall, this data illustrates that uncoated cantilevers can be used with equal precision when using gold-coated surfaces. From Reference [36].

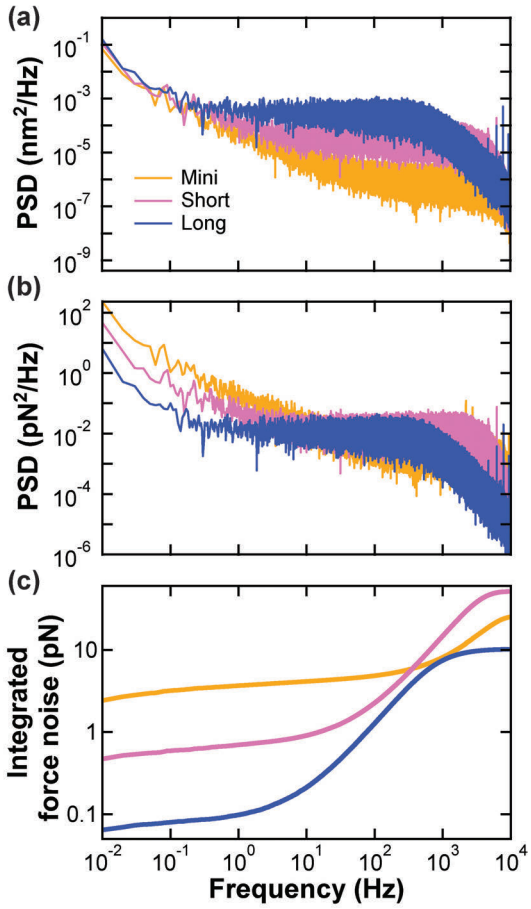

Figure 6.12: Noise on three different uncoated cantilevers. (a) Positional power spectral density (PSD) based on five consecutive 100 s records for a long Biolever (*blue*, k = 6.2 pN/nm), short Biolever (*pink*, k = 20 pN/nm), and Biolever Mini (*orange*, k = 58 pN/nm). Low-frequency positional noise was the same for each cantilever, since it was dominated by instrument noise. (b) Force PSD determined from the data in (a). (c) Integrated force noise shows that the softest lever has the lowest total noise over the full bandwidth of the measurement. From Reference [36].

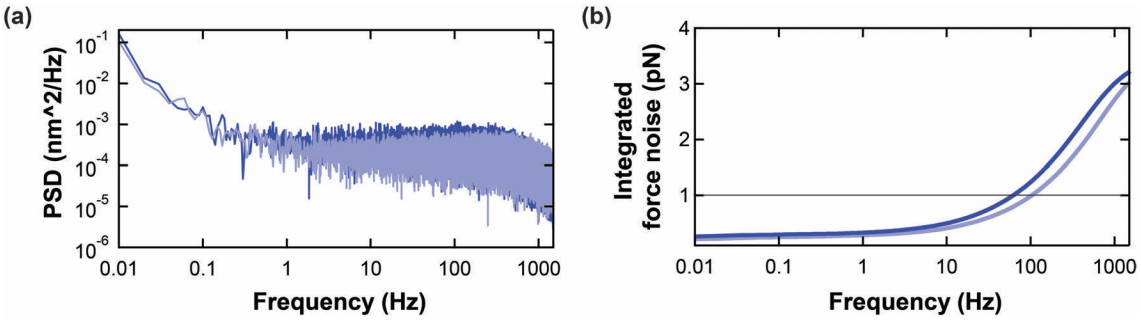

Figure 6.13: Cantilever noise near and far from a surface. (a) Power spectral density and (b) integrated force noise of an uncoated long Biolever (k = 6.2 pN/nm) when it is 100 nm (*dark blue*) and 2 μm (*light blue*) off the surface on the commercial AFM (Cypher, Asylum Research).The integrated noise was slightly higher near the surface, as expected due to the increased hydrodynamic drag. From Reference [36].

6.2.6 Softer cantilevers outperform smaller ones at low frequency

Next, we investigated which cantilever yielded the best force precision, focusing on a popular class of cantilevers used in biophysical experiments (Figure 6.12). Specifically, we measured the positional and force noise for an uncoated Biolever Mini (k = 58 pN/nm; l = 38 μm), a short Biolever (k = 20 pN/nm; l = 60 μm), and a long Biolever (k = 6.2 pN/nm; l = 100 μm), all from Olympus. At the lowest frequencies, the positional PSDs of all three cantilevers were nearly identical, showing that instrumental noise dominated over thermal noise (Figure 6.12a). The crossover to thermally limited positional noise occurs when the PSD response becomes flat with respect to frequency. In this thermal regime, the smaller cantilevers had less positional noise, as expected [43]. To determine which cantilever exhibited the highest force precision, we calculated the force PSD by scaling the positional PSD by the cantilever stiffness (Figure 6.12b). Our data show that while all three cantilevers had nominally similar force spectral sensitivity ($\sim$0.1 pN/$\sqrt{Hz}$) around 10-500 Hz, the shortest cantilever was the quietest, also as expected. However, at low frequencies where instrumental drift dominated, long Biolevers had decreased force noise because of their lower stiffness. We also note that the force precision depends weakly on the height of the cantilever over the surface (Figure 6.13). While spectral sensitivity is a common metric in AFM, many biophysical assays are sensitive to the total applied force. Thus, the crucial metric is the integrated force noise in a particular bandwidth. This bandwidth needs to encapsulate the total duration of the experiment, so that the dynamics under study are not altered. State-of-the-art AFM-based force spectroscopy experiments last up to about 10 s [18, 22]. We chose a 100 s window to encompass these and future studies. With this metric, the long Biolever showed 1 pN force precision from 0.01-76 Hz, while the short Biolever and the Biolever Mini had 1.9 pN and 4.7 pN of noise, respectively. Hence the softest cantilever studied, the long Biolever, exhibited the best force precision (Figure 6.12c).

Why does the longer and softer cantilever yield the best force precision? This result runs counter to the traditional wisdom for AFM. Typically one expects the best force precision to be

achieved with shorter cantilevers with a reduced drag coefficient (β) [91]. This expectation is based on the fluctuation-dissipation theorem, which yields a force precision of $\sqrt{4k_bT\Delta f\beta}$. However, this theorem assumes that thermal fluctuations limit detection. Our work highlights that for applications on time scales longer than about 1 s, thermal noise does not limit the force precision.

6.2.7 Sub-pN precision after minimal settling time

Ideally, sub-pN force precision and stability would be routinely accessible without extended settling time using a commercial cantilever and instrument. To demonstrate this, we measured fifteen uncoated long Biolevers 30 min after wetting using the commercial AFM. The average force precision of all fifteen cantilevers was 1.0 ± 0.7 pN (0.01-10 Hz) based on five consecutive 100 s records for each cantilever. Moreover, a majority (9 out of 15) of the cantilevers tested had a force precision below 1 pN (0.54 ± 0.02 pN). Hence, the simple removal of gold enables routine access to sub-pN force precision just 30 min after mounting.

6.2.8 Sub-pN force precision while stretching DNA

This sub-pN force precision was also achieved in a common single-molecule biophysics assay, stretching DNA [88, 92, 93, 94, 20]. DNA was nonspecifically adsorbed onto mica, and the tip was pressed onto the surface. In the first experiment, we retracted the stage at a slow velocity (v_{stage} = 400 nm/s). The resulting force-extension curve was very quiet by AFM standards and shows the canonical overstretching transition at about 65 pN (Figure 6.14, a) [95, 96]. We quantified the force precision by stretching a DNA molecule that was attached to the tip by >30 nm and holding it at variable extensions for 100 s (Figure 6.14, b). Analysis shows that the force stability and precision was excellent, as demonstrated by full bandwidth records smoothed to 10 Hz (effective data rate = 20 pts/s). When the integrated force noise was calculated, we achieved better than 0.6 pN force precision (0.01-10 Hz) on three different cantilevers (Figure 6.14, c).

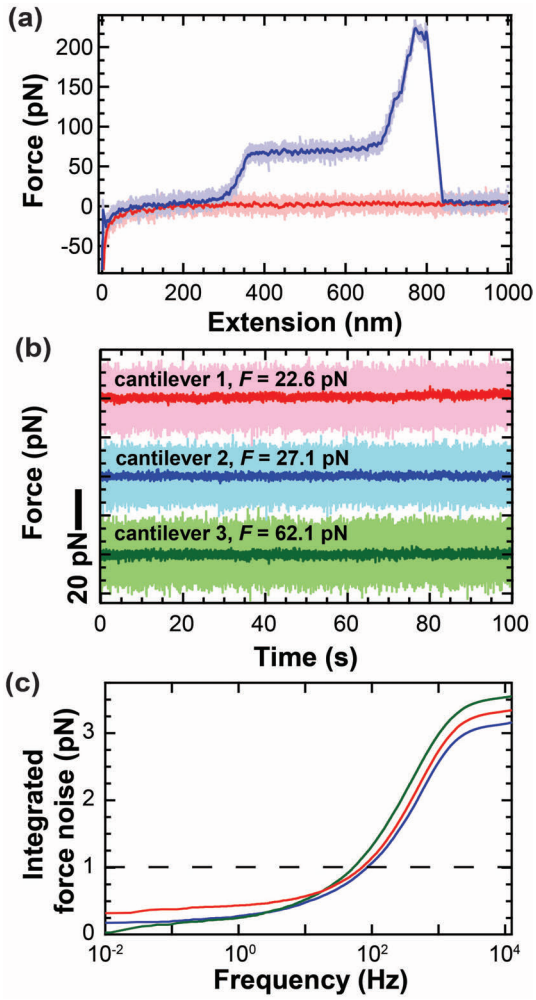

Figure 6.14: Stretching DNA with uncoated cantilevers exhibits sub-pN force stability. (a) Force-extension curve of DNA at a 400 nm/s pulling velocity. The high-bandwidth data (2.5 kHz) for approach (*light pink*) and retraction curve (*light purple*) was smoothed (100 Hz, *purple* and *red*). (b) Force-versus-time trace smoothed to 10 Hz while holding DNA at constant extension at 22.6 pN (*pink*), 27.1 pN (*blue*), and 62.1 pN (*green*). High-bandwidth data are shown in light colors and traces displaced for clarity. (c) Integrated force noise of traces shown in (b). From Reference [36].

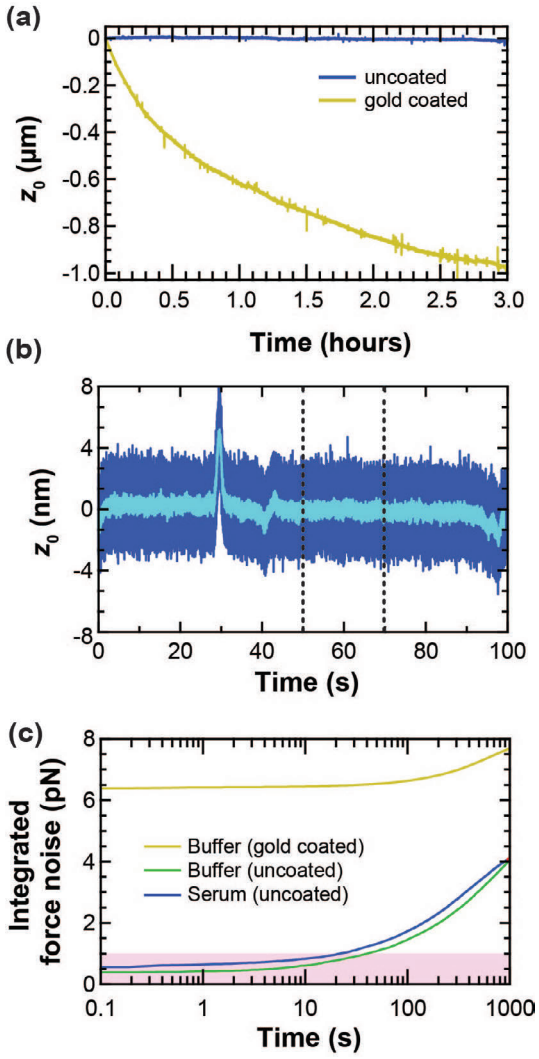

Figure 6.15: Drift in 2% adult horse serum. Data were acquired as described for previous drift curves. (a) Long-term drift for gold-coated (*gold*) and uncoated (*blue*) cantilevers shows that removing the gold dramatically reduced drift in these conditions. (b) However, a more detailed examination of uncoated cantilever records (*blue*) reveals the presence of large transient deflections in z_0 that are consistent with particulates (e.g. protein aggregates) moving through the detection beam. Baseline fluctuations in z_0 for uncoated cantilevers appeared to increase in 2% serum relative to aqueous buffer, consistent with many smaller events between larger transients. (c) Integrated force noise for a relatively quiet section of data, marked with dotted lines in (b), showed sub-pN force precision ($\Delta f = 0.1 - 20$ Hz; *cyan*) could be achieved between major events. The integrated noise for a quiet section is much smaller than a gold-coated lever in buffer, though not as small as an uncoated lever in buffer, as expected. From Reference [36].

6.2.9 Effect of impure background fluid on precision

Force stability in single molecule force spectroscopy is now limited by tip-sample drift and the stability of the bio-molecular attachments, which is typically based on nonspecific adsorption. For live cell assays needing serum-based medium, removing gold dramatically reduces the long-term drift (Figure 6.15, a). However, force precision in serum is worse than in buffer alone, consistent with particulates diffusing through the detector beam (Figure 6.15, b,c).

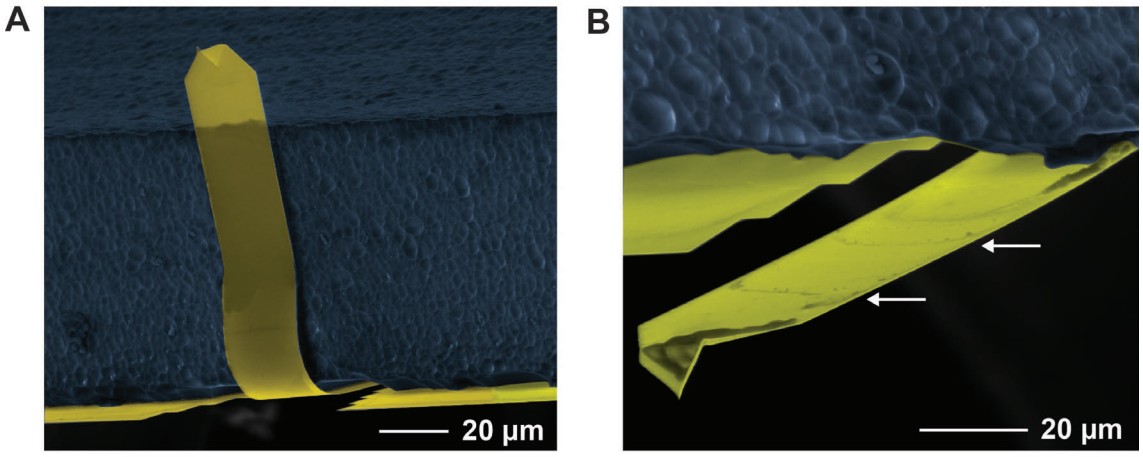

Figure 6.16: Folding of soft cantilever with wetting causes high stress and alteration to the gold coating. (a) Scanning electron micrograph of a long Biolever after wetting shows the cantilever adhering to the chip. This cantilever was subsequently induced to unfold by dipping in alcohol. (b) After unfolding, a second SEM shows alterations to the gold coating (*dark areas*). We suspect that such folding and release leads to residual stress. In the AFM, cantilevers that are originally folded often spontaneously unfold after several minutes. From Reference [36].

6.3 Conclusion and speculative mechanisms

In calculating force for AFM, researchers have typically assumed that the zero-force position of the cantilever was constant. Our work shows that this is a poor assumption for a fully gold-coated cantilever, even several hours after mounting a tip. However, the simple removal of gold led to sub-pN force precision 30 min after mounting for a majority of cantilevers tested, even though the cantilever's reflectivity was reduced. Further, removing the gold dramatically reduced long-

term drift. We speculate that the long-term drift in z_0 over hours is tied to the mechanical stress of wetting. It is not uncommon for soft cantilevers to fold backwards and stick to the chip (Figure 6.16). One would expect that the residual stress after such a significant mechanical deflection is large. Within this hypothesis, such large deformations must affect gold-coated cantilevers differently than uncoated cantilevers. Moreover, the exact mechanics of wetting may be highly variable and therefore lead to the observed variability in the drift of nominally identical cantilevers. Independent of the exact mechanism, sub-pN force sensitivity, which is typically associated with optical traps and magnetic tweezers [43] is now routinely accessible with a commercial AFM in liquid using a simple modification to popular commercial cantilevers. Our results should generalize to any AFM with a sufficiently sensitive and stable detection system. Thus, we expect that this enhancement in AFM's core function — measuring force — can immediately benefit research in biophysics and nanoscience.

Chapter 7

Unfolding and refolding studies of the membrane-bound protein bacteriorhodopsin

7.1 Introduction: bacteriorhodopsin as a model membrane protein

Proteins associated with biological membranes are critical gatekeepers to the cell and a major frontier in biophysical research. Although they comprise ∼30% of the proteome [97] and over 60% of drug targets [98], membrane proteins represent only about 600 of the 87,8000 structures in the protein data bank (PDB, http://www.rcsb.org/pdb)— less than 1%— as of February 2013. Protein structures are most commonly determined by x-ray crystallography, and membrane proteins have proven to be more difficult than soluble proteins to express, purify, and crystallize. Although the first high-resolution crystal structure of a protein was published in 1960, the first high-resolution crystal structure of a membrane protein was not published until 1985, and progress in obtaining subsequent structures has been slower for membrane proteins than for soluble ones [99]. Understanding of membrane protein folding has, similarly, proceeded more slowly than understanding of soluble protein folding. The amphiphilic nature of the lipid membrane means that the membrane-bound proteins exist in a partially hydrophobic and partially hydrophilic environment, meaning that the energetics of folding depend on the depth of a particular section of protein in the bilayer [100]. The two-stage model for helical membrane proteins, where helices insert into the membrane, then associate with one another, provides a general framework for thinking about membrane protein folding [101].

Bacteriorhodopsin (BR) [103] is a model membrane protein from the photosynthetic microor-

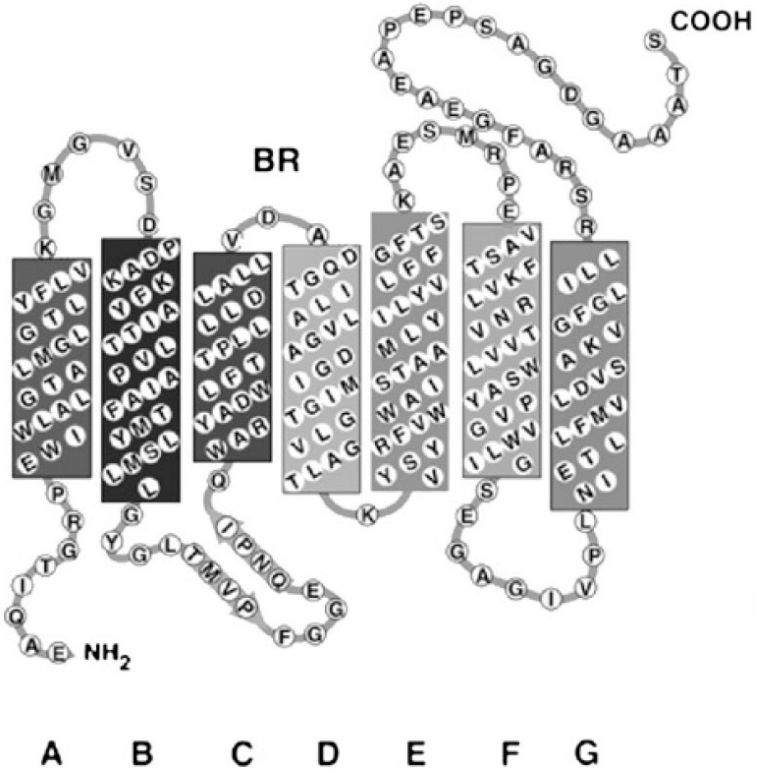

Figure 7.1: Schematic showing sequence, secondary structure, and topology of bacteriorhodopsin. The seven transmembrane helices are drawn as rectangles, and the beta hairpin between helices B and C with arrows. Note also the length and relatively large number of charged residues (aspartate and glutamate- D and E, respectively) in the C terminus. Reprinted from Reference [102], with permission from Elsevier.

ganism *Halobacterium salinarum* (also known as *Halobacterium halobium* [104]). Biologically, it functions as a light-activated proton pump for chemiosmotic photosynthesis [105]. With seven transmembrane helices [106], it is structurally similar to G-protein-coupled receptors (GPCRs), a class of membrane proteins important for human health. In its native membrane, known as "purple membrane," BR assembles into a 2D lattice of trimers. Purified, lyophilized purple membrane can be obtained commercially (Sigma). BR has been studied extensively using bulk biochemical [107, 108], single-molecule [109, 15], and computational [110, 111] techniques. It has been used in proof-of-principle experiments as a biological data storage mechanism [112], and its C helix, which inserts into the membrane in a pH-dependent manner, has been proposed as a cancer targeting mechanism, since tumors tend to have a lower pH than surrounding tissue [113].

BR is the membrane protein most commonly studied by AFM. It was first imaged at molecular resolution in biological buffer in 1990 [114]. To achieve this resolution, the BR was adsorbed to atomically-flat mica; glass is too rough to achieve molecular resolution. Because BR forms a 2D crystal in its native membrane, individual molecules of BR can be imaged without concern about diffusion. AFM images have also shown that the conformation of the trimers is force-dependent [115]. More recently, high-speed AFM results were able to capture dynamics of the 2D crystal formation [109] and transitions from the light-adapted to the dark-adapted state [7]. There is also a long history of mechanical unfolding of BR by AFM, starting in 2000 [15]. That work showed that monomers of BR unfold from the membrane in a mostly pairwise fashion, producing four characteristic main unfolding peaks. A number of extra unfolding peaks are also seen [116], and these vary depending on whether the pulling is from the C-terminal or N-terminal side [117]. These are termed "anchor points," as they result from points on the protein that are more strongly anchored into the membrane. BR molecules nonspecifically adsorbed to the tip show the same primary peaks as those covalently bound, though the first peak, involving the F and G helices, was easier to resolve when the molecule was covalently bound [15]. Finally, it has also been reported that BR folds into the membrane against an applied force, and under certain conditions intermediates could be observed during folding [79].

We sought to measure the folding and unfolding of BR at or near equilibrium conditions. Hopping back and forth between two folding states near equilibrium has been reported in soluble proteins [23], but not membrane proteins. This type of experiment has the potential to observe a large number of folding and unfolding transitions, allowing statistically significant conclusions to be made. By could observing many folding and unfolding transitions over a long period of time, we hoped to draw precise, quantitative conclusions about the folding landscape of BR.

7.2 Methods

7.2.1 Preparation of membrane patches

Lyophilized patches of purple membrane were obtained from Sigma and reconstituted as described in Appendix E. A detailed protocol for adsorption of purple membranes to mica has been published [71]. However, we wished to use glass because it integrates more robustly with the ultrastable AFM. This meant that we had to consider the surface chemistry of the glass. When mica is used as a substrate, one can simply peel off the top layer of the mica to expose a clean surface, with essentially the same surface chemistry every time. To prepare the BR slides on glass, we must Piranha clean the slides and either oxygen plasma clean them, leaving a fresh, negatively charged surface, or functionalize them with (3-Aminopropyl)triethoxysilane (APTES, Sigma). These full protocols are described in Appendices E and F. The C-terminal side of BR sticks more readily to the tip, since it is longer and contains more charged residues (Figure 7.1). It is therefore advantageous to have the C terminus facing up. In order to bias the membrane patches in this orientation, we deposit them at low pH [118]. The membrane patches are prone to aggregation, but can be separated in the bath sonicator (Vibracell, Sonics) without noticeably damaging them.

7.2.2 Mechanical unfolding and refolding

When a bacteriorhodopsin sample is first put into the ultrastable AFM, the membrane patch is located using the label-free optical method described in Chapter 4. Then several fast pulling

curves are acquired to verify that conditions are favorable to proceed, and for a reference to assist in determining which side of the patch is exposed. The typical protocol for pulling experiments is to press the tip into the surface at ∼1 nN, wait ∼1 s for a protein to nonspecifically bind, then pull back at a moderate rate (∼100-200 nm/s) and determine whether a molecule is attached by the presence of specific force peaks. When conditions are good and the patch is oriented with the C-terminus exposed, this sticking occurs ∼1% of the time. Once a molecule is detected, more specific protocols are applied. We have applied two protocols in particular to BR. Slow (<2 nm/s) refolding and unfolding was used to probe refolding and find interesting regions of the protein, and extension clamping was used to observe transitions over longer periods of time.

7.3 Unfolding and refolding at and near equilibrium

We observed hopping back and forth over a barrier when pulling at 2 nm/s. Figure 7.2 shows an example of this. The protocol here was to press into the surface at 1 nN, wait 1 s, then pull back at 80 nm/s. When an event (the first force peak) was detected, the pulling rate was switched to 2 nm/s. At around 20 nm, the protein unfolds and refolds several times before the tip is moved out of the range where this occurs. This type of behavior happens frequently, but not always, during slow pulling curves. The high precision and slow speed are critical to resolve it, since the entire event happens within a tip position of 1 nm and 0.4 s. If the tip were moving faster, it would skip over these events. The key challenge in interpreting this data is to determine what part of the protein is involved in this data trace. As described below, we were unsure of the sidedness and placement of the protein on the curve.

When we clamped at positions where back-and-forth hopping was observed in the slow pulling, we observed hopping between several states. During the trace shown in Figure 7.3, the tip was moved by 0.5 nm increments during extension clamping. In Figure 7.3, a, however, force drift can clearly be seen. These data were acquired before the force stability described in Chapter 6— indeed, this was one of the traces that demonstrated that the force drift was a major limiting factor in our ability to perform the experiments we desired to perform. Therefore, quantitative interpretation of

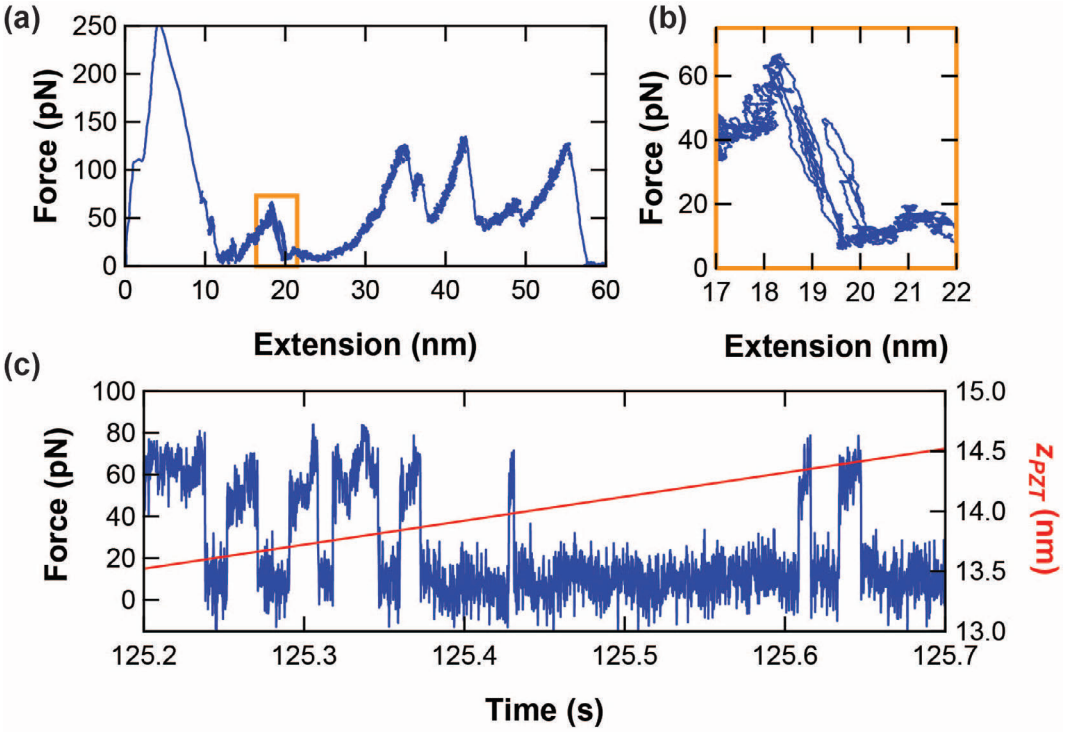

Figure 7.2: Hopping back and forth over a barrier observed during slow pulling of bacteriorhodopsin. (a) Force versus extension curve on bacteriorhodopsin, smoothed to 50 Hz. Before ∼10 nm, the tip position was ramped at 80 nm/s. Once an event was detected, the rate was slowed to 2 nm/s. (b) Expanded view of the region in the orange box shows that this peak has multiple events, not just one unfolding. (c) Plotting full bandwidth data as a function of time, rather than extension, allows the events to be seen more clearly. The requested position of the tip at this time is shown in red; the entire series of events happens in less than 1 nm.

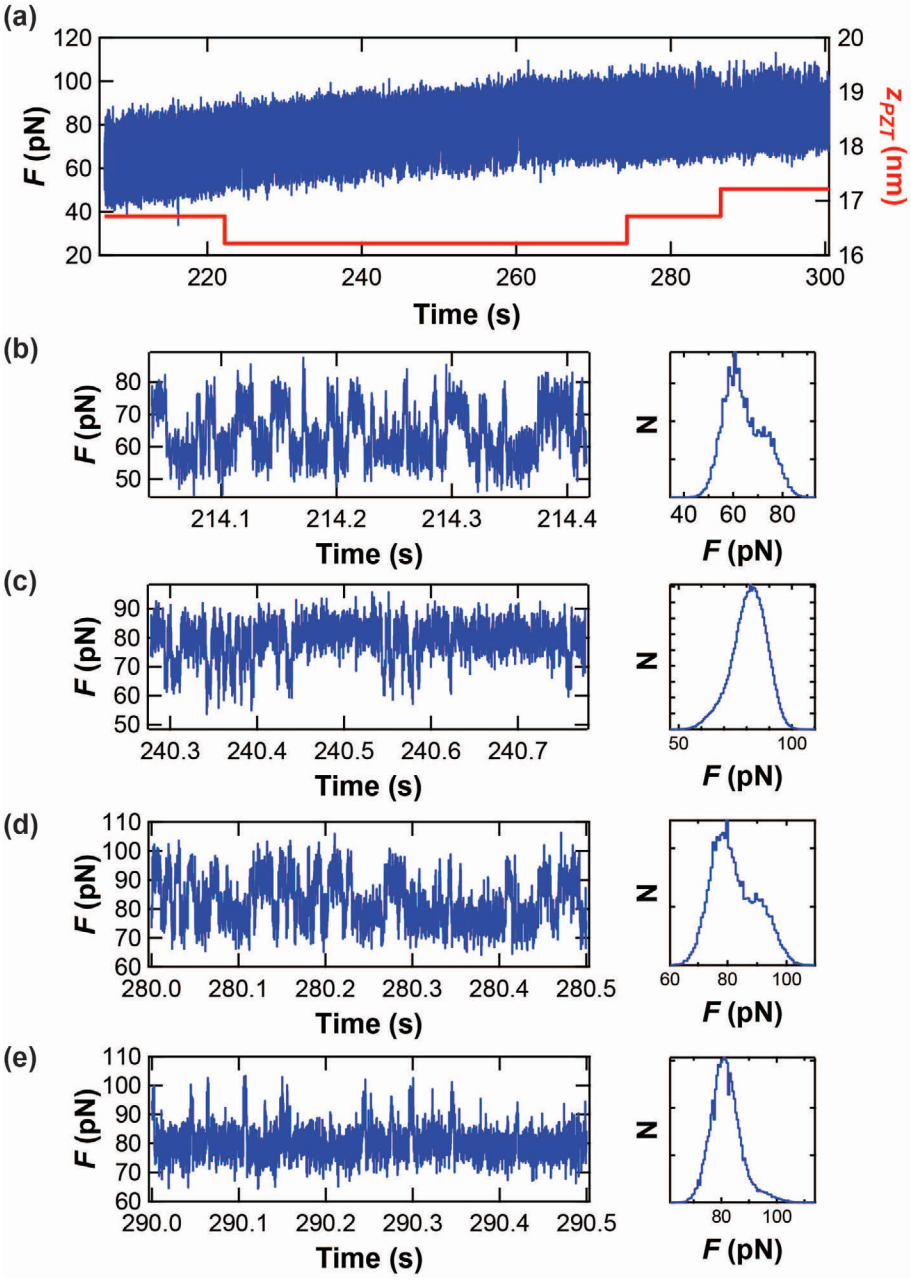

Figure 7.3: Hopping back and forth over a barrier observed during extension clamping of bacteriorhodopsin. (a) Entire extension clamping section of the record, with force in dark blue and requested tip position in red. The position was clamped at 16.7 nm, then 16.2 nm, moved back to 16.7 nm and finally clamped at 17.2 nm. (b)-(e) Detail time records and histograms during extension clamping at 16.7, 16.2, 16.7, and 17.2 nm, respectively. Note that the time traces show a small part of the data used to create the histogram, and that the forces shown are not corrected for drift.

these data are not possible. It is still interesting to qualitatively observe them, however. Figures 7.3, b through e, show how the time spent in each state varies as a function of extension. In panel (b), the state is relatively evenly distributed between the two states. Panel (c), 0.5 nm closer to the surface, shows a clear bias to the higher force (folded) state. Panel (d), which returns to the same extension in panel (a), has a similar distribution. Interestingly, this implies that a significant amount of the force drift in this case was a measurement artifact, since a similar distribution is occurring at different measured force. Although this is one of the traces that motivated us to look for the force drift described in Chapter 6, it is possible that this time the drift was due to a different effect that was also uncovered in that process. Namely, the voltage references take a very long time (hours) to warm up, and drift can be reduced by leaving them on. Finally, in Panel (e), the extension is clamped 0.5 nm further from the surface, and the distribution is biased to the low force (unfolded) state.

The first barrier to quality interpretation of BR data is determining the sidedness of the membrane. It can land with either the C-terminal (cytoplasmic) or N-terminal (extracellular) side facing up. We have used the low pH procedure to bias the membrane to landing with the C-terminal side up. The C-terminal side has a much greater chance of sticking to the tip than the N-terminal side, which other groups have found to stick only one in every ∼10,000 times (private communication with Max Kessler). When conditions are good, the C terminus sticks to the tip ∼1% of the time. The most definitive way to determine sidedness is through high-resolution imaging, high enough resolution to observe the shape of the trimer. However, this is currently not possible in the ultrastable AFM, as we currently use only glass substrates, which are too rough for molecular resolution imaging. Another way to determine sidedness is to check that high-speed pulls align to the shape of reported pulling curves from the literature. The height and presence or absence of larger bumps can also be used as low-resolution imaging ways to determine sidedness. These bumps, which appear more often on the cytoplasmic side, are thought to be molecules of F1-ATPase.

A second barrier to quantitative analysis of these data is understanding what part of the protein is being unfolded and refolded. In typical AFM pulling experiments this is done by lining

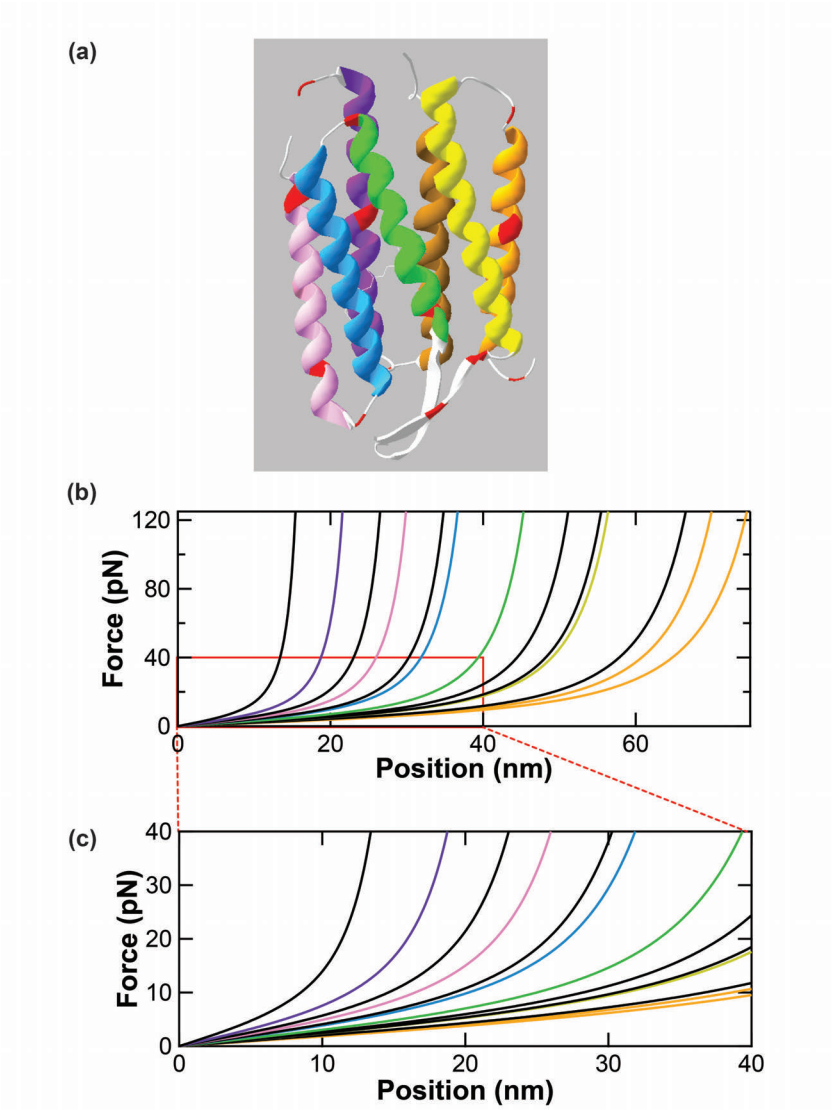

Figure 7.4: Previously-observed anchor points in bacteriorhodopsin. (a) Ribbon diagram created from PDB file 2NTU [119]. Helices A-F are colored, in order, orange, yellow, green, blue, purple, and brown. Note that the break in the chain between helices E and F is a feature of the structure, not of the protein itself. Transitions observed in Reference [117] when pulling from the C terminus are colored red. (b) The same transitions drawn on a force versus extension graph as wormlike chain curves, color coded according to helix. Transitions colored in black are in between helices. (c) Expanded view of the same plot. Note how crowded the transitions are at low force.

the traces up by eye. This is complicated by the fact that the attachment point of the protein to the tip is unknown— it could be bound anywhere along the C- or N-terminus and anywhere along the side of the AFM tip. Additionally, slow traces are more difficult to fit to wormlike chain curves than fast ones. Since the higher forces are not sampled during a slow pulling event, the curves corresponding to different attachment points are much more similar. Naively you would expect to simply plot force as a function of extension and each point would fit to a particular point on a wormlike chain curve. In practice they are very close together, especially at low force (Figure 7.4), so that any one point could be interpreted as belonging on many different curves. Complicating matters is the fact that z_0 and F_0, the position and force of zero, are not well known. The standard in the field is to line these up by eye. Many different anchor points have been reported in the literature, so we cannot rely on reported values to distinguish between two nearby possibilities. Contrast this to a more simple system, two-state unfolding of a small soluble protein with no or one reported intermediate. In that case, less precision and accuracy are required, because there are fewer states that the system is likely to be in.

Several papers have been published [15, 116, 117, 79] describing the anchor points in BR at which force peaks are observed. The anchor points observed are similar, but not the same, between the different reports. Only one [117] reports an uncertainty in assigning the peaks to amino acids in BR, and that uncertainty is relatively large: $\pm$ 3 amino acids. The transitions observed in that paper when pulling from the C-terminal side are shown in Figure 7.4 mapped onto a crystal structure of BR and drawn as wormlike chain force-versus-extension curves. Unsurprisingly, several of the observed anchor points are at the ends of the helices, but anchor points are also observed mid-helix for many of the helices. This creates a large number of curves that are relatively closely spaced, especially at low force, making them hard to distinguish. We solved this problem by significantly improving the force precision (Chapter 6), but have not yet applied that work to BR.

7.4 Conclusions and future directions

The folding pathways of Bacteriorhodopsin are complex, and can be probed by near-equilibrium AFM measurements. However, in order to make quantitative evaluations of equilibrium folding behavior, more work is required. First, these experiments must be revisited with the uncoated, low drift AFM cantilevers described in Chapter 6. Greater force stability will assist in determining the region of the protein where the events are taking place, and also in measuring kinetics. Second, the experiments should be revisited with a covalent attachment between the AFM tip and the protein. The duration of experiments is ultimately limited by the longevity of this attachment. Events where a protein attached to the tip, then released before the end of the experiment, were extremely common during the data collection process. The Perkins lab is currently working to produce cysteine-labeled BR, in an effort led by Violet Roskens, and using *H. salinarum* colonies kindly provided by James Bowie. These BR mutants could be covalently attached to functionalized tips as described in Reference [120]. The optical imaging technique described in Chapter 4 will be key to this effort, since it will prevent the tip being contaminated before use. These improvements will increase the duration of equilibrium folding and unfolding events, and the consistency with which we can acquire these data.

Chapter 8

Equilibrium fluctuations of the computationally-designed soluble protein NuG2

8.1 Introduction

It is still not fully understood how a protein folds. Although the sequence of a protein can almost always be determined, and the structure can often be determined, how sequence becomes structure is not well understood. One way to better understand protein folding is to take a reductionist approach, attempting to characterize the folding of some small, typical motifs important for folded proteins, then building up to larger sequences from there.

One typical motif is the beta hairpin [121]. These structures involve a hydrogen bond between residues i and $i+3$. Because these interactions are very local, involving amino acids that are close to each other in the sequence, beta hairpins are a logical site for nucleation of folding. Indeed, using mutagenesis and stopped-flow measurements, it has been seen that beta hairpins can be, but are not always, the rate-limiting step for folding of small proteins [121]. An interesting system highlighting the roles of beta hairpins in protein folding comes from the structurally similar immunoglobulin G-binding domains of Protein G and Protein L. Each domain contains two beta hairpins, but opposite hairpins nucleate folding— in the Protein G domain, the second hairpin folds first, while in Protein L the first one folds first. This observation is evidence against the tempting simple hypothesis that proteins with similar structures follow similar folding pathways [122].

Could the folding pathway of the Protein G domain (GB1) be reversed, so that it follows the folding pathway of the Protein L domain? This is the challenge that the David Baker group, a computational lab from the University of Washington, undertook. They showed that this was

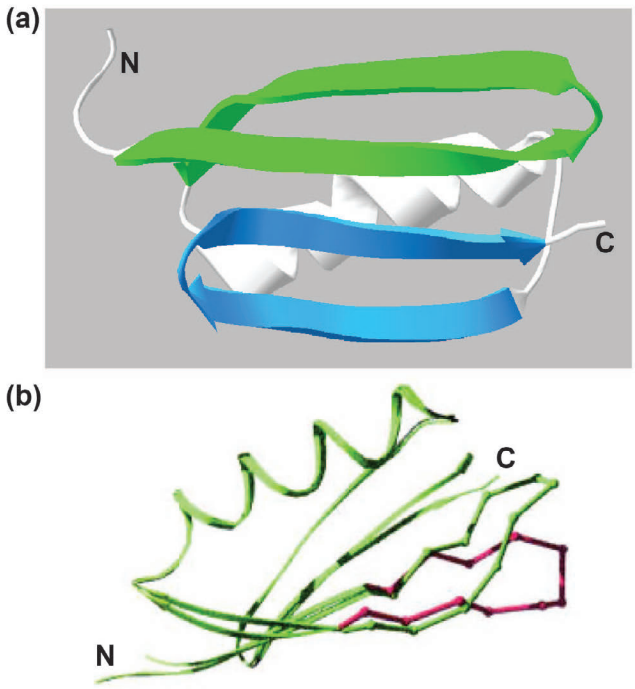

Figure 8.1: The structure of the computationally-designed small folding domain NuG2 (a) Crystal structure from PDB file 1MIO [123]. Hairpin 1 is shown in green and hairpin 2 in blue, with the connecting alpha helix behind in white. (b) Structure from Reference [123] comparing the structures of the first hairpin between the wild type Protein G domain (*green*) and NuG2 (*pink*). Reprinted from [123], with permission from John Wiley and Sons.

indeed possible. By using structures available in the Protein Data Bank, they found hairpins to graft in place of the first (slower-folding) hairpin. Two low-energy turns were selected out of the 322 computationally tested, and two (named NuG1 and NuG2) were expressed and purified. NuG2 was found to be 100x faster-folding and 4 kcal/mol more stable than the wild-type GB1 domain [124]. Later, the group published crystal structures of the proteins, showing that the structures remained very similar to the wild-type protein, and also tested some computer-designed point mutants that increased stability [123]. The structure of NuG2 reported in that paper is shown in Figure 8.1, a. Like the wild-type GB1 domain, NuG2 is a small domain consisting of a beta hairpin followed by an alpha helix, followed by another beta hairpin, aligned so that the 1st and last beta strand are next to each other, forming one sheet. The redesigned first hairpin is oriented slightly differently in NuG2 than in the wild-type GB1 (Figure 8.1, b).

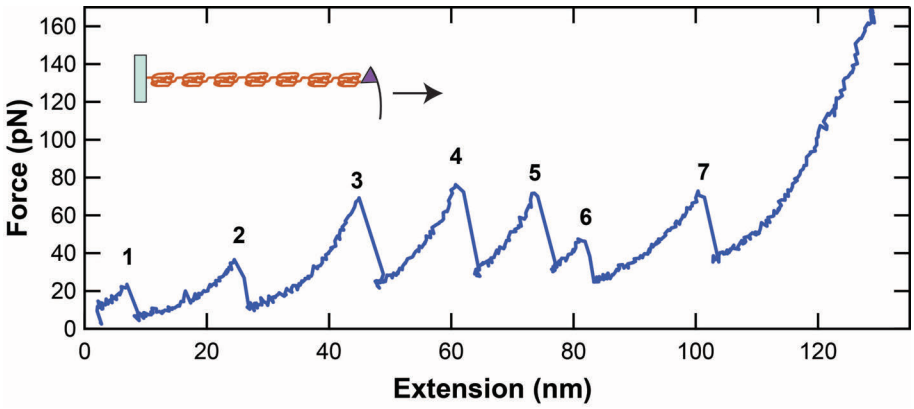

Figure 8.2: Characteristic sawtooth unfolding pattern seen when pulling NuG2 at a constant velocity. Each section represents pulling on a different number of unfolded proteins; force peaks and subsequent force drops occur when a domain unfolds. Here seven NuG2 domains are seen to unfold, followed by a curve that persists to a higher force. This is interpreted as pulling on the fully unfolded protein: the attachments of the protein to the tip and surface sustain a higher force than the folds of each domain.

NuG2 and GB1 have been extensively studied by AFM-based SMFS, spearheaded by Hongbin Li's group at the University of British Columbia. In part these proteins have been studied because of their potential to help understand the initial stages of protein folding; in part, it is for the practical reason that the protein is relatively easy to work with. For AFM studies, these small folding domains

are usually engineered into a string of identical tandem repeats (often 8, as in our construct). This way the presence of the characteristic sawtooth pattern shown in Figure 8.2 can demonstrate that the NuG2 is the protein attached to the tip, and not some other contamination. Further, the high-force section, as seen at the end of that graph, gives evidence as to how many units are attached (in this case, seven). AFM studies on GB1 and NuG2 have shown that their mechanical stability is enhanced by ligand binding [125, 126], that the Markovian nature of the unfolding can be directly measured with force-clamp spectroscopy [19], and that the transition state involves disruption of the bonds between beta strands 1 and 4 [127]. One particularly exciting research direction showed that the tandem repeat polyproteins behave as an ideal elastomer, without fatigue during extension-relaxation cycles [16], and can therefore be used as a building block for designed nanomaterials [128].

We wished to measure the folding properties of NuG2 with our new tools enabled by dual-detection AFM (described in detail in Chapter 5). Specifically, we wished to measure the equilibrium folding kinetics as a function of force. This is in contrast to previous work on NuG2, and most other AFM-based force experiments, which only function out of equilibrium. In this chapter, I discuss the present state of this work. After describing the methods used (8.2), I discuss results from straightforward extension clamping (8.3). We found that the kinetics during the extension clamp were surprisingly slow, leading us to develop a "back-and-forth" protocol to drive folding (8.4). Although a full analysis remained elusive, some preliminary information about the folding transition state can be roughly calculated (8.5). Finally, I conclude with some notes about current challenges and next steps (8.6).

8.2 Methods

We are collaborating on this project with Hongbin Li, who provided tandem repeats of eight NuG2 repeats [$(NuG2)_8$]. These have a cysteine on one end and a histidine tag for purification on the other end. We found that nonspecifically adsorbing the proteins to glass formed bonds that were only rarely long-lasting enough to persist for the duration of our experiments (tens of

minutes). The cysteine in the protein construct can form a covalent bond with a fresh layer of gold, and this was the original technique we used to better immobilize the proteins. However, it was difficult to fabricate a fresh gold surface that was both uniform enough for good adhesion, and thin enough not to affect our laser-based tip position measurements. Gold surfaces were more reactive when used within one hour of removal from the evaporation chamber. We typically used 5-10 nm of gold on the surface, with a 2 nm chromium adhesion layer under it. At this thickness, the protein was usually well-adhered, but the tip signal was degraded. It was still possible to fully calibrate and lock the tip position, but the process was not robust or routine. We therefore switched to the maleimide-based technique reported in Reference [120]. Ruby Sullan in our lab adapted this protocol for anchoring NuG2. Briefly, the surface is functionalized by a silane, then a polyethelene glycol (PEG) linker containing the maleimide is added, followed by the protein. A key part of this technique is the reduction of the disulfide bonds that can form between two polyprotein chains, causing the $(NuG2)_8$ molecules to dimerize. Previously, we would reduce these with Tris (2-carboxyethyl) phosphine hydrochloride (TCEP) or Dithiothreitol (DTT) in the solution. In the maleimide-based protocol, the protein is reduced using TCEP attached to beads, which can then be removed from the protein solution by spinning in a centrifuge and removing the supernatant.

An extension clamp experiment essentially consists of four steps: (*i*) attaching a molecule, (*ii*) confirming that it is a single tether, (*iii*) finding an extension where the protein is hopping between states with different numbers of domains folded, and (*iv*) clamping the tip height near the hopping transition using the FPGA-based servo loop. In order to obtain an attached molecule, the tip is repeatedly pressed onto the surface at $\sim$1 nN for $\sim$1 s, and retracted at $\sim$200 nm/s. Exact values of these parameters are adjusted on a day-to-day basis to optimize attachment. Most retraction curves will not have attached molecules. In order to select those that do, the program uses extension and force thresholds set by the user with a cursor on the live force-versus-extension plot. If the measured force and extension both reach values above threshold values, the software recognizes this as an attached molecule. Typical threshold values for the $(NuG2)_8$ construct are 80 nm for the extension and 90 pN for the force. Once the molecule is attached, the program moves

most of the way back to the surface, locks the position, and gives extension control to the user via a video game controller. The video game controller can be used to move the extension up and down, as well as to control the most important features of the user interface (e.g., moving cursors on the graph, clearing the graph, and initiating different sets of instructions). Tether confirmation is accomplished using this control. The user moves the tether up and down at a relatively fast rate (∼50 nm/s), visually verifying that it has the features of a single tether, and confirming the number of molecules attached. Then the extension is changed more slowly (∼5 nm/s) to find an extension where hopping behavior occurs. Finally, the extension is clamped for ∼100 s at several extensions near this hopping point to record the long-term data traces. For the back-and-forth protocol, the procedure is nearly identical. The only difference is that, instead of clamping at a single position in the last step, the extension is stepped between two positions: one just above and one just below the extension at which the molecule spends half of the time in each state. The user defines these positions by placing cursors on the graph. Data is collected at several such pairs.

8.3 Extension clamping on NuG2

In principle, extension clamping is a valuable technique because it can provide equilibrium information about the folding and unfolding rates at different extensions, and therefore different forces [129]. If sufficiently long traces can be acquired, data from many unfolding and refolding events can be analyzed at once, leading to a more precise result. Unexpectedly, NuG2 did not unfold and fold fast enough during an extension clamp to make this type of analysis. Figure 8.3 shows one such trace. The approximate drift rate during this extension clamp is 0.2 nm/minute, about half that of the average uncoated BioLever during the force drift experiments described in Chapter 6. Despite that, the force drifted significantly before enough events were observed to calculate folding and unfolding rates. In order to generate more events in less time, we switched to the more complicated "back-and-forth" protocol described in the next section.

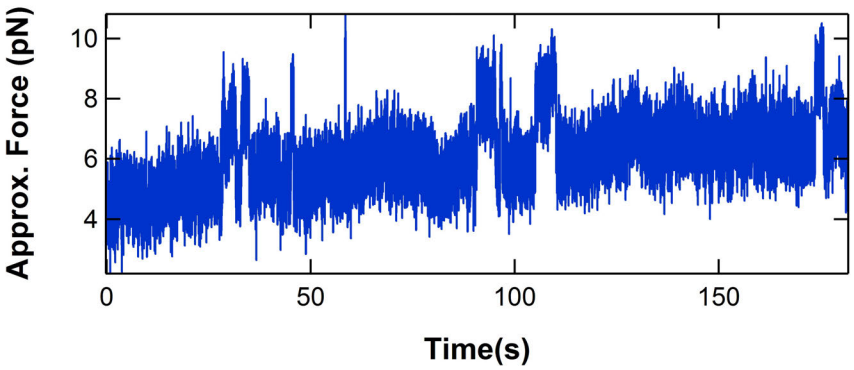

Figure 8.3: Force trace during clamping at a single extension on NuG2. Although an uncoated cantilever was used to minimize drift, there was still significant drift over the 200 seconds of data acquisition. Furthermore, there were not enough folding and unfolding events in that time to calculate overall rates.

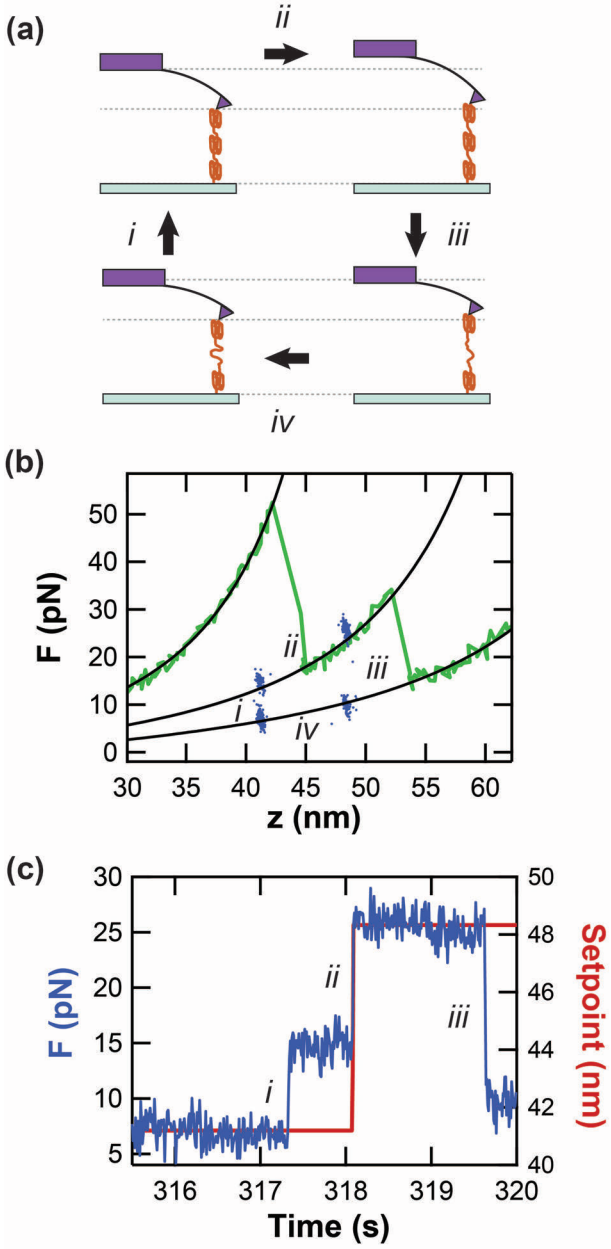

Figure 8.4: The "back and forth" protocol on NuG2. (a) Schematic showing the four steps of the experiment. Note that three sub-units are shown for simplicity in the illustration; the actual experiment used eight. (*i*) The extension clamp starts in a position where the folded state is favored, and a module of the protein folds. Although the molecule was drawn with all modules folded at this point, that may or may not be the case. (*ii*) The tip is then moved to a position where the unfolded state is favored. (*iii*) The molecule unfolds. (*iv*)The molecule is then relaxed back to the starting extension, where the folded state is favored. Note that it need not be the same module that unfolded in step ii. (b) Force-versus extension plot showing the path of the molecule through the theoretical wormlike-chain curves (*black*). Note that a change in extension represents movement along a wormlike-chain curve, while unfolding and refolding represent jumps between them. (c) The same data plotted against time (*blue*), along with the extension set point (*red*).

8.4 Back-and-forth measurements on NuG2

In the back-and-forth protocol, two extensions were chosen, with one biased toward the folded state and one biased toward the unfolded state. The tip position was then alternated between them by hand, with the user switching the extension after observing a folding or unfolding event (Figure 8.4). This procedure produced events much more quickly than extension clamping: ∼50 events in 100 seconds, as compared to the ∼5 events in 100 seconds seen in Figure 8.3. With this larger amount of data, folding and unfolding rates can be determined from the dwell time histograms of the events. The most simple expected behavior is for the folding rate to decrease and the unfolding rate to increase as the force increases. However, when plotted against force, there is too much scatter in the data to discern a clear trend.

8.5 Estimate of distance to folding transition state

Although the data as they currently stand have too many complicating factors for a full analysis, it is still possible to derive an estimate of the distance to the transition state Δx. The folding or unfolding rate at a particular force F is given by [19]:

$$\alpha(F) = \alpha_0 \exp(\frac{F\Delta x}{k_b T}), \tag{8.1}$$

where α_0 is the folding or unfolding rate at zero force, Δx is the distance to the transition state, and $k_b T$ is the thermal energy. So

$$\Delta x = \frac{k_b T}{F} \ln(\frac{\alpha}{\alpha_0}). \tag{8.2}$$

The zero-force folding rate of NuG2 was found by bulk measurements to be 1100 s^{-1} [124]. Using this value in one set of back-and-forth type measurements, Δx for folding was calculated to be 5 ± 2 nm (number of rates measured N=8). To put this number in context, folded NuG2 as seen in the crystal structure [123] is only 3-4 nm across. A large distance to the transition state on the mechanical folding energy landscape might account for the slow dynamics during extension

clamping (*e.g.*, Figure 8.3) even though the unloaded folding rate is very fast. The Δx for folding is also comparable to that measured for prion proteins [130]. The reported α_0 for unfolding is about 0.03 s^{-1} [19]. Calculations of Δx from the same set of back-and-forth data using this value yielded 0.4 ± 0.2 nm (N=10), within error of the reported value of 0.25 ± 0.01 nm, determined by force-clamp spectroscopy [19].

8.6 Conclusions and future directions

In the pursuit of precision AFM force measurements, each problem solved reveals the next obstacle. Having reduced position drift, force drift became relevant; having reduced the force drift, a number of smaller obstacles now stand in the way of a complete characterization. First, the reduced force drift is still significant at the long time scales we are concerned with. We have found that allowing the instrument to settle for a very long time (several hours) before taking data reduces but does not eliminate this issue. Force drift affects not only the baseline of a single rate measurement during an extension clamp or back-and-forth experiment (100s of seconds), but also complicates interpretation by making it difficult to determine the zero-force position, and therefore the absolute force. So far, I have attempted to solve this problem by recording relatively fast pulling traces in between rate measurements, then fitting these to wormlike-chain curves with the zero-force position as a free parameter. However, this technique has had little success, as the fits obtained were not very repeatable, and highly dependent on the initial conditions. In the future, I plan to touch the surface in between rate measurements to obtain an unequivocal measurement of the zero-force position. This touchoff event must be fast (a few ms) and gentle, to avoid contaminating the tip. The code controlling this event was therefore written onto the FPGA. The code has been written and tested, but not yet implemented during an NuG2 experiment. A second potential source for analysis trouble could be subunits unfolding and refolding at very low force below the instrumental noise. Since the force is so low, the force differences between some subunits are very small, and we may be missing folding and unfolding events. For instance, we may be attempting to study the transition between a state with five unfolded domains and one with six unfolded domains,

but making undetected transitions to a state with seven unfolded domains. This is particularly a problem for the folding events, since they occur at lower force, and I speculate that it is a major source of the greater error in calculating the distance to the folding transition state versus the unfolding. The simplest way to avoid this is to operate near the end of the protein, where there are no such "extra" domains to unfold. This carries the negatives of slower net folding and unfolding rates, a greater potential for the protein to detach from the tip, and operation near the edge of the tip's position-calibrated region. Another possible solution would be to make a protein construct in which one domain of NuG2 is situated in between repeats of a domain with a higher unfolding force, for instance the I27 domain of Titin. Finally, in order to make the most compelling statements, precision must go hand-in-hand with accuracy. Currently, force accuracy in AFM is limited by the thermal calibration of the tip spring constant, which can vary by up to 15% [131]. Since we expect the proteins to be sensitive to sub-pN force differences, this is significant on the scale of forces we measure: 15% of 4 pN is 0.6 pN. Our best way to work around this problem for now is to compare only data from the same tip. Then we know that we are at least comparing forces measured the same way, even if the absolute numbers are inaccurate. Ultimately, to achieve quantitative data that can be accurately compared with results from other labs and other techniques, we must use a more accurate method of spring constant determination. It may be possible to use the overstretching transition of DNA as an *in-situ* force calibration.

Despite these many difficulties, it is also possible that the unexpected apparent behavior of the folding and unfolding as a function of force represents real effects. It has been theorized that these rates might have unexpected behavior as a function of force, stemming from the choice of 1D reaction coordinate in the many-dimensional folding landscape that even a simple protein possesses [132]. The reaction coordinate in a mechanical unfolding experiment is the end-to-end distance, but this may not correspond to the degree of freedom that is the rate-limiting step. If this is the case, a number of scenarios of force dependence of the folding and unfolding lifetimes are possible, including scenarios where the unfolding rate, for instance, decreases rather than increases at higher force, or scenarios where there the rate is a function of force is non-monotonic. The refolding of

NuG2 has not been extensively studied; it is possible that it falls into one of these categories.

Chapter 9

Conclusions and Future Directions

In summary, we have opened up new ways of doing AFM by measuring the tip and sample positions with two focused laser beams. The instrument relies on a number of hardware and software advances and runs on FPGA-based software. By doing this, we can achieve atomic-scale stability in ambient conditions, imaging with a lateral drift of less than 5 pm/minute. This setup also enables label-free optical imaging of thin (5 nm) biological membranes. Finally, I have optimized this instrument for use in precision single-molecule force spectroscopy to measure protein folding and unfolding. A dual detection mode of both force and position means that we can do pulling more slowly and that we can do extension clamp mode, which was not possible before. When we started trying to apply this to proteins, however, we quickly found out that the force drift was a limiting factor. Fortunately, by simply removing the gold from AFM cantilevers, we could reduce the force drift by greater than an order of magnitude without any decrease in signal-to-noise ratio at the frequencies that we are studying. We apply this to two different protein systems: Bacteriorhodopsin and NuG2. In each case we were able to make qualitative, but not quantitative statements about the proteins. Interpretation is still more complicated than we expected. The NuG2 folded more slowly than we expected. It is harder than expected to differentiate between states at very low force, and it requires precision that we do not have as of yet. However, we were able to observe unfolding and refolding at and near equilibrium for both systems.

Looking forward, the ultrastable AFM project will take a number of directions. It has a number of potential abilities that have not yet been fully exploited. Because the ultrastable AFM

excels at imaging slowly, it is well-suited for use in jumping (also known as force-volume) mode [133, 134], where the tip is lowered to a user-defined force at each pixel. This is a very gentle but also slow mode of imaging. We have programmed the ultrastable AFM to perform this mode of imaging, and hope to use it on large, fragile samples such as virus capsids and microtubules. A second capacity we hope to exploit is the ability to hover the tip over a quickly-changing biological system and monitor its fluctuations. Finally, the second-generation instrument is currently in the planning phases. It will include features to solve some of the usability challenges that the generation one instrument faces. It will also be more stable and not be based on an optical microscope frame. Also, the soundproof box will be built attached to the floor rather than the optical table.

As a final note, we hope that the technologies and techniques we have developed will be used by others to help achieve their goals in scanning probe microscopy. We are aware of two groups who have applied the ultrastable AFM technique. One group has used a stabilized AFM to measure the growth of neurons [135]. The challenge in this project was to measure growth of cells over minutes to hours at 37 ℃. By stabilizing the AFM, they were able to measure the force exerted by the neuron over tens of minutes. The second group has incorporated stabilization into tip-enhanced Raman scattering (TERS) [136], a scanning probe technique that provides chemical information, allowing them to reduce both the tip-sample drift and the drift between the tip and the excitation beam. Because the technique of measuring the tip and sample positions with backscattered light is very general, we expect that it will be incorporated into more types of scanning probe techniques, increasing the precision and duration with which data can be acquired.

Bibliography

[1] Leo Gross, Fabian Mohn, Nikolaj Moll, Peter Liljeroth, and Gerhard Meyer. The chemical structure of a molecule resolved by atomic force microscopy. Science, 325(5944):1110–1114, 2009.

[2] Leo Gross, Fabian Mohn, Nikolaj Moll, Gerhard Meyer, Rainer Ebel, Wael M Abdel-Mageed, and Marcel Jaspars. Organic structure determination using atomic-resolution scanning probe microscopy. Nature Chemistry, 2(10):821–825, 2010.

[3] Nikolay Buzhynskyy, Richard K Hite, Thomas Walz, and Simon Scheuring. The supramolecular architecture of junctional microdomains in native lens membranes. EMBO Reports, 8(1):51–55, 2006.

[4] Simon Scheuring, Nikolay Buzhynskyy, Szymon Jaroslawski, Rui Pedro Gonçalves, Richard K Hite, and Thomas Walz. Structural models of the supramolecular organization of aqp0 and connexons in junctional microdomains. Journal of Structural Biology, 160(3):385–394, 2007.

[5] Simon Scheuring and James N Sturgis. Chromatic adaptation of photosynthetic membranes. Science Signalling, 309(5733):484, 2005.

[6] Etienne Dague, David Alsteens, Jean-Paul Latgé, Claire Verbelen, Dominique Raze, Alain R Baulard, and Yves F Dufrêne. Chemical force microscopy of single live cells. Nano Letters, 7(10):3026–3030, 2007.

[7] M. Shibata, T. Uchihashi, H. Yamashita, H. Kandori, and T. Ando. Structural changes in bacteriorhodopsin in response to alternate illumination observed by high-speed atomic force microscopy. Angewandte Chemie, 123(19):4502–4505, 2011.

[8] Richard D Piner, Jin Zhu, Feng Xu, Seunghun Hong, and Chad A Mirkin. Dip-pen nanolithography. Science, 283(5402):661–663, 1999.

[9] SK Kufer, EM Puchner, H Gumpp, T Liedl, and HE Gaub. Single-molecule cut-and-paste surface assembly. Science, 319(5863):594–596, 2008.

[10] Gerd Binnig, Calvin F Quate, and Ch Gerber. Atomic force microscope. Physical Review Letters, 56(9):930–933, 1986.

[11] Gerhard Meyer and Nabil M Amer. Novel optical approach to atomic force microscopy. Applied Physics Letters, 53(12):1045–1047, 1988.

[12] Ken A Dill and Justin L MacCallum. The protein-folding problem, 50 years on. Science, 338(6110):1042–1046, 2012.

[13] Nobuyasu Koga, Rie Tatsumi-Koga, Gaohua Liu, Rong Xiao, Thomas B Acton, Gaetano T Montelione, and David Baker. Principles for designing ideal protein structures. Nature, 491(7423):222–227, 2012.

[14] Matthias Rief, Mathias Gautel, Filipp Oesterhelt, Julio M Fernandez, and Hermann E Gaub. Reversible unfolding of individual titin immunoglobulin domains by afm. Science, 276(5315):1109–1112, 1997.

[15] F. Oesterhelt, D. Oesterhelt, M. Pfeiffer, A. Engel, HE Gaub, and DJ Müller. Unfolding pathways of individual bacteriorhodopsins. Science, 288(5463):143–146, 2000.

[16] Yi Cao and Hongbin Li. Polyprotein of gb1 is an ideal artificial elastomeric protein. Nature Materials, 6(2):109–114, 2007.

[17] R. Merkel, P. Nassoy, A. Leung, K. Ritchie, and E. Evans. Energy landscapes of receptor–ligand bonds explored with dynamic force spectroscopy. Nature, 397(6714):50–53, 1999.

[18] J.M. Fernandez and H. Li. Force-clamp spectroscopy monitors the folding trajectory of a single protein. Science, 303(5664):1674–1678, 2004.

[19] Yi Cao, Rachel Kuske, and Hongbin Li. Direct observation of markovian behavior of the mechanical unfolding of individual proteins. Biophysical Journal, 95(2):782–788, 2008.

[20] N. Liu, T. Bu, Y. Song, W. Zhang, J. Li, W. Zhang, J. Shen, and H. Li. The nature of the force-induced conformation transition of dsdna studied by using single molecule force spectroscopy. Langmuir, 26(12):9491–9496, 2010.

[21] I. Casuso and S. Scheuring. Automated setpoint adjustment for biological contact mode atomic force microscopy imaging. Nanotechnology, 21(3):035104, 2009.

[22] J.P. Junker, F. Ziegler, and M. Rief. Ligand-dependent equilibrium fluctuations of single calmodulin molecules. Science Signalling, 323(5914):633, 2009.

[23] J. Stigler, F. Ziegler, A. Gieseke, J.C.M. Gebhardt, and M. Rief. The complex folding network of single calmodulin molecules. Science Signalling, 334(6055):512, 2011.

[24] Masayuki Abe, Yoshiaki Sugimoto, Takashi Namikawa, Kenichi Morita, Noriaki Oyabu, and Seizo Morita. Drift-compensated data acquisition performed at room temperature with frequency modulation atomic force microscopy. Applied Physics Letters, 90(20):203103–203103, 2007.

[25] DW Pohl and R Moller. Tracking tunneling microscopy. Review of Scientific Instruments, 59(6):840–842, 1988.

[26] Neil H Thomson, Monika Fritz, Manfred Radmacher, Jason P Cleveland, Christoph F Schmidt, and Paul K Hansma. Protein tracking and detection of protein motion using atomic force microscopy. Biophysical Journal, 70(5):2421–2431, 1996.

[27] Babak Mokaberi and Aristides AG Requicha. Drift compensation for automatic nanomanipulation with scanning probe microscopes. Automation Science and Engineering, IEEE Transactions on, 3(3):199–207, 2006.

[28] Toshio Ando, Noriyuki Kodera, Eisuke Takai, Daisuke Maruyama, Kiwamu Saito, and Akitoshi Toda. A high-speed atomic force microscope for studying biological macromolecules. Proceedings of the National Academy of Sciences, 98(22):12468–12472, 2001.

[29] Toshio Ando, Takayuki Uchiashi, and Noriyuki Kodera. High-speed afm and applications to biomolecular systems. Annual Review of Biophysics, 42(1), 2013.

[30] Roger Proksch and E Dan Dahlberg. Optically stabilized, constant-height mode operation of a magnetic force microscope. Journal of Applied Physics, 73(10):5808–5810, 1993.

[31] AW Sparks and SR Manalis. Scanning probe microscopy with inherent disturbance suppression. Applied Physics Letters, 85(17):3929–3931, 2004.

[32] Euclid E Moon and Henry I Smith. Nanometer-precision pattern registration for scanning-probe lithographies using interferometric-spatial-phase imaging. Journal of Vacuum Science & Technology B: Microelectronics and Nanometer Structures, 24(6):3083–3087, 2006.

[33] Euclid E Moon, Jan Kupec, Mark K Mondol, Henry I Smith, and Karl K Berggren. Atomic-force lithography with interferometric tip-to-substrate position metrology. Journal of Vacuum Science & Technology B: Microelectronics and Nanometer Structures, 25(6):2284–2287, 2007.

[34] M. Schlierf, F. Berkemeier, and M. Rief. Direct observation of active protein folding using lock-in force spectroscopy. Biophysical Journal, 93(11):3989–3998, 2007.

[35] G.M. King, A.R. Carter, A.B. Churnside, L.S. Eberle, and T.T. Perkins. Ultrastable atomic force microscopy: atomic-scale stability and registration in ambient conditions. Nano Letters, 9(4):1451, 2009.

[36] A.B. Churnside, R.M.A. Sullan, D.M. Nguyen, S.O. Case, M.S. Bull, G.M. King, and T.T. Perkins. Routine and timely sub-piconewton force stability and precision for biological applications of atomic force microscopy. Nano Letters, 12(7):3557–3561, 2012.

[37] A.R. Carter. A precision optical trapping assay: measuring the conformational dynamics of single e. coli RecBCD helicases. PhD thesis.

[38] A.B. Churnside, G.M. King, A.R. Carter, and T.T. Perkins. Improved performance of an ultrastable measurement platform using a field-programmable gate array for real-time deterministic control. In Proc. SPIE, volume 7042, page 704205, 2008.

[39] V. Jacobsen, P. Stoller, C. Brunner, V. Vogel, and V. Sandoghdar. Interferometric optical detection and tracking of very small gold nanoparticles at a water-glass interface. Optics Express, 14(1):405–414, 2006.

[40] H. Ewers, V. Jacobsen, E. Klotzsch, A.E. Smith, A. Helenius, and V. Sandoghdar. Label-free optical detection and tracking of single virions bound to their receptors in supported membrane bilayers. Nano Letters, 7(8):2263–2266, 2007.

[41] A.B. Churnside, G.M. King, and T.T. Perkins. Label-free optical imaging of membrane patches for atomic force microscopy. Optics Express, 18(23):23924–23932, 2010.

[42] A.B. Churnside, G.M. Kinga, and T.T. Perkins. Independent measurements of force and position in atomic force microscopy. In Proc. of SPIE Vol, volume 7405, pages 74050H–1, 2009.

[43] W.J. Greenleaf, M.T. Woodside, and S.M. Block. High-resolution, single-molecule measurements of biomolecular motion. Annual Review of Biophysics and Biomolecular Structure, 36:171, 2007.

[44] A.R. Carter, G.M. King, T.A. Ulrich, W. Halsey, D. Alchenberger, and T.T. Perkins. Stabilization of an optical microscope to 0.1 nm in three dimensions. Applied Optics, 46(3):421–427, 2007.

[45] A.R. Carter, G.M. King, and T.T. Perkins. Back-scattered detection provides atomic-scale localization precision, stability, and registration in 3d. Optics Express, 15(20):13434–13445, 2007.

[46] A.E. Carpenter. Human TATA-Binding Protein Interactions with DNA Characterized by Stabilized, Axial Optical Trapping. PhD thesis.

[47] M.J. Lang, C.L. Asbury, J.W. Shaevitz, and S.M. Block. An automated two-dimensional optical force clamp for single molecule studies. Biophysical Journal, 83(1):491–501, 2002.

[48] IM Svishchev and PG Kusalik. Structure in liquid water: A study of spatial distribution functions. The Journal of Chemical Physics, 99:3049, 1993.

[49] T.T. Perkins, R.V. Dalal, P.G. Mitsis, and S.M. Block. Sequence-dependent pausing of single lambda exonuclease molecules. Science, 301(5641):1914–1918, 2003.

[50] Keir C Neuman and Steven M Block. Optical trapping. Review of Scientific Instruments, 75(9):2787–2809, 2004.

[51] DA Walters, JP Cleveland, NH Thomson, PK Hansma, MA Wendman, Gus Gurley, and Virgil Elings. Short cantilevers for atomic force microscopy. Review of Scientific Instruments, 67(10):3583–3590, 1996.

[52] J. Vesenka, S. Manne, R. Giberson, T. Marsh, and E. Henderson. Colloidal gold particles as an incompressible atomic force microscope imaging standard for assessing the compressibility of biomolecules. Biophysical Journal, 65(3):992–997, 1993.

[53] J. Gelles, B.J. Schnapp, and M.P. Sheetz. Tracking kinesin-driven movements with nanometre-scale precision. Nature, 331(6155):450–453, 1988.

[54] W.K. Pratt. Digital Image Processing, volume 4. John Wiley & Sons, Hoboken, New Jersey, 2007.

[55] J.L. Choy, S.H. Parekh, O. Chaudhuri, A.P. Liu, C. Bustamante, M.J. Footer, J.A. Theriot, and D.A. Fletcher. Differential force microscope for long time-scale biophysical measurements. Review of Scientific Instruments, 78(4):043711–043711, 2007.

[56] J.T. Woodward and D.K. Schwartz. Removing drift from scanning probe microscope images of periodic samples. Journal of Vacuum Science & Technology B: Microelectronics and Nanometer Structures, 16(1):51–53, 1998.

[57] BC Stipe, MA Rezaei, and W. Ho. Single-molecule vibrational spectroscopy and microscopy. Science, 280(5370):1732–1735, 1998.

[58] J. Huisstede, K. van der Werf, M. Bennink, and V. Subramaniam. Force detection in optical tweezers using backscattered light. Optics Express, 13(4):1113–1123, 2005.

[59] G. Volpe, G. Kozyreff, and D. Petrov. Backscattering position detection for photonic force microscopy. Journal of Applied Physics, 102(8):084701–084701, 2007.

[60] I. Horcas, R. Fernandez, JM Gomez-Rodriguez, J. Colchero, J. Gómez-Herrero, and AM Baro. Wsxm: A software for scanning probe microscopy and a tool for nanotechnology. Review of Scientific Instruments, 78(1):013705–013705, 2007.

[61] T.T. Perkins, G.M. King, and A.R. Carter. Laser guided tip approach with 3d registration to a surface, August 5 2010. US Patent App. 12/806,086.

[62] C.D. Frisbie, L.F. Rozsnyai, A. Noy, M.S. Wrighton, C.M. Lieber, et al. Functional group imaging by chemical force microscopy. Science, pages 2071–2071, 1994.

[63] SM Block, KA Fahrner, and HC Berg. Visualization of bacterial flagella by video-enhanced light microscopy. Journal of Bacteriology, 173(2):933–936, 1991.

[64] R.A. Lugmaier, T. Hugel, M. Benoit, and H.E. Gaub. Phase contrast and dic illumination for afm hybrids. Ultramicroscopy, 104(3):255–260, 2005.

[65] A. Yildiz, J.N. Forkey, S.A. McKinney, T. Ha, Y.E. Goldman, and P.R. Selvin. Myosin v walks hand-over-hand: single fluorophore imaging with 1.5-nm localization. Science, 300(5628):2061–2065, 2003.

[66] H. Yamada, H. Tokumoto, S. Akamine, K. Fukuzawa, and H. Kuwano. Imaging of organic molecular films using a scanning near-field optical microscope combined with an atomic force microscope. Journal of Vacuum Science & Technology B: Microelectronics and Nanometer Structures, 14(2):812–815, 1996.

[67] C.A.J. Putman, H.G. Hansma, H.E. Gaub, and P.K. Hansma. Polymerized lb films imaged with a combined atomic force microscope-fluorescence microscope. Langmuir, 8(12):3014–3019, 1992.

[68] A.B. Mathur, G.A. Truskey, and W. Monty Reichert. Atomic force and total internal reflection fluorescence microscopy for the study of force transmission in endothelial cells. Biophysical Journal, 78(4):1725–1735, 2000.

[69] H. Gumpp, SW Stahl, M. Strackharn, EM Puchner, and HE Gaub. Ultrastable combined atomic force and total internal fluorescence microscope. Review of Scientific Instruments, 80(6):063704–063704, 2009.

[70] R.P. Gonçalves, G. Agnus, P. Sens, C. Houssin, B. Bartenlian, and S. Scheuring. Two-chamber afm: probing membrane proteins separating two aqueous compartments. Nature Methods, 3(12):1007–1012, 2006.

[71] D.J. Müller and A. Engel. Atomic force microscopy and spectroscopy of native membrane proteins. Nature Protocols, 2(9):2191–2197, 2007.

[72] DJ Müller and A. Engel. The height of biomolecules measured with the atomic force microscope depends on electrostatic interactions. Biophysical Journal, 73(3):1633–1644, 1997.

[73] D.J. Griffiths. Introduction to Electrodynamics, volume 3. prentice Hall New Jersey, 1999.

[74] A. Lukács, G. Garab, and E. Papp. Measurement of the optical parameters of purple membrane and plant light-harvesting complex films with optical waveguide lightmode spectroscopy. Biosensors and Bioelectronics, 21(8):1606–1612, 2006.

[75] H. Michel and D. Oesterhelt. Three-dimensional crystals of membrane proteins: bacteriorhodopsin. Proceedings of the National Academy of Sciences, 77(3):1283–1285, 1980.

[76] A. Sarkar, R.B. Robertson, and J.M. Fernandez. Simultaneous atomic force microscope and fluorescence measurements of protein unfolding using a calibrated evanescent wave. Proceedings of the National Academy of Sciences of the United States of America, 101(35):12882–12886, 2004.

[77] A. Beyder, C. Spagnoli, and F. Sachs. Reducing probe dependent drift in atomic force microscope with symmetrically supported torsion levers. Review of scientific instruments, 77(5):056105–056105, 2006.

[78] C. Cecconi, E.A. Shank, C. Bustamante, and S. Marqusee. Direct observation of the three-state folding of a single protein molecule. Science, 309(5743):2057–2060, 2005.

[79] M. Kessler, K.E. Gottschalk, H. Janovjak, D.J. Muller, and H.E. Gaub. Bacteriorhodopsin folds into the membrane against an external force. Journal of Molecular Biology, 357(2):644–654, 2006.

[80] A. Hoffmann and M.T. Woodside. Signal-pair correlation analysis of single-molecule trajectories. Angewandte Chemie International Edition, 50(52):12643–12646, 2011.

[81] C.A. Bippes and D.J. Muller. High-resolution atomic force microscopy and spectroscopy of native membrane proteins. Reports on Progress in Physics, 74(8):086601, 2011.

[82] M. Radmacher, JP Cleveland, and PK Hansma. Improvement of thermally induced bending of cantilevers used for atomic force microscopy. Scanning, 17(2):117–121, 1995.

[83] LA Wenzler, GL Moyes, and TP Beebe. Improvements to atomic force microscopy cantilevers for increased stability. Review of Scientific Instruments, 67(12):4191–4197, 1996.

[84] P. Paolino and L. Bellon. Frequency dependence of viscous and viscoelastic dissipation in coated micro-cantilevers from noise measurement. Nanotechnology, 20(40):405705, 2009.

[85] M. Kawakami, Y. Taniguchi, Y. Hiratsuka, M. Shimoike, and D.A. Smith. Reduction of the damping on an afm cantilever in fluid by the use of micropillars. Langmuir, 26(2):1002–1007, 2009.

[86] G.S. Shekhawat, A. Chand, S. Sharma, V.P. Dravid, et al. High resolution atomic force microscopy imaging of molecular self assembly in liquids using thermal drift corrected cantilevers. Applied Physics Letters, 95(23):233114–233114, 2009.

[87] A. Labuda, J.R. Bates, and P.H. Grütter. The noise of coated cantilevers. Nanotechnology, 23(2):025503, 2011.

[88] A. Noy, D.V. Vezenov, J.F. Kayyem, T.J. Maade, and C.M. Lieber. Stretching and breaking duplex dna by chemical force microscopy. Chemistry & Biology, 4(7):519–527, 1997.

[89] F.A. Denis, P. Hanarp, D.S. Sutherland, J. Gold, C. Mustin, P.G. Rouxhet, and Y.F. Dufrêne. Protein adsorption on model surfaces with controlled nanotopography and chemistry. Langmuir, 18(3):819–828, 2002.

[90] M. Liu, N.A. Amro, C.S. Chow, and G. Liu. Production of nanostructures of dna on surfaces. Nano Letters, 2(8):863–867, 2002.

[91] M.B. Viani, T.E. Schaffer, A. Chand, M. Rief, H.E. Gaub, and P.K. Hansma. Small cantilevers for force spectroscopy of single molecules. Journal of Applied Physics, 86(4):2258–2262, 1999.

[92] C. Bustamante, Z. Bryant, S.B. Smith, et al. Ten years of tension: single-molecule dna mechanics. Nature, pages 423–426, 2003.

[93] M. Rief, H. Clausen-Schaumann, H.E. Gaub, et al. Sequence-dependent mechanics of single dna molecules. Nature Structural Biology, 6:346–350, 1999.

[94] H. Clausen-Schaumann, M. Rief, C. Tolksdorf, and H.E. Gaub. Mechanical stability of single dna molecules. Biophysical Journal, 78(4):1997–2007, 2000.

[95] S.B. Smith, Y. Cui, C. Bustamante, et al. Overstretching b-dna: the elastic response of individual double-stranded and single-stranded dna molecules. Science, pages 795–798, 1996.

[96] P. Cluzel, A. Lebrun, C. Heller, R. Lavery, J.L. Viovy, D. Chatenay, F. Caron, et al. Dna: an extensible molecule. Science, pages 792–794, 1996.

[97] A. Doerr. Membrane protein structures. Nature Methods, 6(1):35–35, 2008.

[98] J. Davey. G-protein-coupled receptors: new approaches to maximise the impact of gpcrs in drug discovery. Expert Opinion on Therapeutic Targets, 8(2):165–170, 2004.

[99] S.H. White. The progress of membrane protein structure determination. Protein Science, 13(7):1948–1949, 2009.

[100] J.U. Bowie. Solving the membrane protein folding problem. Nature, 438(7068):581–589, 2005.

[101] J.L. Popot and D.M. Engelman. Membrane protein folding and oligomerization: the two-stage model. Biochemistry, 29(17):4031–4037, 1990.

[102] Johannes Preiner, Harald Janovjak, Christian Rankl, Helene Knaus, David A Cisneros, Alexej Kedrov, Ferry Kienberger, Daniel J Muller, and Peter Hinterdorfer. Free energy of membrane protein unfolding derived from single-molecule force measurements. Biophysical Journal, 93(3):930–937, 2007.

[103] D. Oesterhelt and W. Stoeckenius. Rhodopsin-like protein from the purple membrane of halobacterium halobium. Nature, 233(39):149–152, 1971.

[104] A. Ventosa and A. Oren. Halobacterium salinarum nom. corrig., a name to replace halobacterium salinarium (elazari-volcani) and to include halobacterium halobium and halobacterium cutirubrum. International Journal of Systematic Bacteriology, 46(1):347–347, 1996.

[105] D. Oesterhelt and W. Stoeckenius. Functions of a new photoreceptor membrane. Proceedings of the National Academy of Sciences, 70(10):2853–2857, 1973.

[106] R. Henderson, J.M. Baldwin, TA Ceska, F. Zemlin, E. Beckmann, KH Downing, et al. Model for the structure of bacteriorhodopsin based on high-resolution electron cryo-microscopy. Journal of Molecular Biology, 213(4):899, 1990.

[107] Eva Pebay-Peyroula, Gabriele Rummel, Jurg P Rosenbusch, and Ehud M Landau. X-ray structure of bacteriorhodopsin at 2.5 angstroms from microcrystals grown in lipidic cubic phases. Science, 277(5332):1676–1681, 1997.

[108] Melody L Mak-Jurkauskas, Vikram S Bajaj, Melissa K Hornstein, Marina Belenky, Robert G Griffin, and Judith Herzfeld. Energy transformations early in the bacteriorhodopsin photocycle revealed by dnp-enhanced solid-state nmr. Proceedings of the National Academy of Sciences, 105(3):883–888, 2008.

[109] H. Yamashita, K. Voïtchovsky, T. Uchihashi, S.A. Contera, J.F. Ryan, and T. Ando. Dynamics of bacteriorhodopsin 2d crystal observed by high-speed atomic force microscopy. Journal of Structural Biology, 167(2):153–158, 2009.

[110] Dmitry M Korzhnev, Vladislav Yu Orekhov, Alexander S Arseniev, Rainer Gratias, and Horst Kessler. Mechanism of the unfolding of transmembrane α-helical segment (1-36)-bacteriorhodopsin studied by molecular dynamics simulations. The Journal of Physical Chemistry B, 103(33):7036–7043, 1999.

[111] Christian Kappel and Helmut Grubmüller. Velocity-dependent mechanical unfolding of bacteriorhodopsin is governed by a dynamic interaction network. Biophysical Journal, 100(4):1109–1119, 2011.

[112] Norbert Hampp, Christoph Bräuchle, and Dieter Oesterhelt. Bacteriorhodopsin wildtype and variant aspartate-96 aspargine as reversible holographic media. Biophysical Journal, 58(1):83–93, 1990.

[113] Y.K. Reshetnyak, O.A. Andreev, M. Segala, V.S. Markin, and D.M. Engelman. Energetics of peptide (phlip) binding to and folding across a lipid bilayer membrane. Proceedings of the National Academy of Sciences, 105(40):15340–15345, 2008.

[114] H.J. Butt, K.H. Downing, and P.K. Hansma. Imaging the membrane protein bacteriorhodopsin with the atomic force microscope. Biophysical Journal, 58(6):1473, 1990.

[115] D.J. Müller, G. Büldt, A. Engel, et al. Force-induced conformational change of bacteriorhodopsin. Journal of Molecular Biology, 249(2):239–243, 1995.

[116] H. Janovjak, J. Struckmeier, M. Hubain, A. Kedrov, M. Kessler, and D.J. Müller. Probing the energy landscape of the membrane protein bacteriorhodopsin. Structure, 12(5):871–879, 2004.

[117] M. Kessler and H.E. Gaub. Unfolding barriers in bacteriorhodopsin probed from the cytoplasmic and the extracellular side by afm. Structure, 14(3):521–527, 2006.

[118] Steven B Hayward, David A Grano, Robert M Glaeser, and Knute A Fisher. Molecular orientation of bacteriorhodopsin within the purple membrane of halobacterium halobium. Proceedings of the National Academy of Sciences, 75(9):4320–4324, 1978.

[119] J.K. Lanyi and B. Schobert. Structural changes in the l photointermediate of bacteriorhodopsin. Journal of Molecular Biology, 365(5):1379–1392, 2007.

[120] J.L. Zimmermann, T. Nicolaus, G. Neuert, and K. Blank. Thiol-based, site-specific and covalent immobilization of biomolecules for single-molecule experiments. Nature Protocols, 5(6):975–985, 2010.

[121] Anna Marie C Marcelino and Lila M Gierasch. Roles of β-turns in protein folding: From peptide models to protein engineering. Biopolymers, 89(5):380–391, 2008.

[122] Arash Zarrine-Afsar, Stefan M Larson, and Alan R Davidson. The family feud: do proteins with similar structures fold via the same pathway? Current Opinion in Structural Biology, 15(1):42–49, 2005.

[123] Sehat Nauli, Brian Kuhlman, Isolde Le Trong, Ronald E Stenkamp, David Teller, and David Baker. Crystal structures and increased stabilization of the protein g variants with switched folding pathways nug1 and nug2. Protein Science, 11(12):2924–2931, 2009.

[124] Sehat Nauli, Brian Kuhlman, and David Baker. Computer-based redesign of a protein folding pathway. Nature Structural & Molecular Biology, 8(7):602–605, 2001.

[125] Yi Cao, MM Balamurali, Deepak Sharma, and Hongbin Li. A functional single-molecule binding assay via force spectroscopy. Proceedings of the National Academy of Sciences, 104(40):15677–15681, 2007.

[126] Yi Cao, Teri Yoo, Shulin Zhuang, and Hongbin Li. Protein–protein interaction regulates proteins mechanical stability. Journal of Molecular Biology, 378(5):1132–1141, 2008.

[127] Tao Shen, Yi Cao, Shulin Zhuang, and Hongbin Li. Engineered bi-histidine metal chelation sites map the structure of the mechanical unfolding transition state of an elastomeric protein domain gb1. Biophysical Journal, 103(4):807 – 816, 2012.

[128] Shanshan Lv, Daniel M Dudek, Yi Cao, MM Balamurali, John Gosline, and Hongbin Li. Designed biomaterials to mimic the mechanical properties of muscles. Nature, 465(7294):69–73, 2010.

[129] Yohichi Suzuki and Olga K Dudko. Single molecules in an extension clamp: Extracting rates and activation barriers, *submitted*.

[130] Hao Yu, Amar Nath Gupta, Xia Liu, Krishna Neupane, Angela M Brigley, Iveta Sosova, and Michael T Woodside. Energy landscape analysis of native folding of the prion protein yields the diffusion constant, transition path time, and rates. Proceedings of the National Academy of Sciences, 109(36):14452–14457, 2012.

[131] Joost te Riet, Allard J Katan, Christian Rankl, Stefan W Stahl, Arend M van Buul, In Yee Phang, Alberto Gomez-Casado, Peter Schön, Jan W Gerritsen, Alessandra Cambi, et al. Interlaboratory round robin on cantilever calibration for afm force spectroscopy. Ultramicroscopy, 111(12):1659–1669, 2011.

[132] Yohichi Suzuki and Olga K Dudko. Single-molecule rupture dynamics on multidimensional landscapes. Physical Review Letters, 104(4):48101, 2010.

[133] PJ De Pablo, J Colchero, J Gomez-Herrero, and AM Baro. Jumping mode scanning force microscopy. Applied Physics Letters, 73(22):3300–3302, 1998.

[134] Izhar Medalsy, Ulf Hensen, and Daniel J Muller. Imaging and quantifying chemical and physical properties of native proteins at molecular resolution by force–volume afm. Angewandte Chemie International Edition, 50(50):12103–12108, 2011.

[135] Thomas Fuhs, Lydia Reuter, Iris Vonderhaid, Thomas Claudepierre, and Josef A Käs. Inherently slow and weak forward forces of neuronal growth cones measured by a drift-stabilized atomic force microscope. Cytoskeleton, 70(1):44–53, 2013.

[136] Taka-aki Yano, Taro Ichimura, Shota Kuwahara, Prabhat Verma, and Satoshi Kawata. Subnanometric stabilization of plasmon-enhanced optical microscopy. Nanotechnology, 23(20):205503, 2012.

Appendix A

Scripts for making an array of holes on the FEI focused ion beam instrument

This is an example of a script that produces an array of holes using the runscript function on the FEI focused ion beam. It consists of two files. ABC_mask_June2010.MIL makes a part of the pattern that fits in one screen (at 1000x magnification), then ABC_mask_June2010.psc calls that pattern, and mills it at various stage positions to build up the entire array of holes. To create an array of holes that is roughly 1 mm $\times$1 mm, repeat the instructions between # in ABC_mask_June2010.psc 10 times and call that file using runscript.

File: ABC_mask_June2010.MIL

```
# Forms the grid and mills
x0 = 0 y0 = 0
setpatinfo 0.3, si
clear
circle x0, y0, 0, 0.60
x0 = x0 + 10
circle x0, y0, 0, 0.60
x0 = x0 + 10
circle x0, y0, 0, 0.60
x0 = x0 + 10
circle x0, y0, 0, 0.60
x0 = x0 + 10
```

```
circle x0, y0, 0, 0.60
x0 = x0 + 10
circle x0, y0, 0, 0.60
x0 = 0
y0 = y0 - 30
circle x0, y0, 0, 0.60
x0 = x0 + 10
circle x0, y0, 0, 0.60
x0 = x0 + 10
circle x0, y0, 0, 0.60
x0 = x0 + 10
circle x0, y0, 0, 0.60
x0 = x0 + 10
circle x0, y0, 0, 0.60
x0 = x0 + 10
circle x0, y0, 0, 0.60
mill
```

File: ABC_mask_June2010.psc

```
run ABC_mask_June2010.MIL
setparallelmode 0
#
getstagepos
stagemove x, x+0.06
mill
getstagepos
stagemove x, x+0.06
mill
```

```
getstagepos
stagemove x, x+0.06
mill
getstagepos
stagemove x, x+0.06
mill
getstagepos
stagemove x, x+0.06
mill
getstagepos
stagemove x, x+0.06
mill
getstagepos
stagemove x, x+0.06
mill
getstagepos
stagemove x, x+0.06
mill
getstagepos
stagemove x, x+0.06
mill
getstagepos
stagemove x, x-0.54
stagemove y, y-0.06
mill
#
```

Appendix B

Descriptions of key LabVIEW vis

In this appendix, I briefly describe the critical LabVIEW vi's. Because the number of vis is large, I have grouped the descriptions.

Utilities

Stage FIFO read 2011.vi and Tip FIFO read 2011.vi Read all of the points currently in the stage or tip FIFO, which is the structure that transfers data from the FPGA to the host computer. It then deinterlaces the data, and outputs two clusters: one with arrays of all the data collected, and one with the mean value of for each item. Data items include raw QPD voltages, scaled positions (and force in the case of the tip), signals sent to the translation stages, and setpoints.

Stage FIFO read number 2011.vi and Tip FIFO read number 2011.vi Collects a certain number of data points. To do this, it clears the FIFO, pauses for the correct amount of time, then uses the previous vi to read out the desired data.

StageChangeOffset r1_3.vi and TipChangeOffset r1_3.vi Change the stage and tip offsets in x, y, and z on the FPGA program. The offset defines the zero setpoint with respect to the entire range of the stage.

StageChangeSetpoint r1_3.vi and TipChangeSetpoint r1_3.vi Change the stage and tip setpoints in x, y, and z. If the servo loops are off, these are simply the requested positions with respect to the offsets. If the servo loops are on, they are the servo set points.

StageReportOffset r1_3.vi and TipReportOffset r1_3.vi Read the offsets in x, y, and z from the FPGA. These offsets define the zero setpoint with respect to the entire range of the stage.

StageReportSetpoint r1_3.vi and TipReportSetpoint r1_3.vi Read the setpoints in x, y, and z from the FPGA.

Force calibrate new algorithm_3.vi Moves the tip into the surface until a user-specified voltage threshold is reached, then finds the zero-force voltage and the sensitivity (V/nm). In this version, these are found by performing successive sets of linear, then choosing the pair with

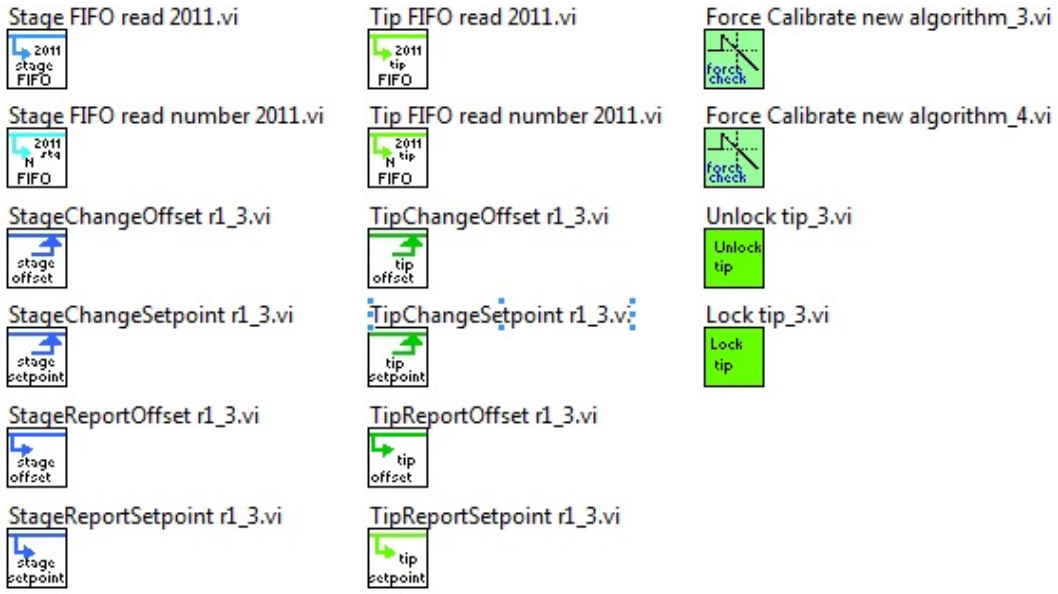

Figure B.1: Collection of vis that operate as general utilties to perform various tasks. These show up in numerous places in the software.

the lowest error. This corresponds to one line fitting the data when the tip is above the surface, and one when the tip is in contact. Loads these parameters onto the FPGA chip, and saves them to a file.

Force calibrate new algorithm_4.vi Like the previous vi, this one moves the tip into the surface until a user-specified voltage threshold is reached, finds the zero-force voltage and the sensitivity (V/nm), loads these parameters onto the FPGA chip, and saves them to a file. The difference is that this one uses user-adjusted cursors to determine where the transition between tip on surface and above surface is.

Unlock tip_3.vi and Lock tip_3.vi Unlocks and locks the tip servo loops without moving the tip. If the tip position has drifted, maintaining the same set points when turning off or on the servos causes it to move, which can disrupt experiments. These vis solve the problem by determining and using the set point that will keep the tip at its current position.

Programs called by the imaging vi

WriteArrayWithHeadersToFile r1_3.vi This is a very general vi that writes an array as a text file, with headers describing each column. Here it is being used to save force-versus-distance curves during the force check.

Update servo controls UI_3.vi Allows the user to update the on/off status, gains, and setpoints of the six servo loops. The user can also use this vi to control which parameter is being servoed for the tip z position (force or position).

Control Servos During Scan_3.vi This is similar to the previous vi, except that it does not allow the user to update the setpoints on the sample. It is meant for use during scanning, when the sample setpoints are being handled programatically elsewhere.

Prep Arrays_3.vi Takes the raw line scans from the various line scan vis and formats them into images for saving and for viewing. The image for saving does not have any additional processing; each line scan in the image for viewing has a fit line subtracted from it.

save image_3.vi Saves the images. Three files— forward, reverse, and aux— are written. For normal imaging, these correspond to the image when the tip is going forward across the sample, when it is going the opposite direction, and the error image for the forward-going. Other modes may re-purpose these. This vi also saves information from the scan parameter and control clusters.

Prep Arrays_3.vi Takes the raw line scans from the various line scan vis and formats them into images for saving and for viewing. The image for saving does not have any additional processing; each line scan in the image for viewing has a fit line subtracted from it.

LargeOpticalScan.vi Makes a large-area optical scan by taking optical images at different substage positions, then stitching them together into a single, large image.

SelectSSPosZoom.vi Allows the user to look at the large-area optical scan and choose a region with desired features, then recenters the substage on that area.

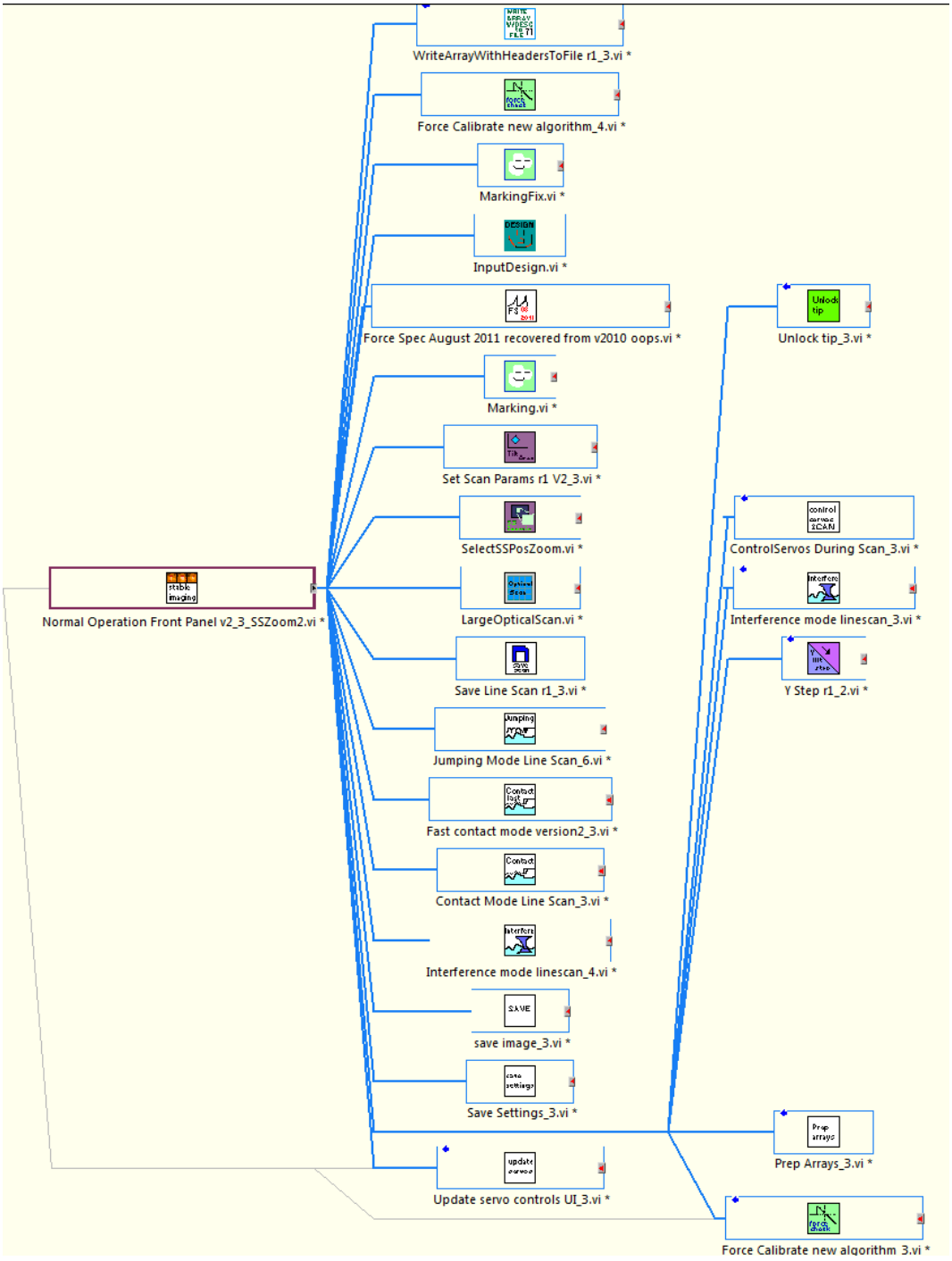

Figure B.2: Hierarchy diagram of programs that run under the operation vi, after calibration

Y Step r1_2.vi Makes one step in the slow scanning direction, which is typically y, the long axis of the cantilever. However, it can make a step in an arbitrary direction depending on the requested scan angle.

Contact Mode Line Scan_3.vi Takes a contact mode line scan in x by moving the stage, waiting for it to finish the move, then collecting data for the pixel. This is a relatively precise but slow way of creating a contact mode image.

Fast contact mode version2_3.vi Takes a contact mode line scan by continually moving the stage in x and simultaneously taking data, then dividing the data into pixels. This is a faster but less precise method of creating a contact mode image. It is sufficient for most tasks.

Jumping Mode Line Scan_6.vi Makes a jumping mode line scan. In this mode, the tip is lowered to the surface until a specified force threshold is reached. The PZT height at this point is then recorded as the pixel value. Jumping mode is a slow but gentle mode of imaging.

Interference mode linescan_3.vi Does an optical line scan. The user can choose whether to scan with the λ=845 nm laser focus or the λ=810 nm laser focus, which is the typical choice because it is registered to the tip position.

Interference mode linescan_4.vi Same as the previous vi, but with more outputs and graphical displays. Both are used for historical reasons.

Marking.vi The original marking program written by Louisa Eberle. Brings the tip into contact with the surface and makes a pre-defined mark.

MarkingFix.vi A version of the previous vi revised by Matt Siewny. Makes a series of marks defined by an input array of endpoints, and an array that defines whether the tip is engaged or disengaged with the surface on each segment. This way, a non-continuous pattern can be made.

InputDesign.vi Allows the user to draw a series of segments and organizes them into the correct arrays to serve as inputs to "MarkingFix.vi."

Force Spec August 2011 recovered from 2010 oops.vi The current force spectroscopy program, which includes a state machine to run various force spectroscopy-related tasks; continuous data reading and saving; displays of force versus extension, force versus time, and extension histogram; and control through the keyboard, mouse and video game controller. Since this program is both complicated and critical for the data described in this thesis, its sub-vis are described in detail in the following section.

Programs that run on the FPGA

FPGA Top Level v2.vi This is the top-level program running on the FPGA chip, which the programs on the desktop computer calls. In addition to the functions provided by the sub-vis described below, the top-level program contains logic, used during force spectroscopy, to perform functions such as ramping z position and clamping extension or force.

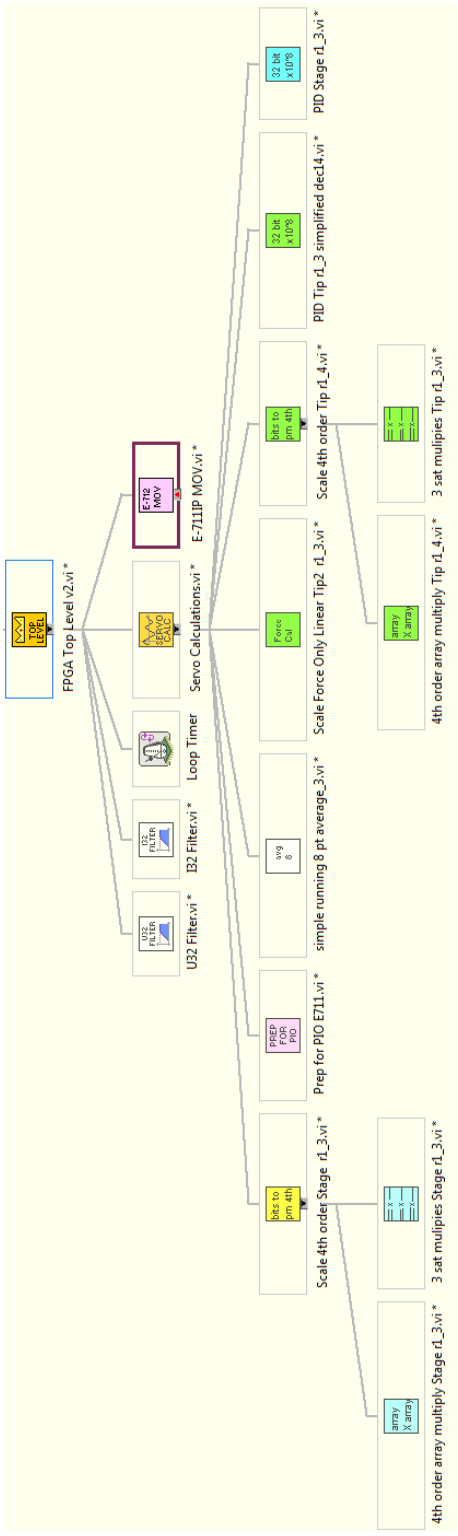

Figure B.3: Hierarchy diagram of programs that run on the FPGA chip during AFM calibration and operation.

U32 Filter.vi and I32 Filter.vi These use "niFPGA Discrete Control Filter.vi," which only takes I16 data type and filters by 10 points. They split the U32 or I32 types into I16, use the filter, then put the 32-bit number back together.

U32 Filter.vi and I32 Filter.vi These use "niFPGA Discrete Control Filter.vi," which only takes I16 data type and filters by 10 points. They split the U32 or I32 type number into I16, use the filter, then put the 32-bit number back together.

Loop Timer This is a timer for the while loop. It is a standard LabVIEW FPGA element.

E-711P MOV.vi This vi arranges and sends the parallel interface outputs to the E-712 controller from Physik Instrumente. It was provided by Scott Jordan of PI.

Servo Calculations.vi This vi handles the acquisition, scaling, servo calculations, data handling to prepare for output, and writes to FIFO memory items to be read on the desktop computer. It does this primarily by calling the rest of the vis listed in this section.

Scale Force Only Linear Tip2 r1_3.vi This vi takes the optical lever data and scales it according to the linear sensitivity determined by touching off the surface.

Scale 4th order Stage r1_3.vi and Scale 4th order Tip r1_4.vi These scale the raw voltage data V_x, V_y, and V_z from the QPDs according to the 4th order polynomials determined during the calibration step. They combine the raw voltages into the correct arrangements (e.g., $V_x V_y^2 V z$) using the "3 sat multiplies" vis, then hand these off to the "4th order array multiply" vis to multiply in the fit coeffecients.

3 sat multiplies Stage r1_3.vi and 3 sat multiplies Tip r1_3.vi These simply contain 3 saturation multiplies apiece. "Saturation multiply" means that if the size of the number exceeds the space alloted for it, the number will saturate rather than wrapping, which causes much more trouble. The reason for this vi is essentially a trick to save space on the FPGA chip. By setting the vi to "re-entrant," only one instance of this vi takes up space on the FPGA chip, and it gets called sequentially each time it is needed. It is thus a way to trade time for space on the chip.

4th order array multiply Stage r1_3.vi and 4th order array multiply Tip r1_3.vi These multiply the fit coeffecients in to the polynomials.

Appendix C

Files output by US-AFM software

This is a list of files written by the US-AFM software. "BaseName" is the base file name, which consists of a user-defined name, plus a time stamp. "N" is the image number stamp.

BaseName.fcoeff contains the coeffecients for the force fit, to calibrate the optical lever signal.

BaseName.FZ contains force-versus-extension curves obtained while calibrating the optical lever signal, in binary format.

BaseName.wig1x, BaseName.wig1y, and **BaseName.wig1z** contain the x, y, and z wiggle signals used to align the tip, in text format.

BaseName.sampcal and **BaseName.tipcal** are the 3D raster scan data used to calibrate the sample and the tip.

BaseName.xcoeff, BaseName.ycoeff, BaseName.zcoeff, BaseName.xsampcoeff, BaseName.ysampcoeff, and **BaseName.zsampcoeff** are the tip x, y, and z; and sample x, y, and z fit coeffecients determined by the tip and sample calibrate programs. These can be viewed in Igor Pro, together with the 3D raster scan data, using the "Calibration Analysis" macro (calibration procedure.ipf and CalibrationPanel.ipf) written by George Emanuel.

When time-series data are acquired with "Update servo controls UI_3.vi" or "Control Servos During Scan_3.vi," the data is written as binary files with the extension **.733** for the sample and the extension **.PC** for the tip. The label **error** is used for a file containing output data to the nanopositioning stage, **set** is for a requested position, and **845** or **810** with the label **x, y,** or **z** are

measured positions.

BaseName_N_Forward.STM, BaseName_N_Reverse.STM, and **BaseName_N_Aux.STM** are the image files. For normal AFM scanning, these are the forward, reverse, and deflection signals. For optical scanning, they are the z, x, and y signals.

The file extension **.pull** is used for all of the force spectroscopy data. Within this set, files flagged with **810x, 810y, 810z,** and **785z** are the measured x, y, and z positions; and the measured z deflection of the tip. The file flagged with **Zerror** is the z control signal output to the tip translation stage (Picocube), **Zset** is the requested tip position in z, and **Mode** is a code describing the tip function at any time (0 for finding the surface, 1 for retracting, 2 for pausing on the surface, and -1 for other behavior). Finally, the files **Aux1** and **Aux2** are currently used for the sample translation stage z position and the z output to the sample translation stage, respectively. These can be loaded into Igor Pro using the "Load AFM data" program written by George Emanuel.

Appendix D

Pseudocode for force spectroscopy LabVIEW program

(0000–0099 Straight operation or zigzag)

0000 IF force >= Threshold Force, move down, ELSE GOTO 10

0010 IF elapsed time <= Delay, hold still, ELSE GOTO 20

0020 CASE 0 (No autoend, no refold): IF Position <= Z retract, move up, ELSE GOTO 9999

CASE 1 (Autoend, no refold): IF Continue true, move up, ELSE GOTO 9999

CASE 2 (No autoend, refold): IF Position <= Z retract, IF 3rd event reached, GOTO 30, ELSE move up, ELSE GOTO 9999

CASE 3 (Autoend, Refold): IF Continue true, IF 3rd event reached, GOTO 30, ELSE move up, ELSE GOTO 9999

0030 IF position >= 10 nm, move down, ELSE GOTO 40

0040 IF elapsed time <= 1s, clamp position, ELSE GOTO 50

0050 IF position <= Z retract, move up, ELSE GOTO 9999

(0100-0199 Triggered force clamp)

0100 IF force >= Threshold Force, move down, ELSE GOTO 110

0110 IF elapsed time <= Delay, hold still, ELSE GOTO 115

0115 Arm autoclamp. GOTO 0120

0120 IF Position <= Z retract (no autoend) OR IF Continue true (Autoend),

IF Clamping false, move up, ELSE GOTO 0130, ELSE GOTO 9999

0130 IF Done false, allow user to adjust force clamp, ELSE GOTO 0140

0140 IF position <= Z retract, move up, ELSE GOTO 9999

(0200-0299 Slow position clamped zigzag)

0200 IF force >= Threshold Force, move down, ELSE GOTO 210

0210 IF elapsed time <= Delay, hold still, ELSE GOTO 220

0220 IF position <= 5 nm, move up, ELSE turn on position clamp, GOTO 0230

0230 CASE 0 (No autoend): IF Position <= Z retract, IF 3rd event reached, GOTO 0240, ELSE move up slowly, ELSE turn off pos clamp, GOTO 9999

CASE 1 (Autoend): IF Continue true, IF 3rd event reached, GOTO 0240, ELSE move up slowly, ELSE turn off pos clamp, GOTO 9999

0240 IF position >= 10 nm, move down at 2 nm/s, ELSE GOTO 0250

0250 IF position <= Z retract, move up slowly, ELSE turn off position clamp, GOTO 9999

(0300-0399 Position clamp)

0300 IF force >= Threshold Force, move down, ELSE GOTO 310

0310 IF elapsed time <= Delay, hold still, ELSE GOTO 320

0320 IF Position <= clamp position, move up, ELSE turn on position clamp, GOTO 0330

0330 IF Done false, allow user to adjust position clamp, ELSE GOTO 0340

0340 IF position <= Z retract, move up, ELSE GOTO 9999

(0400-0499 Adjust setpoint with mouse, then do zigzag)

0400 Clamp at current position, GOTO 410

0410 IF Done false, Allow user to adjust setpoint with mouse, ELSE GOTO 411

0411 Turn on locked ramping

0412 IF Position <=x position of Right bound, Go up at slow rate, ELSE GOTO 0414

0414 IF Position >=x position of left bound, Go down at slow rate, ELSE GOTO 0416

0416 IF elapsed time <= relax time, hold still, ELSE GOTO 0418

0418 IF Done false, GOTO 0412, ELSE GOTO 0420

0420 IF position <= Z retract, move up, ELSE GOTO 9999

(0500-0599 Page 89 in book VI)

0500 IF force >= Threshold Force, move down, ELSE GOTO 510

0510 IF elapsed time <= Delay, hold still, ELSE GOTO 520

0520 IF Position <= z retract,

IF Position >= cursor 2 x AND Force >= Cursor 2 y,

GOTO 0530,

ELSE go up,

ELSE GOTO 9999

0521 Turn on locked ramp

0530 IF Position >= Cursor 0 x, Go down, ELSE GOTO 0535

0535 Wait for Refold Time

0540 IF Position <= Cursor 1 x, Go up slowly, ELSE GOTO 0550

0550 IF Position >= Cursor 0 x, Go down slowly, ELSE GOTO 0560

0560 IF Done false, GOTO 0540, ELSE GOTO 0570

0570 IF Position <= Z retract, move up, ELSE GOTO 9999

(0800-0899 Force quench 3)

0800 IF force >= Threshold Force, move down, ELSE GOTO 810

0810 Turn on force clamp, GOTO 0820

0820 Wait delay

0830 Move force clamp to 70 pN above surface

0840 Wait 3 s

0850 Move force clamp to 20 pN above surface

0860 Wait 5 s

0870 Move force clamp to 70 pN above surface

0880 Wait 3 s, Show dialog: Is there a molecule? Yes, GOTO 850, No GOTO 9999

(1000-1099 Testing clamp tip base)

1000 IF force >= Threshold Force, move down, ELSE GOTO 1010

1010 IF elapsed time <= Delay, hold still, ELSE GOTO 1020

1020 IF position <= 5 nm, move up, ELSE turn on position clamp, GOTO 1030

1030 IF position <= Z retract, move up at slow rate, ELSE GOTO 9999

(1100-1199 Auto find end, then do zigzag)

1100 IF force >= Threshold Force, move down, ELSE GOTO 1110

1110 IF elapsed time <= Delay, hold still, ELSE GOTO 1120

1120 Set auto turnaround switch and thresholds, GOTO 1130

1130 IF Position <= Z retract, IF threshold not reached, move up, ELSE GOTO 1140, ELSE GOTO 9999

1140 IF Position >=x position of left bound, Go down at slow rate, ELSE GOTO 1150

1150 IF Position <=x position of Right bound, Go up at slow rate, ELSE GOTO 1140

(1200-1299 On chip slow zigzag)

1200 IF force >= Threshold Force, move down, ELSE GOTO 1210

1210 IF elapsed time <= Delay, hold still, ELSE GOTO 1220

1220 IF Position <= z retract,

IF Position >= cursor 2 x AND Force >= Cursor 2 y, GOTO 1230,

ELSE go up,

ELSE GOTO 9999

1230 IF "Done" FALSE

Update FPGA chip parameters for ramping between cursors 1 and 2, GOTO 1230

ELSE end ramp, GOTO 1240

1240 IF Position <= z retract, pull to end, ELSE GOTO 9999

(1400-1499 Trigger then position clamp)

1400 IF force >= Threshold Force, move down, ELSE GOTO 1410

1410 IF elapsed time <= Delay, hold still, ELSE GOTO 1420

1420 IF Position <= z retract,

IF Position >= cursor 2 x AND Force >= Cursor 2 y, GOTO 1430,

ELSE go up,

ELSE GOTO 9999

1430 Set parameters on FPGA chip for position locking, GOTO 1440

1440 IF "Done" FALSE

IF "Refold" FALSE, allow user to control extension with X-Box controller

ELSE do routine to touch gently off the surface

ELSE end ramp, GOTO 1450

1450 IF Position <= z retract, pull to end, ELSE GOTO 9999

(2100-2199 Force clamp then ramp)

2100 IF force >= Threshold Force, move down, ELSE GOTO 2110

2110 IF elapsed time <= Delay, hold still, ELSE GOTO 2120

2120 IF Position <= z retract,

IF Position >= cursor 2 x AND Force >= Cursor 2 y, GOTO 2130,

ELSE go up,

ELSE GOTO 9999

2130 Ramp back down to left bound cursor, GOTO 2140

2140 Update parameters for force lock on the FPGA chip, GOTO 2150

2150 Wait for specified time, GOTO 2160

2160 Pull to 3rd cursor, GOTO 2130

9999 Stop moving, turn off all clamps, end loop

Appendix E

Bacteriorhodopsin sample preparation at neutral pH

(1) Clean Substrates

(a) Optional: En-Solv may be used to remove old immersion lens oil

(b) Clean samples for 5 minutes in acetone in bath sonicator (Branson 2510)

(c) Rinse with isopropyl alcohol

(d) Clean samples for 5 minutes in DI water in bath sonicator

(e) Submerge samples in piranha heated at 30% on hot plate. Caution: Piranha is hazardous! Proper training, PPE, handling, and disposal are critical to ensuring safety.

(i) Protocol a: 400 mL H_2SO_4, 25 mL H_2O_2

(ii) Protocol b (preferred): 60 mL H_2SO_4, 20 mL H_2O_2

(f) Allow solution to cool

(g) Transfer samples to 1L beaker full of DI water and rinse several times

(h) Clean samples for 5 minutes in DI water in bath sonicator

(i) Dry samples with filtered Nitrogen

(2) Make Sample

(a) Mix stock BR solution (0.25 mg/mL) from purchased powder (1 mg)

(i) Mix 2 mL of water into bottle of lyophilized membrane from sigma

(ii) Prepare 1% NaN_3 solution

(iii) Mix aliquots with:

(iii.a) 500 μL BR solution

(iii.b) 10 μL NaN_3 solution

(iii.c) 490 μL DI water

(iv) Flash-freeze unused portions

(b) Mix imaging buffer (30 mL)

(i) Filtered deionized water (25.2 mL)

(ii) 10 mM Tris-Cl, pH 7.2 (0.3 mL of 1M)

(iii) 150 mM KCl (4.5 mL of 1M)

(iv) Filter using 0.2 μm syringe filter

(v) Degas: pull vacuum and sonicate for 20 minutes

(c) Mix adsorption buffer with 1 mL of imaging buffer and 25 μL of 1M $MgCl_2$

(d) Mix dilute purple membrane

(i) 30 μL BR stock, invert to mix

(ii) 60 μL adsorption buffer

(iii) Sonicate in Sonics Vibracell sonicator for 10s-2min

(e) Clean sample holder

(i) Ultrasound for ∼30s in soapy water

(ii) Rinse thoroughly with DI water

(iii) Rinse 3X with isopropyl alcohol and water— it is critical to remove all soap residue

(f) Mount sample

(i) Heat sample holder to 95℃

(ii) Apply a small amount of wax (Crystalbond 509) around the hole for the objective

(iii) Determine sample orientation with optical microscope and mount on holder

(g) Oxygen plasma clean

(i) First: 50 SCCM, 300 W, 120s

(ii) Second: 50 SCCM, 150 W, 120s

(h) Deposition

(i) Put Teflon ring on sample holder

(ii) Deposit 90 μL of BR solution

(iii) Let it adsorb for 30-40 minutes

(iv) During adsorption, seal outside of Teflon ring with Repro-Rubber

(i) Rinse

(i) Rinse aggressively to remove poorly-adhered patches

(ii) Rinse at least 3 times with 1 mL imaging buffer

(iii) Sample can be stored in the fridge overnight and rinsed with fresh buffer in the morning

Appendix F

Bacteriorhodopsin sample preparation at neutral pH

This is the protocol for depositing BR onto APTES monolayers at low pH developed by Ruby Sullan.

Reagents:

(1) Acetone

(2) APTES (Sigma A3648)

(3) Toluene (anhydrous, Sigma 244511)

(4) Hydrogen peroxide 30%

(5) Sulfuric acid (98%)

(6) Deionized water (>18 MΩ-cm)

(7) Stock BR (see Appendix E)

(8) Low pH adsorption buffer: 500 mM citrate, 10 mM Tris-Hcl, pH 3.0

(9) Imaging buffer: 300 mM KCl, 10 mM Tris-HCl, pH 7.8

Other required equipment:

(1) Coverslips (22×22 mm for US-AFM or 12 mm diameter for Cypher)

(2) Teflon rack

(3) Bath sonicator (Branson 2510)

(4) Hot plate

(5) 110 °C oven

(6) Filtered, dry N_2 gas

(7) Vortex mixer

Silanization:

(1) Put coverslips in the Teflon rack (make sure they are separate and do not touch each other).

(2) Pre-treatment of coverslips (This is similar to KOH etching protocol.)

   (a) Sonicate in acetone for 10 mins.

   (b) Sonicate in ethanol for 5 mins.

   (c) Sonicate in KOH for 3 mins.

   (d) Sonicate in Milli-Q H2O for 5 mins.

   (e) Rinse with Milli-Q H2O 3x.

   (f) Blow dry with N2.

(3) Start beaker drying in oven at 110 °C. It should dry for 30 min.

(4) Piranha cleaning (Caution: Piranha is hazardous! Proper training, PPE, handling, and disposal are critical to ensuring safety.

   (a) Work under the fume hood.

   (b) Heat sulfuric acid.

   (c) Carefullly lower Teflon rack with coverslips into sulfuric acid. Make sure that the coverslips are separate and below the surface of the liquid.

   (d) Add H_2O_2 to make a 3:1 mixture of sulfuric acid to H_2O_2.

(e) Incubate the coverslips in piranha solution (heated) until bubbles are no longer coming out from the solution (this takes ∼15-20 mins).

(f) Remove from the hot plate and allow to cool (∼30 mins-1 hr)

(5) Rinse with deionized water.

(6) Dry with filtered N_2.

(7) Fill flask dried in oven with toluene.

(8) Add 1.5% v/v of APTES.

(9) Rinse coverslips with tolulene and blow dry with filtered N_2

(10) Immerse the holder slowly in the toluene-silane mixture (it should take ∼10 sec.) Make sure that the coverslips are seperate in the container and all covered with solution. **No water should get into the toluene/silane mixture! It can promote polymerization of silane.**

(11) Incubate 30 min. at room temperature.

(12) Rinse every coverslip with toluene and dry it with filtered N_2.

(13) Store coverslips at room temperature.

BR incubation:

(1) Mix 7.5 μL 0.25 mg/mL stock BR and 82.5 μL adsorption buffer.

(2) Sonicate for 2-4 minutes.

(3) Vortex for 30 s.

(4) Incubate for 45 minutes- 2.5 hours.

(5) Rinse aggressively with imaging buffer using a squirt bottle but not directly aiming at the center of the sample.